UNIVERSITÀ
DEGLI STUDI
DI PADOVA

Sede Amministrativa: Università degli Studi di Padova

Dipartimento di Scienze Chimiche

CORSO DI DOTTORATO DI RICERCA IN SCIENZE MOLECOLARI

CURRICOLO CHIMICO

CICLO XXX

PEROVSKITE MATERIALS AS ELECTRODES FOR SOLID OXIDE FUEL CELLS ACTIVE TOWARD SUSTAINABLE REACTIONS

Coordinatore: Ch.mo Prof. Leonard Jan Prins

Supervisore: Prof.ssa Antonella Glisenti

Dottorando: Alberto Garbujo

If we knew what we were doing,

it wouldn't be called research,

would it?

Albert Einstein

CONTENTS

LIST OF ABBREVIATIONS

A

AFC	Alkaline Fuel Cell
ATR	Auto-thermal Reforming

B

BE	Binding energy
BET	Brunauer Emmett Teller

C

CO	Carbon Monoxide
CO2	Carbon Dioxide
CPE	Constant Phase element
CRW	Critical raw materials

D

DC	Direct current
DIR	Direct internal reforming

DMFC	Direct Methanol Fuel Cell
DMFC	Direct methanol fuel cell

E

e.g.	'Exempli gratia' – Latin for 'for example
E_a	Activation Energy
EC	European Community
EIS	Electrochemical Impedance Spectrum
EU	European Union

G

GC	Gas chromatograph
GDC	Gadolinium doped ceria
GHSV	Reactant Gas Flow Rate/Reactor Volume
GT	Gas turbine

H

h	hour
H_2	Hydrogen
H_3PO_4	Phosphoric Acid
HE-XRD	High Energy X-ray diffraction
HF	High Frequency

IF	Intermediate Frequency
IT	Intermediate temperature

L

LF	Low Frequency
LSC	Strontium doped lanthanum chromate cobaltites
LSM	Lanthanum strontium manganese
LST	Lanthanum strontium titanate

M

MCFC	Molten carbonate Fuel Cell

N

NASA	National Aeronautics and Space Administration

O

OCV	Open circuit voltage

P

PA	Phosphoric Acid
PAFC	Phosphoric Acid Fuel Cell
PEM	Polymer electrolyte membrane
PGM	Platinum group metal
ppm	Parts per million

S

SDC	Samarium doped ceria
SOFC	Solid Oxide Fuel Cell

T

T	Temperature
TCD	Thermal conductivity detector
TEC	Thermal expansion coefficient
TPB	Triple phase boundary
TPO	Temperature programmed oxidation
TPR	Temperature programmed reduction

W

WI	Wet impregnation
wt. %	Weight percentage

X

XPS	X-ray photoelectron spectroscopy

Y

YSZ	Yttrium stabilized zirconia

Introduction

In the history the increase of energy consumption has been followed by several benefits, such as longer life expectation, better living conditions, easier travels and even space exploration. Nowadays, energy is essential for life as we know it. In 2015 the global energy demand was 14,490 Mtoe (millions of tonne of oil equivalent) corresponding to 168,519 TWh and it is expected to grow, although slower than the last two decades, 1.3% per year up to 2035, mainly driven by the emerging economies [1]. Even if the following years will be influenced, as never before, by the gradual transition to renewables sources, it was estimated that in 2035 the fossil fuels will still be the dominant [2].

Beside the benefits previously described, energy consumption has produced some problems such as global warming, climate change, air pollution, resources depletion and deforestation. Moreover, the BP Energy Outlook (British Petroleum) has estimated that in 2017 more than 1 billion of people in the world will not have access to electricity [2]. Many efforts were carried out to study and to solve these problems. Targets and road maps have been proposed by energy councils and countries with the aim of extending the electricity access over the world population while mitigating climate changes phenomena. Several researchers from all scientific fields are involved in achieving sustainable solutions. The European Union (EU) has set the reduction of carbon dioxide by at least 80% by 2050 (to be compared to 1990) [3].

The limits imposed by European Union appear challenging [4]. In fact, in 2015 more than 42% of total energy production was used for power generation and the actual energy conversion devices are characterized by a low efficiency conversion [2]. Within this scenario, finding a proper alternative energy source is therefore inevitable for a sustainable future. The renewable energy sources (hydro, wind, solar, geothermal, biomass and biofuels) have been proposed as a possible solution in order to meet the increasing energy demands and to diffuse electricity over less developed countries [1][3]. However, the renewable energy diffusion is slowed down by some drawbacks, such as high cost and intermittent energy production (in particular, this problem concerns wind and solar power) [5]. For this reason the electricity storage has a strategic importance. The use of hydrogen as energy vector could be used to overtake the intermittent electricity production of wind and solar power [6]. In fact, hydrogen gas has an energy density of 120 MJ Kg^{-1} and could be produced through the electrolysation of water and could be stored as compressed gas [7]. Hydrogen then could be used as a common fuel in a thermal engine or in a fuel cell. In fact, one of the most promising technologies, that has received a great attention during the last decades, is the fuel cell. Although the first fuel cell was invented in 1839 by Sir Williams Grove, several improvements were required in order to obtain an efficient and economical device [8][9][10]. The fuel cell is a device able to convert directly the chemical energy (fuel) into electrical energy. This is characterized by high electrical efficiency and is considered one of the cleanest power generating technologies. Many types of fuel cells have been developed during the past centuries, each one with peculiar characteristics. Among them, Solid Oxide Fuel Cells (SOFCs) have attracted the attention of researchers due to their fuel flexibility and low cost materials [10][11][12][13]. SOFCs are characterized by the highest working temperatures (800-1000°C) between fuel cells and this allows fuel versatility,

internal reforming and auto-thermal reforming [14][15]. The possibility to be fed with different fuels (different respect to hydrogen) appears extremely interesting with respect to the slow transition from fossil to renewable fuels. Besides, there are some difficulties related to the production and the storage of hydrogen [6]. An extremely high efficiency in combined co-generation cycles (coupled with gas turbine system, 70%, or by extracting heat and power, 70-90%) can be reached thanks to the operating temperature [10][16]. The high performance and tolerance toward pollutants, SOFCs are not poisoned by carbon monoxide in contrast to the low temperature fuel cells, have highlighted this technology as the most suitable for large stationary power plant applications. The demerits of SOFCs are the durability of materials, the long start-up time, the need of high performance materials and the cost of thermal isolation [10][17][18]. All these problems are linked to the working temperature. In the last years great efforts have been addressed to the development of SOFC that can work at intermediate temperature (600-800°C). The temperature decrease involves a series of problems caused by the consequent reduction of catalytic activity and conductivity [18]. The realization of an intermediate temperature solid oxide fuel cell (IT-SOFC) requires the formulation of new specific designed materials with high performance at 600-800°C. The research for new materials is of primary importance for a commercial future of IT-SOFCs.

The aim of this research is to develop advanced perovskite based materials specifically designed to be used as electrode for IT-SOCFs fed with biofuels (methane). The methane was chosen due to its role as bio-fuel in the carbon footprint decrease (bio gas, CH_4 and CO_2) and so the catalytic and electrocatalytic reactivity behaviour toward methane were investigated. Two different perovskite-based materials have been studied for SOFC application, titanates and cobaltites.

Titanates are considered one the most promising anode materials for SOFC application [15][19][20]. They show a great stability versus reductive environments and pollutants (e.g. H_2S), but suffer of some weakness such as a low catalytic activity and electron conductibility. However these properties could be enhanced through a suitable doping. Molybdenum and iron were chosen as B-site doping in order to achieve this purpose. Cobaltites are well known to be very active in cathodic reactions but they have also high activity towards oxidation suggesting the possibility to be used in symmetric cell under appropriate conditions [21][22][23][24][25]. In particular cobalt based K_2NiF_4 type structures have been investigated due to their promising mixed-ionic-electronic conductivity and good mechanical and chemical compatibility with SOFC electrolyte [24]. Copper and nickel doping were used in order to enhance the catalytic activity toward sustainable reactions.

The Ti-based perovskites doped investigated are:

1. $SrTi_{0.9}Mo_{0.1}O_3$
2. $SrTi_{0.6}Mo_{0.4}O_3$
3. $Ba_{0.5}Sr_{0.5}Ti_{0.9}Mo_{0.1}O_3$
4. $Ba_{0.5}Sr_{0.5}Ti_{0.9}Fe_{0.1}O_3$
5. $Ba_{0.5}Sr_{0.5}Ti_{0.6}Fe_{0.4}O_3$

The K_2NiF_4-type cobalt based perovskites investigated are:

1. $(LaSr)_2Co_{0.5}Cu_{0.5}O_4$
2. $(LaSr)_2Co_{0.5}Ni_{0.5}O_4$

The thesis is based in six chapters:

1. In the first chapter a summary of the principles and functioning of the fuel cell, the fuel cell types and the peculiarity of solid oxide fuel cell are reported.
2. In the second chapter the perovskite oxides were presented as one of the most suitable materials for solid oxide fuel cell application. Moreover the design and the synthesis used are reported.
3. In the third chapter titanium based perovskite as anode for IT-SOFC have been investigated. The materials were fully characterized through XRD, XPS, TPR, TPO, SEM and their reactivity toward methane dry reforming was investigated by means of GC. Finally the electrochemical behaviour has been studied by impedance analysis under hydrogen environment.
4. In the fourth chapter the cobalt based perovskite with K_2NiF_4 type structures were investigated as symmetric electrodes for IT-SOFC feed with methane. XRD, XPS, TPR, TPO and SEM were performed in order to fully characterize the materials. Their activity toward direct methane oxidation was investigated and finally the electrochemical investigations under stationary air and under methane flow have been observed by means impedance analysis.
5. In the fifth chapter the study of the reversible structural properties of selected perovskite-type oxides toward redox pulsing as a function of temperature carried out at European Synchrotron Radiation Facility (ESRF) is reported.
6. In the final chapter the general conclusion and the prospective of these studies have been explained.

Chapter 1

1.1 Fuel cells: a long history

The fuel cell (FC) is an electrochemical device capable of converting chemical energy directly into electrical energy without the limit of Carnot cycle. The development of the fuel cell started in 1839 with Sir William Robert Grove, who was chemist and patent lawyer[8][9][10]. He was the first one to obtain electrical energy starting from two gases (hydrogen and oxygen) and with spongy platinum as electrodes during his famous water electrolyser/fuel cell experimental demonstration [9]. Several years later, precisely in 1889, starting from the results obtained by Sir William Robert Grove, L. Moud and C. Langer were able to achieve an efficiency of 50% in a fuel cell fed with hydrogen using platinum foil and platinum black as electrodes. Ten years later, in 1896, J. J. Jacques developed a new fuel cell based on molten salt as an electrolyte able of reaching 1.5 kW of power in a stack configuration [8]. After that demonstration the potential application of fuel cell becomes clear and gave rise to a relevant research field. Although the principles of FCs were discovered at the beginning of XIX century, only in 1932 with the pioneering work of Dr. Francis T. Bacon, the FC obtains the first great improvement. Dr. Francis and T. Bacon in fact replaced the expensive materials previously used, platinum, with cheaper ones with the aim of powering a vehicle (Bacon cell). His impressive work led to greater

enhancements and to the realization of the auxiliary power source for NASA's Apollo space vehicles, Figure in 1960s [8].

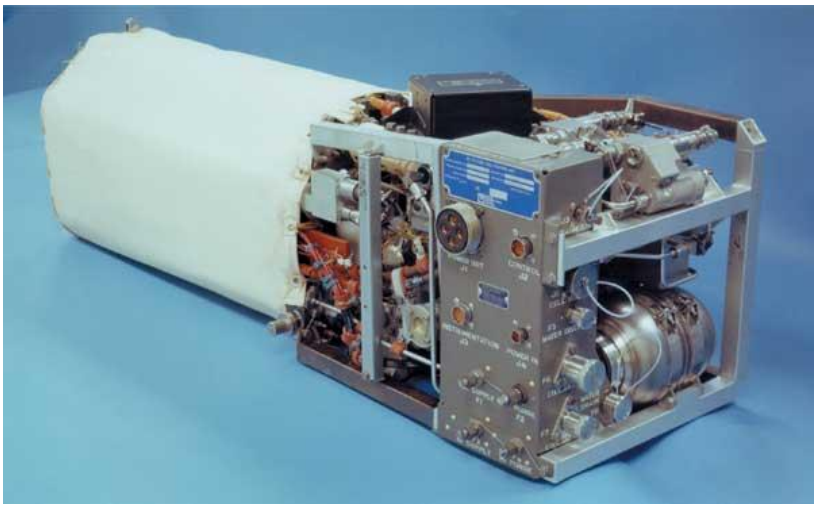

Figure 1.1: Alkaline fuel cell used into space shuttle (NASA) [26].

After the fuel cell success in the NASA programme many researchers focused their attention on developing new types of fuel cell enhancing continuously the performance of this technology.

1.2 Principles and thermodynamics of fuel cell

The fuel cell is based on the spontaneous reaction between a fuel (e.g. H_2) and an oxidant (e.g. O_2) to produce electricity and heat in an electrochemical device [8]. The involved reactions occur at the anode (oxidation) and at the cathode (reduction). The electrons obtained from the fuel oxidation pass through an external circuit and reach the oxygen which underwent a reduction, figure 1.2. The anode and the cathode are connected through a membrane, called electrolyte, which allows only the ionic conductivity between the two electrodes in order to close the circuit.

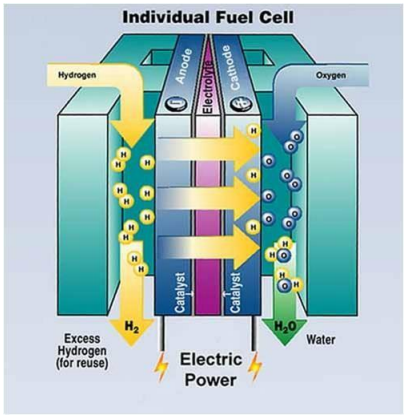

Figure 1.2: Scheme of fuel cell.

Beside the typology and focusing on H_2 and O_2 operating fuel cells, the reactions involved are:

at the cathode the O_2 is reduced to the ion O^{2-} (eq.1.1);

(eq.1.1) Cathode: $O_2 + 4e^- \rightarrow 2O^{2-}$

the ions obtained by the reduction, diffuse through the electrolyte and react with the fuel at the anode side (eq.1.2),

(eq.1.2) Anode: $2H_2 + 2O^{2-} \rightarrow 2H_2O + 4e^-$

The overall process is then:

(eq.1.3) Fuel cell: $2H_2 + O_2 \rightarrow 2H_2O$

By using the Nernst's law it is possible to find the electrode potential:

(eq.1.4) $$E_{electrode} = E^{\circ} - \frac{RT}{nF} ln \frac{(a_{Red})^{V_{red}}}{(a_{Ox})^{V_{Ox}}}$$

where E° is the potential under standard conditions, R the universal gas constant, T the temperature, *n* the exchanged electrons, F the Faraday constant, a_{Red} and a_{Ox}

the activities of reduced and oxidised compounds and V_{Red} and V_{Ox} are the stoichiometric coefficients.

The total cell potential is then calculated by the equation:

(eq.1.5) $$\Delta E_{cell} = E_{cathode} - E_{anode}$$

or can be obtained by the Nernst's equation using the reaction quotient Q:

(eq.1.6) $$\Delta E_{cell} = \Delta E° - \frac{RT}{nF} Q$$

Under steady state conditions, with constants pressure and temperature, it is possible to correlate the free Gibbs energy (ΔG) with the reversible electric work $(w_{el})_{rev}$:

(eq.1.7) $$\Delta G = -(w_{el})_{rev}$$

The maximum electric work corresponds to the free Gibbs energy change of the reaction. The potential ΔE can be calculated by:

(eq.1.8) $$\Delta E = -\frac{\Delta G}{nF}$$

If the reaction (eq.1.3) is conducted at 25°C and at 1 atm pressure, the reactants are in their standard state with ΔG = -237,14kJ/mol, n=2, F=96485.33 C/eq and the ΔE results 1.23V.

The ΔE resulting from equation (eq.1.8) is called open circuit voltage (OCV) and it is the potential at zero current. In a real device the OCV is lower than the theoretical value because it depends on the thermodynamic parameters of the

reaction and it is affected by the current induced polarization effects, figure 1.3. The potential loss is related to:

a) the overvoltage for charge transfer at the electrodes;

b) the mass transport overpotential;

c) the adsorption and desorption of the reactants;

d) the ohmic resistance of the electrolyte.

In a hydrogen/oxygen fuel cell device, the maximal theoretical efficiency is affected by the activation and the mass transport overpotential. Since ΔH is the total energy available and ΔG is the energy that can be converted, the theoretical efficiency can be expressed:

(eq.1.9) $$\varepsilon_r = \frac{\Delta G}{\Delta H} = 1 - \frac{T\Delta S}{\Delta H}$$

The maximum ε_r that could be achieved in a fuel cell under standard condition (25°C and 1 atm) and with liquid water as product is 83% [9][10].

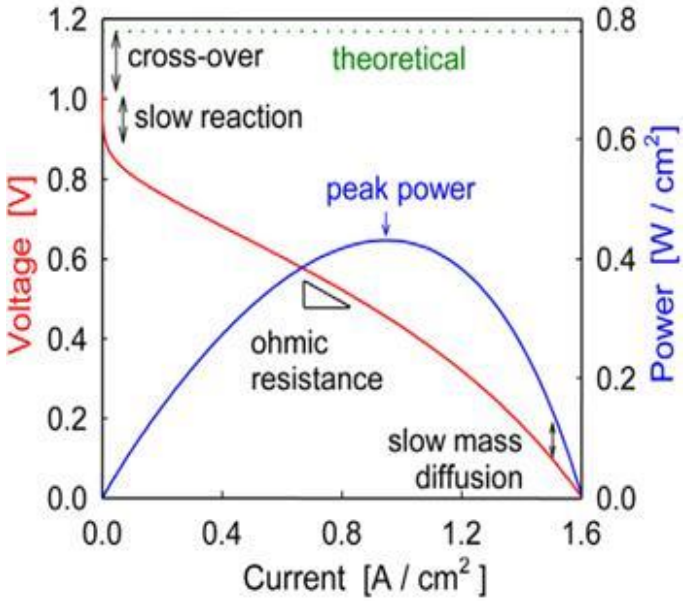

Figure 1.3: Polarization and power curve of a fuel cell [27].

The first example of fuel cell developed (by Sir William Robert Grove) was based on platinum electrodes, sulphuric acid as electrolyte and it worked close to room temperature. However the great interest in this technology has encouraged the development of different fuel cells. The fuel cells can be classified with respect of electrolytes, fuels used or by the working temperatures. It should be underlined that each type of fuel cell has usually a different final application (highly portable, stationary, isolated stand-alone system, emergency energy supply, etc.). The versatility of this technology is one of the main reasons of such a high interest.

Two main types of fuel cells could be identified by working temperature:

1) Low temperature fuel cells (80– 200°C)
2) High temperature fuel cells (600 – 1000°C)

1.3 Low temperature

1.3.1 Alkaline Fuel Cell: AFC [10][28]

In alkaline fuel cells an KOH aqueous solution is used as electrolyte (normally 30-45 wt%) and Ni or Pt as electrodes. The AFCs have the highest electrical efficiencies between the FCs due to their lower activation overvoltage at cathode induce by basic environment. The AFC was used for the first time in the Apollo missions (1960s) and then on the Space Shuttle Orbiter. The working temperatures and pressures greatly vary between developed designs, but the typical working temperatures are between 50°C to 200°C. The inexpensive materials used, such as nickel and KOH, and the high efficiency reached, are the most important merits of this technology. The main drawback is related to the high reactants purity needed in order to avoid quick drop down of the efficiency due to the formation of carbonate species in the electrolyte. Carbonates can form by interaction with the CO_2 present in air and in the fuel. Despite the great

success in 1950-60s the limitations of this technology have slightly decreased the attention of researcher on AFC. Now the interest on AFC is focused on developing new membranes, mainly polymeric based, with more resistance toward carbonate formation, high ion conductivity and chemical stability at basic high pH.

1.3.2 Proton Exchange Membrane Fuel Cell: PEMFC [8] [10][29]

Proton exchange membrane fuel cells are based on a proton-conducting polymers as electrolyte and Pt as electrodes, both cathode and anode. PEMFCs can work at low temperatures (80-105°C) but to have a good ionic conduction the membrane has to be kept hydrated. This is particularly important because the ionic conductivity is strictly related to the water content. The most famous and used polymer membrane is Nafion® developed by Dupont. It consists of a polytetrafluoroethylene-based structure sulphonated at the side chain in order to attract the water and allow the proton conduction. The strong fluorine-carbon bonds give a high stability under reducing and oxidising environments and also toward chemical attack. The high cost of the first generation of PEMFC was caused by the high platinum amount (28 mg/cm^2) resulting in slow diffusion of this technology. The great develop of PEMFC started with the decreasing of platinum amount and the increasing of power density. The peculiarities of PEMFC have led this type of FC as the better choice for portable application. Nowadays PEMFC are the most studied fuel cells and the research in this field is focused mainly on reducing the platinum amount and developing new membranes with high ionic conductivity, thermal stability and water management. The water management and fuel purity are still the main challenges of this technology due to the difficult to keep humidified the membrane above 80°C and to avoid poisoning at low temperatures.

1.3.3 Direct Methanol Fuel Cell: DMFC [17][30][31]

Direct methanol fuel cells are electrochemical devices which can be fed with methanol instead of hydrogen. The substitution of hydrogen with a methanol allows this technology to avoid all the costly and safety problems concerning the use of high pressure gas. Moreover methanol has a good electrochemical activity, very high energy density (4820 $Wh \cdot L^{-1}$ versus 180 Wh L^{-1} of hydrogen) and it is cheap. DMFC can have the same structure of AFCs and PEMFCs but the metal catalysts are slightly different. Usually anodes are based on Pt-Ru, Pt-Pd and Pt-Ni alloy but many other different metals are studied. Cathodes, due to the high activity toward oxygen reduction, are mainly based on Pt. The use of methanol however induces several drawbacks. These devices suffer from methanol permeation through the membranes which induces short-circuit and consequently a decrease of performance. Moreover the carbon deposition and the poisoning of metal catalysts force a higher metal electrocatalysts loading than the hydrogen fed FC. Researchers now are focusing on reduction of methanol crossover and on decreasing the noble metal loading. The great interests on these FCs are linked to the potential application on ultra-low power applications such as laptop computers and cell phones.

1.3.4 Phosphoric Acid Fuel Cell: PAFC [17][30]

In phosphoric acid fuel cells (PAFC) the phosphoric acid (>85% wt) is used as electrolyte. The electrodes are based on Pt and the working temperatures is around 150-200°C. Due to their relatively low cost, simple constructions and good chemical and electrochemical stability, the PAFC was one of the first FC developed for the market. The PAFC successful, started in 1960, was associated to Francis Thomas Bacon. Although the strong acid environment could lead to the premature corrosion of the FC materials, high phosphoric acid concentration

greatly decrease the water vapour pressure. This features allowed immobilizing the electrolyte into a porous matric resulting in a more simple PAFC design and avoiding the risk of excessive matrix drying under operation conditions. The power plant built based on this technology allowed to achieve electrical efficiency between 35% and 40% but including also the thermal energy the efficiency raised up to 85%. Despite the large success of PAFC in 1980-1990s the interests on this technology gradually decreased mainly due to the still high cost and insufficient stability in long term. The research now is focused on decreasing the noble metal loading by the use of iron alloy and in the reduction of working temperatures with the use of additives on electrolyte solution.

1.4 High temperature

1.4.1 Molten Carbonate Fuel Cell: MCFC[30]

Molten carbonate fuel cells (MCFC) are based on a liquid electrolyte, usually fused sodium and potassium (30-38 mol%) carbonate in a $LiAlO_2$ (62-70% mol) matrix. The liquid is immobilized in ceramic porous container. In order to keep melted the electrolyte and allow the ionic conduction, MCFCs have to operate at 600-700°C. For this reason, together with solid oxide fuel cell, they are considered a high temperature fuel cell. Because of the high temperature methane reforming can be carried out directly in the cell avoiding external reformers. Moreover, less expensive electrocatalysts, such as NiO (cathode) and Ni/Cr (anode) can be used as electrodes. One peculiar feature of MCFC is that, despite the other FC, the cathode side not only consumes the oxygen but also the carbon dioxide coming from the anode side through a special bypass. The main drawback is the corrosion of the materials due to the high temperature and the aggressive electrolyte which lead to an insufficient long period stability. The potential use of different fuels from hydrogen has attracted high interest on

MCFC. However the MCFC lifetime target for an industrial application (around 40,000 hours) is still a challenge. Nowadays many efforts have been done in order to enhance the lifetime of MCFS but still more work needs to be done.

1.4.2 Solid Oxide Fuel Cell: SOFCs

Solid oxide fuel cells (SOFC) are high temperature fuel cells characterized by a solid ceramic electrolyte. Due to this peculiarity, SOFCs need to operate at high temperature (800-1000°C), depending on the electrolyte. Cermets are the most diffuse anode (mainly Ni-Yttria-stabilized zirconia) whereas $La_{1-x}Sr_xMnO_3$ and $La_{1-x}Sr_xCoO_3$ perovskite are two of the most used cathodes. These cells do not present complications due a liquid electrolyte (as in MCFCs), or to water management (as in PEMFC), or to the fuel purity (as in all FCs using noble metals). The high operating temperature contributes to the great versatility of SOFCs: fuel versatility, possibility of internal reforming and auto-thermal reforming. The possibility to be fed with different fuels from hydrogen such as syngas, methane, ethanol, hydrocarbons and ammonia and the tolerance toward pollutants (SOFCs are not poisoned by carbon monoxide, as the low temperature fuel cells, and they can tolerate low amounts of sulphide), has highlighted the SOFC as the most suitable device for large stationary power plant applications, figure 1.4. Due to the operating temperature, an extremely high efficiency in combined co-generation cycles (coupled with gas turbine system, 70%, or by extracting heat and power, 70-90%) can be reached. The possibility to be fed with different fuels (fossil and renewable) with such high efficiency appears interesting with respect to the slow transition from fossil to renewable fuels. On the other hand, the high temperatures have significant drawbacks in terms of long-term stability (faster degradation of materials), cost of temperature tolerant materials and components, long start-up (due to slower heating rate) and high thermal

expansion. The research in Intermediate Temperature, IT-SOFC is focused on maintaining all the properties of a typical SOFC but meanwhile significantly lowering the operative temperatures (the target temperature range is 600-800°C). However the temperature decrease involves a series of problems caused by the consequent drop of catalytic activity and conductivity whereas the use of carbon based fuels requires catalysts with high reactivity and robust tolerance to impurities. The realization of an IT-SOFC requires thus the formulation of new specifically designed materials capable of assuring high performance at intermediate temperatures. Because of these problems many researchers have done great efforts in order to decrease the operation temperatures to 600°C or below.

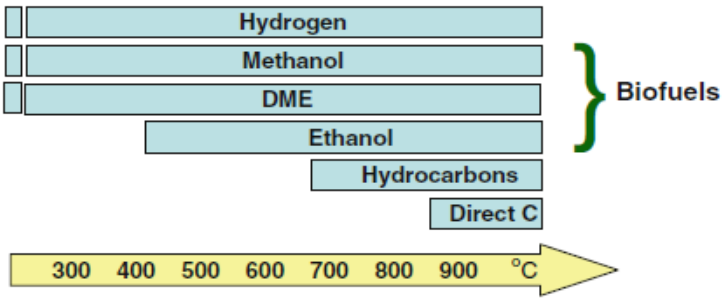

Figure 1.4: Fuel flexibility of high temperature fuel cells [18].

1.5 Solid Oxide Fuel Cell: principal elements [18]

The three principal elements of solid oxide fuel cells are the anode, the electrode where oxidation processes happen, the cathode, the electrode where reductive processes occur, and the electrolyte, the material which allows the ionic mobility between the two electrodes. In a SOFC, ionic conductivity can, in principle, be carried out both by oxygen and proton ions so giving rise to two types of ceramic

cells: protonic cells and oxygen anions cells. Both have merits and demerits but they can be summarized in the working temperatures and fuel flexibility. The SOFCs based on oxygen ion conduction operate at higher temperatures but can be fed with many fuels, while proton ion conduction cells could operate at lower temperatures but must be fuelled only with H_2. Moreover, conductivity in proton-based cells is strictly connected with the content of hydroxyl groups and thus is affected by humidity, thermal history, etc. In this PhD research work, only the oxygen ion conduction based cells are considered.

1.5.1 Method

The search for new and advanced materials able to meet the needs of this type of fuel cell is of primary importance for a commercial future of IT-SOFCs. The decreasing of working temperatures, as already cited in previous paragraph, could lead to a remarkable decreasing in FC performance.

Commonly two different approaches are used to improve the efficiency of solid oxide fuel cell. The first one, which is preferred in the SOFC Ni cermet based anodes, consists in maximizing the three phase boundaries (described in paragraph 1.5.5) area through the optimization of synthesis; the second approach, which seems most innovative and promising, is the use of mixed ionic electron conducting electrode (described in paragraph 1.5.6) instead of cermet based. The use of mixed ionic electron conducting electrode allows an extraordinary enhancement of active area since the electrochemical reactions and the oxygen ion could diffuse in whole the surface of electrode.

Besides increasing the efficiency, the replacement of Ni/YSZ with a mixed ionic electron conducting electrode could be fundamental to reduce the front deactivation problems. One of the most promising materials studied for this application are perovskite oxide.

A lots of perovskite based materials have been investigated in a systematic way and much progress have been made. In spite of the real and interesting opportunities offered by perovskites, the obtained devices are still far from the criteria of commercialization. Currently perovskites show too low performance at intermediate temperature (600-800°C); moreover the catalytic activity of these materials with respect to real biogas still needs to be properly investigated and optimized.

The aim of this research project is the development of new materials, highly performant at intermediate temperature (600-800°C), capable of high efficiency, stability and resistance to poisoning. These electrodes will be the basis for the development of intermediate temperatures SOFC directly fed with biogas.

1.5.2 Anode

The anode is the site where the fuel is oxidised. It must fulfil several characteristics: good activity towards the fuel oxidation, good ionic conductivity, good electronic conductivity, stability in severe reducing atmosphere, appropriate porosity, chemical compatibility with the electrolyte, suitable thermal expansion coefficient, resistance to carbon deposition and sulphur poisoning. The anode is the key component that allows using different fuels in SOFCs.

At the moment the most common anodes for SOFCs consist of a cermet (ceramic-metallic material) constituted by a metallic component dispersed into a matrix of electrolyte material, usually yttria stabilized zirconia (YSZ). The most used cermet anode is Ni-YSZ where YSZ has typically 8% Y_2O_3 and 92% ZrO_2. Nickel is an inexpensive element with a great activity towards hydrogen and hydrocarbon oxidation and a good electronic conduction; YSZ, in contrast, is an oxide with a high chemical and mechanical stability and a good ionic conduction at high

temperature. These anodes are designed to accomplish the hydrogen oxidation and hydrocarbon reforming with high electronic conductivity [13][32]. However, Ni-based anodes do have some drawbacks, such as the sinterability, the reactivity with some La containing electrolytes, the low tolerance to sulfur and to the deposition of carbon when hydrocarbons are used as fuel and the steam levels are low [33]. Indeed, carbon formation is usually thermodynamically favoured with hydrocarbon fuels at the low O_2 fugacity that exists in the anode compartment [10]. Copper has also been proposed as an alternative to Ni, and also CeO_2 is added to provide the requested catalytic activity, and to reduce the carbon formation [34]. Copper in fact, does not catalyse the C-C bond formation [35]. However, a recent study has shown the destabilization of YSZ when copper compounds are also present [36]. Another possible limit of cermet based electrodes is the number of accessible active sites. In fact, the electrodic processes (fuel oxidation, oxygen reduction) require the intimate contact between the following three different elements: the electron conductor (e.g. Ni in anodes), the ionic conductor (e.g. YSZ) and the reactants (e.g. H_2). This condition is called three phase boundaries (TPB) requirement. Research focuses on new materials capable of meeting the above mentioned requirements. Among the most promising materials perovskite based ones are particularly interesting because of their capability to meet all the SOFC demands and to go beyond the actual cermet limits. Although their development is affected by the lower performance when compared with the cermet Ni-YSZ, some promising result has been demonstrated on $Pr_{0.5}Ba_{0.5}MnO_{3-\delta}$, $La_{0.5}Sr_{0.5}Ti_{0.75}Ni_{0.25}O_3$, 6.3%Ni-8.3%GDC-$La_{0.57}Sr_{0.15}TiO_3$, $La_2Sr_4Ti_6O_{19}$, Ni-GDC 30% $La_{0.2}Sr_{0.8}TiO_3$ 70% wt and also double perovskite such as Sr_2MgMoO_{6-d}, Sr_2CoMoO_6 and $Sr_2TiNi_{0.5}Mo_{0.5}O_6$ [19][35][37][38] [39][40][41].

1.5.3 Cathode

The cathode is the electrode where oxygen reduction is performed. Like the anode, also the cathode must achieve many features: good activity toward the oxygen reduction, good electronic conduction, chemical compatibility with the electrolyte and a suitable thermal expansion. Lanthanum strontium manganites $(La_{1-x}Sr_x)MnO_3$, (LSM) was the first material studied due to its high cathode activity and a great stability with YSZ [18]. LSM has a high electronic conductibility but it is a poor ionic conductor; because of this reason, it must be mixed with a good ion conductor, usually the electrolyte. As for the cermet anode, also the LSM/YSZ cathode suffers from three phase boundaries limit. Another drawback with LSM is the reactivity with the interconnects (mainly based on Cr). New promising materials have been developed paying particular attention to intermediate operative temperatures: $(La_{1-x}Sr_x)CoO_3$ (LCF), $(La_{1-x}Sr_x)FeO_3$ (LSF) and $(La_{1-x}Sr_x)(Co_{1-y}Fe_y)O_3$ (LSCF) [18]. The innovative characters of these new materials are mainly focused on two aspects: the capability to be electrocatalytically active at intermediate temperatures (600 to 800°C), and the possibility to operate as mixed ionic and electronic conductors, solving the triple phase boundaries. However, all La and Sr containing electrodes, suffer of reactivity toward YSZ inducing the formation of insulating phases, such as $La_2Zr_2O_7$ and $SrZrO_3$. At intermediate temperatures the use of LSF, LSC and LSCF with YSZ electrolyte is compulsory coupled with an interlayer of gadolinium doped ceria (GDC) [18].

1.5.4 Electrolyte

As mentioned, the electrolyte of SOFC, has to guarantee good ion conduction and good chemical and mechanical stability towards electrodes, reactants and temperatures. The ceramic electrolyte is the responsible of the high temperature

required for SOFC due to the ionic transport processes. The ionic mobility in the ceramic electrolyte is the most impactful process responsible of the greater ohmic loss. Because of this reason, particular attention is devoted to obtain the thinner but, at the same time gasses impermeable, membrane. The contact with gasses and electrodes can also induce shorts circuits capable of dropping the FC efficiency. Skinner et al. reported that an adequate area specific resistance (ASR) should be less than 0.15 Ω cm^2 for an electrolyte and the ion conductivity should be at least 0.1 S/cm at working conditions [42][43]. The widely used ceramic membrane is the yttria stabilized zirconia (YSZ), 8% Y_2O_3 and 92% ZrO_2. It has a cubic structure and a high mechanical and chemical stability under oxidising and reducing environments [44]. The most promising electrolyte for IT option is the cubic fluorite structure: gadolinium doped ceria (GDC). The maximum ionic conductivity occurs at 10-20 mol% Gd doping [42]. The GDC electrolyte could permit the use of less expensive materials such as stainless steel with the consequently decreasing of the device cost [8].

The material that shows a suitable ionic conductibility at low operating temperature is $La_{1-x}Sr_xGa_{1-y}MgO_3$. It has attracted many attentions due its properties but it still suffers of durability problems with electrodes and it is extremely expensive compare with YSZ and GDC, figure 1.5.

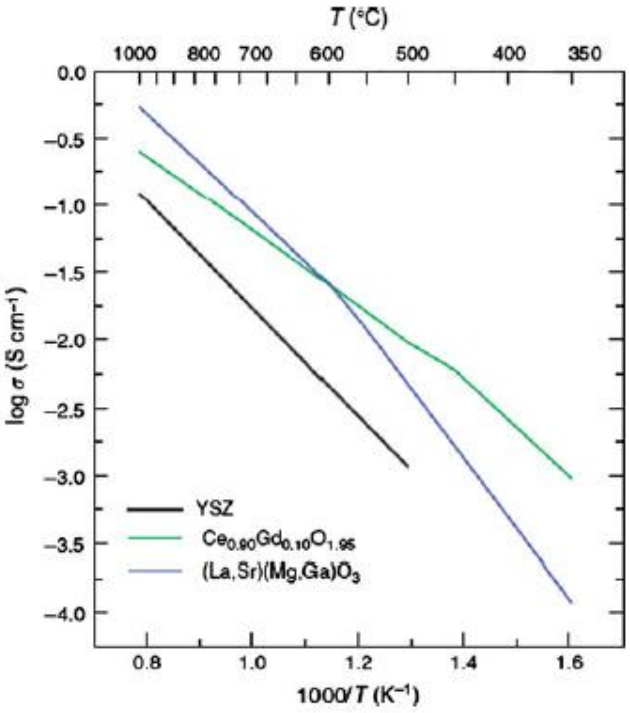

Figure 1.5: Electrolytes conductivity as a function of temperature [45].

1.5.5 Three phase boundary [43][46]

The "three phase boundary" (TPB) is the site where ions, electrons and gas molecules get in contact. The phenomenon was observed for the first time in 1920s by Alfred Schmidt and he named this process "gas-diffusion reaction". In traditional systems, where electrodes are purely electronic conductors and electrolytes are pure ionic conductor, the electrochemical reactions occur only at the intersection of them. The gas connectivity to these intersections is essential in order to allow the electrochemical processes. Below is reported the proposed mechanism for the three phase boundaries in a cathode, figure 1.6.

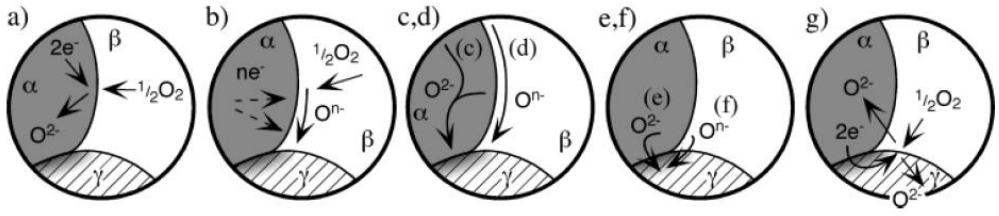

Figure 1.6: Schematic illustration of three phase boundary (TPB): (a) Incorporation of oxygen into the bulk of the electronic phase (if mixed conducting); (b) adsorption and/or partial reduction of oxygen on the surface of the electronic phase; (c) bulk or (d) surface transport of O^{2-} or O^{n-}, respectively, to the α/β interface, (e) electrochemical charge transfer of O^{2-} or (f) combinations of O^{n-} and e^-, respectively, across the α/β interface, and (g) rates of one or more of these mechanisms wherein the electrolyte itself is active for generation and transport of electro-active oxygen species [46].

Although TPB-based systems are extensively present in many anodes and cathodes with good results, the regions where the electrochemical reactions perform are limited. This further limit induced several researchers to improve the microstructure of electrodes. Another solution to this problem is the use of mixed ion-electron conductors (MIECs), i.e. of materials which allow simultaneously the electrical and ionic conductivity in whole the surface.

1.5.6 Mixed Ionic Electronic Conductor (MIEC) [16][43]

A mixed ionic electronic conductor is a material with both ionic and electronic conduction propriety, figure 1.7. This peculiarity allows to overcome the limit of three boundaries phase of SOFC so as to significantly increasing the material active sites. The mixed ion conductor feature could enhance the electrochemical reaction on the anode surface reducing the problems of gas diffusion thought the porous electrode [23]. A larger number of materials have been studied as SOFC MIEC electrodes and among them perovskite oxides are among the most studied: $La_{1-x}Sr_xFeO_3$ (LSF), $La_{1-x}Sr_xCoO_3$ (LSC), $La_{1-x}Sr_xFe_{1-y}Co_yO_3$ (LSCF) and $Ba_{0.5}Sr_{0.5}Co_{0.6}Fe_{0.4}O_{3-d}$ [16][47].

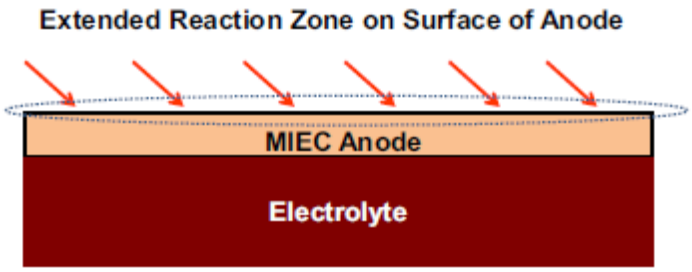

Figure 1.7: Schematic illustration of MIEC surface active sites [23].

1.5.7 Current Collector

The current collector is a layer printed on the electrodes with the function of collecting electrons in a system with a low electronic conductibility. The materials have to be stable under the operative conditions, to be characterized by a high electronic condition and a suitable thermal expansion.

1.5.8 Interconnection [18][42]

The interconnect is the element capable of guaranteeing the fuel and oxidant gases separation and of collecting the current from the electrodes. It must have a high electrical and thermal conductivity, a good chemical stability under oxidising and reducing environments; moreover, it has to be easily and cheaply manufacturable. Lanthanum chromite-based perovskite ($LaCrO_3$) is the most popular interconnect used at high temperature. Usually $LaCrO_3$ is doped with Sr or Ca in order to reduce the sintering temperature and to enhance conductivity. $LaCrO_3$ has been extensively studied but it still suffers of issues concerning the electrodes poisoning (in long term operations), the high cost and difficulty in fabrication. For this reasons the possible use of metallic interconnects, allowed by a decreasing working temperatures in IT-devices, will be a great breakthrough in the SOFC technology.

1.5.9 SOFC Cell Design

The peculiar properties and performance of SOFCs can be deeply modified, beside material optimization, by selecting one of the different possible architectures, figure 1.8, each one characterized by merits and demerits. The supporting layer has usually a thickness of 1-5 mm while the other components are considerably thinner (typically 5-50 μm) [16]. Reducing the thickness in fact generally decreases cost and enhances the cell performance (lower polarization resistance). Historically, electrolyte supported cell were the most diffuse due to the simple fabrication and elevated mechanical robustness. The electrolytes were usually between 50 and 500 μm and through screen printing the electrodes deposition was easily carried out [16]. However the large electrolyte thickness induced remarkable performance loss. Cathode supported cell were explored by Siemens-Westinghouse due to their historical high performance in terms of number of hours operation (the longest running demonstration was 36,750 hours). However in spite of good industrial successful, due to the high cathode cost (high rare-earth content) the enthusiasm of this design was slowly waned. Nowadays the most popular design is the anode supported cells, due to fewer problems concerning the electrolyte resistance (the electrolyte layer is very thin) and, additionally, a thicker anode permits the fuel processing directly into the cell. More recent but extremely promising are the ceramic and metal supported cells. In ceramic supported cells the support is inert and with a similar thermal expansion with the cell. In addition the ceramic support allows higher operating temperature than metal one also avoiding the typical electrode degradation induced by chromium vapour of metals alloy. The metal supported cell suffers from shorter lifetime than ceramic supported one. On other hand the metal supported cell, due to high electrical conductivity, high thermal resistance and high strength of the support, could find application on systems where the thermal

cycling are more important than the cell lifetime. The new technologies coupled with intermediate temperature materials, allow the developed of low cost substrate supported cell.

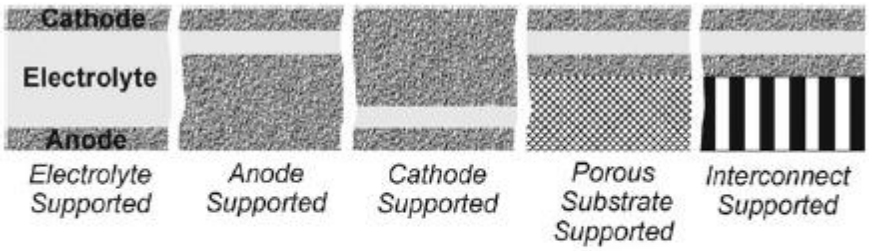

Figure 1.8: Illustration of SOFC support architectures [42].

The uses of solid elements (electrolyte, anode and cathode) have paved the way to the development of many designs in order to optimize the fluid-dynamics and the heat exchange [9].

The three main designs diffuse are:

1. Siemens–Westinghouse tubular cell;
2. Sulzer-Hexis cell;
3. planar cell.

The tubular design has been developed by Westinghouse (Siemens-Westinghouse) in the late 1980s and it was the first breakthrough achieved in SOFC technology [18]. It is the most promising design for high temperature SOFC and it has a self-sealing structure, where fuel and air flow inside or outside the tubes depending of the configurations, figure 1.9.

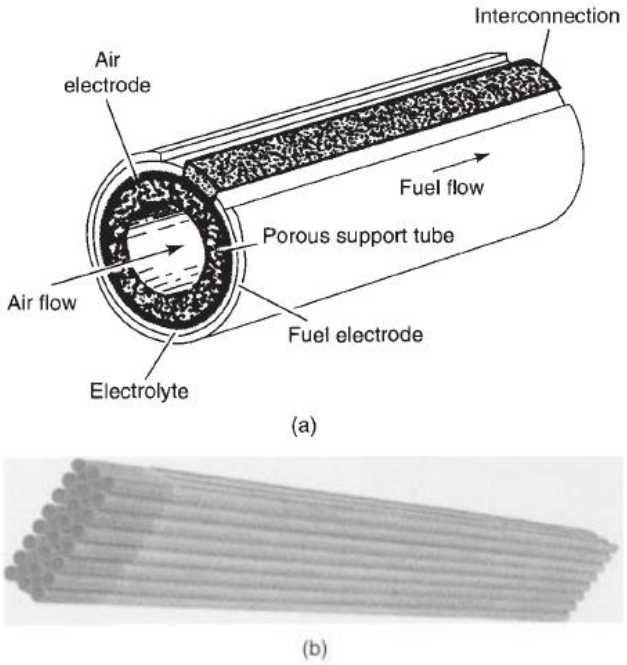

Figure 1.9: Tubular design a) single tubular and b) bundle of 24 tubular SOFCs [30].

The Sulzer-Hexis design (Hear exchanger integrated stack) is under investigation for the small co-generations plants. The interconnector works as current collector and as heat exchanger, figure 1.10.

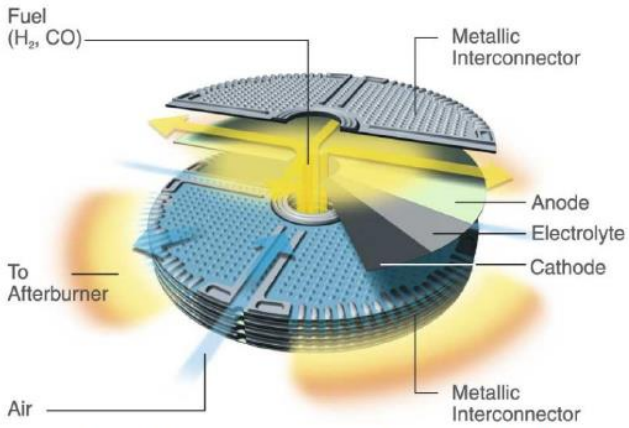

Figure 1.10: Sulzer - Hexis design [48].

The planar celli is the most diffuse due to the low cost and the simpler design, figure 1.11. It has some issues concerning the sealant and the interconnection but

it is ideal for intermediate temperature fuel cell. At intermediate temperature, in fact, the use of stainless steel becomes possible with greater improvement on SOFC realization.

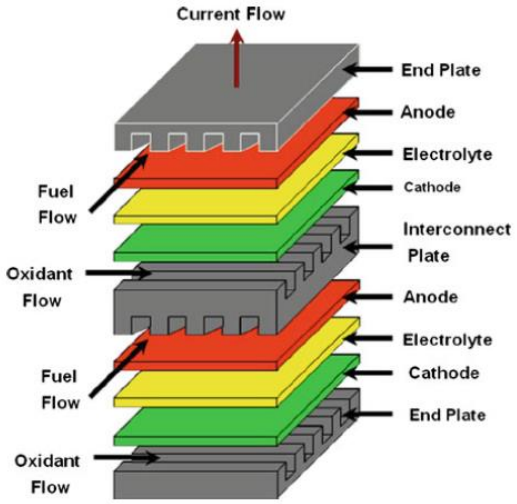

Figure 1.11: Planar design [48].

1.5.10 Single-Chamber SOFCs [30]

An interesting variant of the typical SOFC is the single-chamber SOFC in which the reactants are fed together (not separate) in the cell chamber. This interesting design allow to greatly simplify the cell fabrication and decreasing the avoiding the sealing problems between anodic and cathodic side. Since avoiding the direct reaction between fuel and air is not possible in this design, the electrodes have to be extremely selective toward their reaction (anode with oxidation, and cathode with reduction) in order to obtain a decent performance.

1.5.11 Electrodes Deposition: Screen printing [49][50]

The electrodes deposition is one crucial step for a low cost SOFC fabrication. Many techniques are available to obtain layers with controlled morphology and thickness and among them the screen printing has been recognised as the most promising one. In general this procedure is composed by the following steps: the electrode containing ink is placed in a plastic mask with and suitable mesh. A coating blade is then pressed on the mask and moved along the substrate, figure 1.12. Once the ink is deposited on substrate, the cell is heated slowly until whole the ink solvent is evaporated.

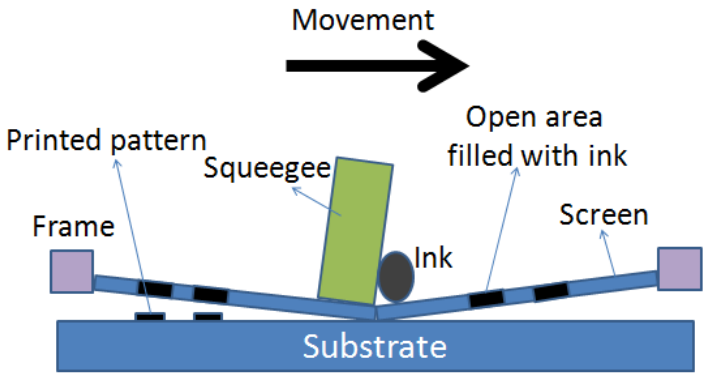

Figure 1.12: screen printing machine

The ink recipe, the numbers of deposition and the type of mask are among the main parameters that can be tuned in order to control the electrode morphology. After the deposition a high temperature treatment is required in order to achieve an appropriate adhesion.

1.5.12 Ink

The ink is the vehicle through which the powder prepared is deposited on the substrate. It is based on different components, such as the powder, a binder and a solvent. The powder must have a proper dimension and dispersion and has to be homogenous dispersed into the organic solvent. The binder guarantees the links between the particles after the solvent evaporation and before the thermal treatment adhesion. An optimized amount of binder is essential in order to control the final porosity and the fabrication steps.

1.5.13 Infiltration [51]

The infiltration is a widely used technique based on the penetration of an active material, through solution, into backbone architecture, figure 1.13. This technique allows combining materials with different properties in order to enhance the performance of the final composite. It is considered a promising process for inexpensive SOFC electrodes preparation. The three main elements of the infiltration process are: the backbone, the permeated material and the vehicle (solvent). The backbone is the scaffold of the final material and it must have a good porosity and tortuosity but also a good adhesion with the support (the electrolyte). For this reason, a proper thermal treatment has to be performed with the purpose of keeping a suitable porosity. The active material has to be dissolved or dispersed in a solvent before to be infiltrated into the backbone. The morphology of the infiltrated layer has a great impact on the final performance. The concentration, the viscosity, the selected precursors (nitrates, acetate, etc.) and the surfactant are the main parameters allowing to control the infiltration process [52].

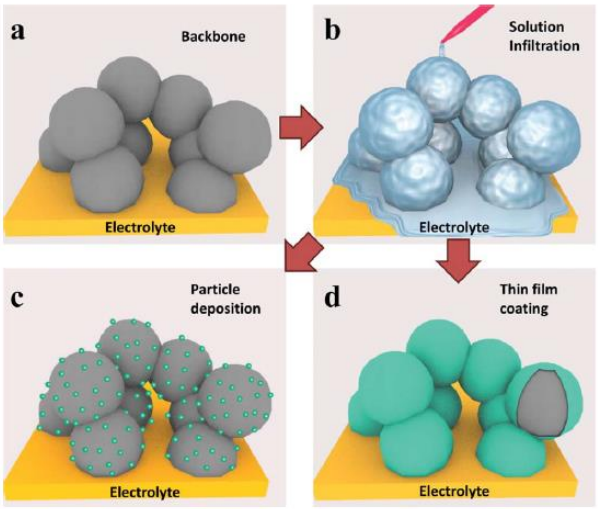

Figure 1.13: Illustration of infiltration steps [52].

1.5.14 Bio-Fuels and Fuel Processing [53][54]

The fuel is the most important element in a fuel cell system and the anode is the key component that allows using different fuels. In a SOFC, fuels such as syngas, methane, methanol, ethanol, and some light hydrocarbons can be used as an alternative of high purity hydrogen, avoiding problems related to the production, storage, distribution and security. Fuel flexibility is one of the key aspects that may allow SOFCs to a commercial development. SOFCs are also not poisoned by carbon monoxide, which is used as a fuel, and they can tolerate low quantities of sulphide [10][13][55]. The primary reason for the improved fuel flexibility of SOFCs is their high operating temperature, which accelerates the electrode reaction rates. [56] However, these fuels need to be converted before being available for the electro-catalytic oxidation in the cell. For this reason the reforming of carbon based fuels has to be done. In most cases reforming is done externally, obtaining syngas just before the solid oxide fuel cell chamber. However, the direct reforming of fuels (internal reforming) is considerably recommended assuring a lower complexity of the system (cost cutback) and a greater temperature control of reactions. In fact, the heat produced during

oxidations reactions provides directly energy to the highly endothermic process of reforming, table 1.1, resulting in a considerably lower thermal energy loss (enhancement of overall efficiency).

Table 1.1: Main reactions involved in the reforming [51].

Reaction		Reaction enthalpy at 1100 K (kJ mol^{-1})
$CH_4 + CO_2 \rightarrow 2\,H_2 + 2CO$	(1)	259
$CH_4 + 1/2O_2 \rightarrow 2\,H_2 + CO$	(2)	−23
$CH_4 + 2O_2 \rightarrow 2H_2O + CO_2$	(3)	−802
$CH_4 + H_2O \rightarrow 3\,H_2 + CO$	(4)	226
$CH_4 \rightarrow C + 2\,H_2$	(5)	90
$2CO \rightarrow C + CO_2$	(6)	−170
$CO + H_2O \rightarrow H_2 + CO_2$	(7)	−34
$CO + 1/2O_2 \rightarrow CO_2$	(8)	−282
$H_2 + 1/2O_2 \rightarrow H_2O$	(9)	−248

Among the fuels, biogas and biofuels are the most attractive. The use of biofuels, in fact, is highly recommended due to their low environmental impact, the possibility to have multiple renewable sources (or municipal organic wastes) and the ability to warrantee a neutral carbon balance, figure 1.14 [54].

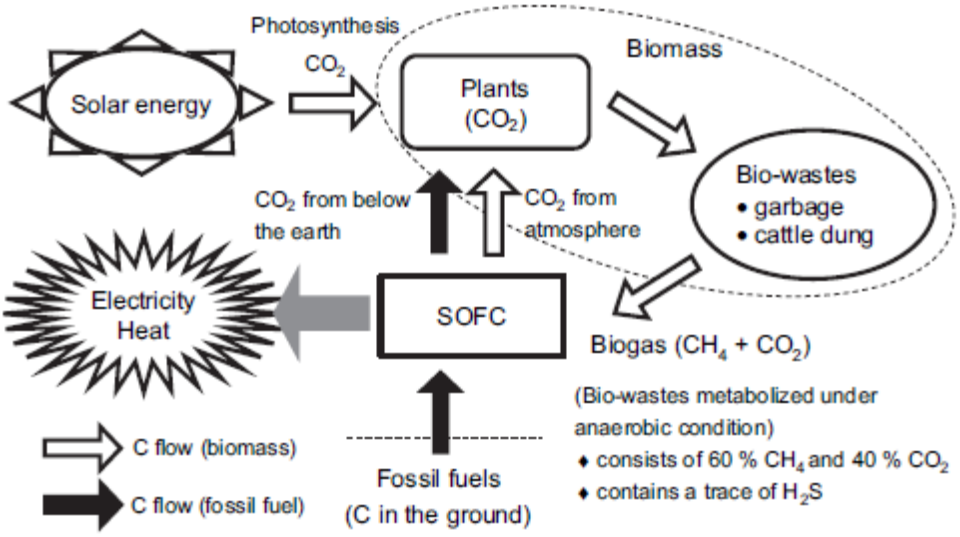

Figure 1.14: Heat and electricity generation form SOFC technology starting from renewable resources [54].

Among the biofuel candidates, bio-gas (CH_4+CO_2) is characterized by high availability and easy management. The bio-gas composition is reported in table 1.2. Moreover, in biogas-fed SOFC the problem of low methane concentration, relevant when bio-gas is used in classical gas engine, is overcome. In fact, in literature is reported that a SOFC system could generate power even at 20% CH_4 to CO_2 whereas a combustion engine could not [57]. In theoretical study two identical plants fed with different fuels (hydrogen and natural gas) have been investigated; the comparison revealed that when the methane reforming (eq.1.20) is performed into the SOFC device (internal reforming) the total output energy for of the plant is greater [58].

(eq.1.20) $$CH_4 + CO_2 \rightarrow 2CO + 2H_2$$

At the industrial level there is high attention for this kind of system but nowadays there are still some problems that have to be resolved: the carbon formation (table 1.1) and the sulphur contamination [30][54].

Table 1.2: Bio gas composition [59].

Compound	Landfill gas (vol %)	Bio gas from anaerobic digestion (vol %)
CH_4	35-65	53-70
H_2	0-3	0
CO_2	15-50	30-47
H_2S	0-100 ppm	0-10000 ppm
NH_3	5 ppm	<100 ppm

1.6 Target of Research

The aim of this research is to develop advanced perovskite based materials to be used as electrodes in intermediate temperatures (600-800°C) Solid Oxide Fuel Cells (SOFCs) fed with bio-gas. Particular attention was devoted on limiting, or avoiding when possible, critical raw materials and the high catalytic activity towards methane.

Chapter 2

2.1 Introduction to chapter 2

In this chapter the perovskite oxides, the design strategies and the synthesis used for the investigated compounds are presented.

2.2 Perovskite-based oxides [18]

Perovskites are a particular type of oxide with a general formula ABO_3 where A and B are two different cations. The first mineral of this type was discovered in 1839 by Gustav Rose in the Ural Mountains of Russia; it was a double oxide of calcium and titanium, $CaTiO_3$, and the name came from the mineral collector and Minister of the Russian Court Lev Perovski. The ideal perovskite structure ABO_3 is cubic with a larger 12-coordinated A cation, and a smaller 6-coordinated B cation, figure 2.1. The cations A and B can assume different combination of charge, e.g. $1^+/5^+$, $2^+/4^+$ and 3^+3^+.

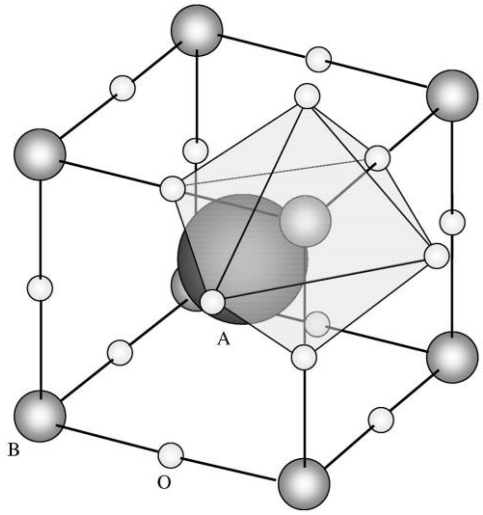

Figure 2.1: oxide structure [60].

In the ideal perovskite, in which atom are in close contact, the distance between the B cation centre and oxygen is $\frac{a}{2}$, where a is the unit cell parameter, and the distance between A cation and oxygen is $\frac{a}{\sqrt{2}}$. We can then derive the equation (eq. 2.1):

(eq. 2.1) $$r_A + r_O = \sqrt{2}(r_B + r_O)$$

where r_A, r_B, r_O are the radius of A cation, B cation and oxygen respectively.

In 1926 Victor Goldschmidt proposed the t-factor which is a parameter that allows to estimate the deviation from ideal structure, (eq. 2.2).

(eq. 2.2) $$t = \frac{r_A + r_O}{\sqrt{2}(r_B + r_O)}$$

A perovskite based compound has the t value between 0.80 and 1.10, where the ideal perovskite then has t-factor of 1. A value >1 reveals a distorted structure induced by a big cation, while a value between 0.9 and 0.75 reveals a distortion induced by a small A cation. When the value is $0.9 \leq t \leq 1$ the perovskite preserve the cubic structure. Only few perovskites have cubic structures, instead many of them have a slightly distorted structure (e.g. hexagonal or orthorhombic).

Beyond the simple ABO_3 structure, perovskites can present show complex configurations, such as the Ruddelsden Popper's (RP) structure, A_2BO_4 or $(AO)_m(ABO_3)$ also called K_2NiF_4, in which the perovskite structure is alternated with a rock-salt plane, or the superstructures such as $A_2B_2O_6$. In the RP perovskites, in particular, the rock-salt planes should greatly favour the ionic mobility and thus ionic conductivity, figure 2.2.

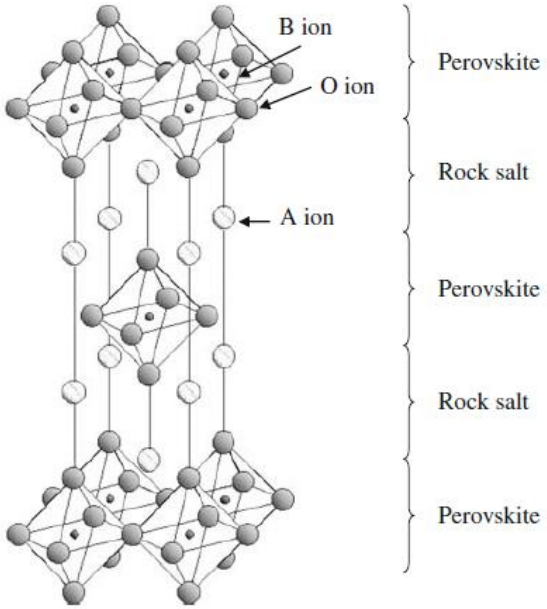

Figure 2.2: K_2NiF_4 perovskite type [18].

Perovskites are very versatile and this is mainly due their peculiar capability of hosting over 90% of period table elements into the structure, figure 2.3. Perovskites find application in many fields such as catalysis, photo-catalysis, ionic and/or electronic conductor, sensors, electro-catalysis, ceramic membranes, etc. Some of the most famous compounds are: superconductive $Ba_2YCu_3O_7$, ferroelectric $BaTiO_3$ based oxide, gas sensor $SrTiO_3$, catalysts for oxidation $LaMnO_3$ and $LaCoO_3$, piezoelectric $Pb(Zr,Ti)O_3$ and electrode $La_{0.6}Sr_{0.4}CoO_3$ [25][61].

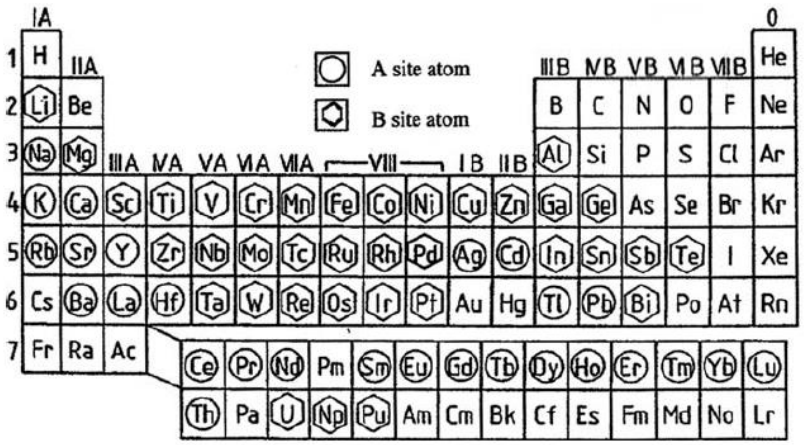

Figure 2.3: Chemical elements that can occupy sites in the perovskite [18].

Perovskite proprieties can be tuned through the use of dopants in A and/or in B sites. The doping strategy is considered crucial for promoting the desired property. A doped compound is generally reported as $A'_{(1-x)}A''_{(x)}B'_{(1-y)}B''_{(y)}O_{3-\delta}$ where the dopants are A" and B", respectively, for A and B site elements. When an aliovalent doping occurs, the oxygen amount is slightly different from the ideal, which can be above or below the stoichiometric value. The valence states un-balance can induce the formation of oxygen vacancies and/or promote unusual oxidation states such as Cu(III), Co(IV) and Fe(IV), so creating powerful redox couples [62][63][64][65].

2.3 Perovskite in SOFC [18]

Perovskites have been considered for SOFC application since decades. Particular attention was paid to cobalt and manganese based perovskites due to their good electrical conductivity and activity in oxygen reduction; $LaCrO_3$ is a promising interconnector at high temperatures and $LaGaO_3$ based perovskites are used as electrolytes for intermediate temperatures. $La_{1-x}A_xCrO_3$ systems have been considered for applications as SOFC anode due to their reasonable electronic conductivity and stability at high temperatures under both oxidizing and

reducing conditions. Improvements in performance were reached through partial substitution of Cr by transition metal ions such as Mn, Fe, V, and Ni. A promising Cr/Mn based system, $(La/Sr)_{1-x}Cr_{0.5}Mn_{0.5}O_{3-\delta}$ ($0< x<0.1$), was reported by Irvine and Tao but the oxide ion conductivity was still relatively low [33][66][67]. Composite systems containing electrolyte (Gadolinium-doped ceria, GDC), metal (Ni, Cu) and perovskite were proposed to improve performance of anode with hydrocarbon fuels, e.g. $(La/Sr)_{1-x}Cr_{0.5}Mn_{0.5}O_{3-\delta}$/GDC with a small amount of Ni (4%). In this composite system the presence of low levels of nickel introduces additional catalytic performance but avoiding problems of carbon formation [33]. Some other promising anodes are $La_{1-x}Sr_xCr_{1-y}Ni_yO_{3-\delta}$, $Pr_{0.7}Sr_{0.3}Cr_{0.9}Ni_{0.1}O_{3-\delta}$, $Sr_2Mg_{1-x}Mn_xMoO_{6-\delta}$ and $CaV_{0.5}Mo_{0.5}O_{3-\delta}$. Mo-based perovskites could be a good candidates for sulphur tolerant anodes has reported by Huang et al. but a ceria-based buffer layer is required to avoid Mo diffusing into electrolyte [68][69][70][71].

The perovskite proprieties could be so different that even the concept of solid oxide fuel cell completed based on perovskite has been proposed [18].

2.4 Critical Raw Material

Before going deeper in study of investigated compounds the elements selection has to be discussed. In fact although almost the total elements of period table could be used in order to fulfil the SOFC requirements, some elements have been identify as critical raw materials (CRM) due to their economic importance and difficult supply. A relevant characteristic of the materials developed in this work, in fact, is the low environmental and economic impact. Following the suggestion of the EU report the perovskite design and optimization was carried out avoiding platinum group metals and minimizing or avoiding rare earth elements, figure 2.4 [72].

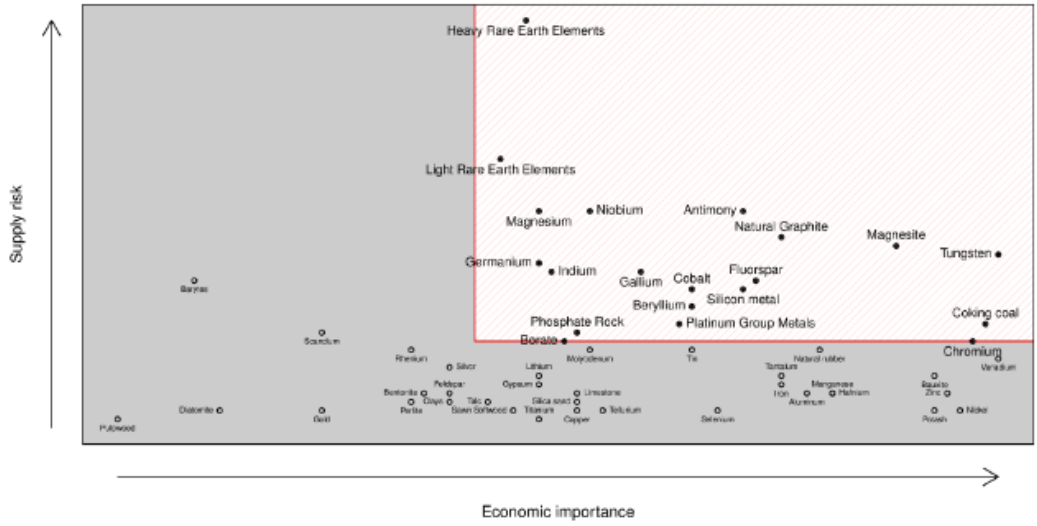

Figure 2.4: Diagram with 41 critical raw materials for EU [72].

This is a particular task and demanding requirement, considering, that the scientific research in IT-SOFCs is, up to now, focussed on La based perovskites.

2.5 Materials selected and investigated

In this work two different perovskite-based materials have been studied for SOFC application, titanates and cobaltites. Titanates are considered one the most promising anode materials for SOFC application. They show a great stability towards reductive environments and pollutants (e.g. H_2S), but suffer of some weakness such as catalytic activity and electron conductibility. Cobaltites are well known to be very active in cathodic reactions but they have also high activity towards oxidation suggesting the possibility to be used in symmetric cell under appropriate conditions.

This work focused on the developing of ABO_3 Ti-based perovskites doped with molybdenum and iron and K_2NiF_4-type cobalt based perovskites.

2.5.1 Ti-Based perovskite

$SrTiO_3$ systems have received a lot of attention due to the intrinsic stability of such materials at high temperatures under reducing conditions. Titanates do not

have a high conductivity but this can be enhanced through a suitable doping with Nb (for Ti) and La (for Sr), e.g. $Sr_{1-x/2}Ti_{1-x}Nb_xO_3$ and $Sr_{1-3x/2}La_xTiO_3$. Other kind of doping such as Ba, Sr, Ca, (for Sr) and Ni, Mg, Mn, Fe, Cr, In, Sn (for Ti) were also investigated with the aim of enhancing the fuel cell anode performance [20][32][33][73]. Titanates are the perovskite most studied as anode. Among all the formulation studied, $La_{0.4}Sr_{0.6}TiO_{3-\delta}$ has shown one of the best performances, about 450 mW/cm^{-2} at 850°C with CH_4 and trace of H_2S. This compound resulted interesting because the presence of sulphide increases the performance instead of poisoning the catalyst. The partial substitution of Sr by Ba in $La_{1-x}Sr_xTiO_3$ is reported not to affect the chemical stability of the compound and, at the same time, to improve the activity when H_2S is present in H_2 and CH_4 feed [74]. Another interesting anode is $La_{0.2}Sr_{0.8}TiO_3$+NiO-SDC+NiO-YSZ where SDC is samarium doped ceria and YSZ is yttria stabilized zirconia. This composite achieves 850 mW/cm^{-2} at 800°C with pure hydrogen feed. Small traces of H_2S (100 ppm) decrease the power of that cell only to 700 mW/cm^{-2}. Since the power benchmark for the commercialization of SOFC is 500mW/cm^{-2}, titanates result highly attractive. Although these compounds have good characteristic as anode for SOFC, they have still low electronic conductivity. The common approaches used in order to improve the conductivity are the material doping and the creation of a composite. Frequently both these approaches are used simultaneously. Doping with rare earths (RE) or with platinum group metals (PGM) is widely used for this purpose, but this causes consequently an increasing cost and push to find new solution of this issue.

2.5.1.1 Mo-doping

In spite of being known for a long time, molybdates are the newest class of perovskite materials proposed as anode for SOFC. Molybdates, especially $SrMoO_3$

and $BaMoO_3$, have the highest electronic conductivity (about 10^4 S/cm at 25°C) among ceramic materials. This peculiarity has attracted the attention of many researchers for their potential application in SOFC. Unfortunately, molybdenum is not compatible with all elements in a perovskite structure. This is due to its big ionic radius and to its tendency to be stable in high oxidation states (+4, +6). The most promising molybdenum based anode is $Sr_2MgMoO_{6-\delta}$ which is a double perovskite, $A_2B'B''O_6$. Most of the Mo-based perovskite anodes are double and strong reducing treatments are required in order to obtain the correct phase [39]. However, molybdenum oxides (MoO_2) are good hydrocarbons reforming catalysts and they have fewer problems with carbon poisoning when compared with Ni-based catalyst. [75] Anodes based on MoO_2 have demonstrated remarkable power output (> 3W/cm²) when fed with long hydrocarbon (n-dodecane) at 750°C without carbon deposition over 24 hours.[76]. Titanates doped with molybdenum have been studied as a possible solution to the chemical instability in working conditions (Ti) and the low electronic conduction (Mo) [41].

2.5.1.2 Fe-doping

Fe-doped titanates have been extensively studied for oxygen sensor application and oxygen membrane due their good electronic and ionic conduction properties and high thermal stability [77][78][79][80]. Recently $SrTi_{1-x}Fe_xO_3$ based materials have shown a p-type electronic conductor behaviour under cathodic conditions (high pO_2 pressure) but change to n-type electronic conductors under reducing conditions (low pO_2 pressure) [81][82]. Although the Fe-doped titanates exhibit interesting properties as anode for SOFC application only few studies have been carried out on them [82]. The composite $SrTi_{1-x}Fe_xO_3$-GDC, x=4 and 7, shown respectively 191 mW/cm² and 337 mW/cm² at 800 °C under hydrogen, which are interesting results taking in account the low cost of material. Differently from

molybdenum, iron is not active toward hydrocarbon reforming but it is often used in synergy with nickel, enhancing the resistance to carbon poisoning [83][84][85].

The titanates investigated in this study are:

1. $SrTi_{0.9}Mo_{0.1}O_3$,
2. $SrTi_{0.6}Mo_{0.4}O_3$,
3. $Ba_{0.5}Sr_{0.5}Ti_{0.9}Mo_{0.1}O_3$,
4. $Ba_{0.5}Sr_{0.5}Ti_{0.9}Fe_{0.1}O_3$
5. $Ba_{0.5}Sr_{0.5}Ti_{0.6}Fe_{0.4}O_3$

2.5.2 Co-Based perovskite

Cobalt oxides are well known as heterogeneous catalysts for oxidation as well as cathodes for SOFC. $La_{1-x}Sr_xCoO_{3-\delta}$ in fact, was the first perovskite material used as cathode in 1966 by Button and Archer and $LaCoO_3$ was proposed as catalyst for automotive gases abatement by Libby in 1970s [25][86][87]. Although lanthanum and cobalt are both considered critical raw elements, the properties and performance of lanthanum cobaltite suggested to explore the capability of these materials as SOFC electrodes. Cobalt based K_2NiF_4 type structures have been investigated as electrodes for IT-SOFC due to their high mixed-ionic-electronic conductivity and good mechanical and chemical compatibility with SOFC electrolyte [24]. The characteristic structure, in fact, allows to host a great amount of interstitial oxygen ions into the rock-salt layer enhancing the ionic transport [88][89]. Large attention was paid to the La_2NiO_4, La_2CoO_4 and La_2CuO_4 systems which were considered as the most promising material for cathode application [24][90]. The aliovalent doping (with Sr or Ba) in the A-site is the typical strategy carried out to obtain suitable electrical conductivity (10 S cm^{-1} for $La_{0.8}Sr_{1.2}CoO_4$ at room temperature) and to increase the catalytic activity

toward CO and hydrocarbons oxidation on K_2NiF_4 type structures [91][92][93][94]. The best catalytic activity were reported for $(LaSr)_2CoO_4$ showing a T_{50} below 200 °C in CO oxidation [93][95].

2.5.2.1 Ni-doping

Nickelates have received a remarkable attention as electrodes for intermediate temperature SOFC due to the excellent electronic conductivity (La_2NiO_4 100 Scm^{-1}) and higher oxygen mobility when compared with other perovskites [96][97][98][99][100]. It was also found that La_2NiO_4 could reach, after a suitable microstructural optimization, an area specific resistance value of 0.11 Ω cm^2 (at 800 °C) which is extremely good for SOFC application. $La_{1.7}Sr_{0.3}Co_{0.5}Ni_{0.5}O_{4\pm d}$ is reported to achieve an ASR of 1.92 Ω cm^2 under air at 850°C with a symmetric configuration (10Sc1CeSZ 10% Sc_2O_3 and 1% CeO_2 doped ZrO_2 as electrolyte) while $La_{1.2}Sr_{0.8}Co_{0.8}Ni_{0.2}O_{4\pm d}$-GDC composite cathode was able to reach 350 mW/cm^2 at 600 °C in a FC fed with hydrogen.

2.5.2.2 Cu-doping

Cu-doped cobaltites have demonstrated superior catalytic activity toward oxidation and excellent cathodic properties for IT-SOFC. For example $LaCo_{0.5}Cu_{0.5}O_3$ was able of achieve the total CO oxidation below 200 °C while $La_{0.5}Sr_{0.5}Co_{0.5}Cu_{0.5}O_3$ reached an ASR of 0.1 Ω cm^2 under air at 700 °C which is considered an admirable and promising value. With a K_2NiF_4 type structure, cobaltites still show interesting result such as $La_2Co_{0.8}Cu_{0.2}O_4$ which is characterized by an ASR of 0.51 Ω cm^2 at 700 °C in air. Another interesting ASR result was found with $La_{1.7}Sr_{0.3}CuO_4$ which reached 1.2 Ω cm^2 at 500 °C in air. It was also demonstrated that the incorporation of cobalt in La_2CuO_4 structure could increase the electrical and ion conductivity as a function of cobalt loading. [21][22][101][102][103].

The cobaltites investigated in this study are:

1. $(LaSr)_2Co_{0.5}Cu_{0.5}O_4$
2. $(LaSr)_2Co_{0.5}Ni_{0.5}O_4$

2.6 Synthesis procedures

The synthesis procedures have an essential role on the final performance of the materials especially on heterogeneous catalysts. The choice of the synthesis, in fact, is crucial for the chemical-physical and surface properties of the final material. The main syntheses used for the preparation of multi element perovskites can be divided in two types: ceramic and chemical route.

The ceramic route is based on mechanical mixing of solid precursors (oxides, carbonates, acetates of nitrates) followed by thermal treatments at high temperature (1300-1700 °C) in a multi-cycle approach of heating and grindings. This procedure is (or appears) simple but, the high temperature and the mechanical mixing involved frequently induce the formation of large size particles and can lead to chemical and grain size inhomogeneity.

The chemical route or wet chemistry could overcome these disadvantages. There are different chemical routes but co-precipitation, citrate method and Pechini method are the most used. In the last two procedures, the mixing of precursors is performed in solution and the elements homogeneity is obtained at molecular level through the use of an organic complexing molecule. This procedure allows to decrease the temperature of the thermal treatment and also to save time.

In this research all the materials were obtained by means of the citrate method followed by auto combustion of the organic gel and a final thermal treatment a high temperature. The citrate method was selected because is cheap, sustainable and scalable.

2.6.1 Material preparation: citrate method

The titanium based perovskites were obtained through citrate method starting from $SrCO_3$ (Sigma Aldrich ≥98%), $BaCO_3$ (Sigma Aldrich ≥98%), Titanium(IV) isopropoxide (Sigma Aldrich 97%)) and Ammonium molybdate tetrahydrate (Sigma ≥99%). The citric acid was dissolved in water solution (molar ratio of 1.9:1 with respect to the total amount of cations) and subsequently the Ti liquid precursor was added to the solution through a syringe. A HNO_3 concentrated solution was added to the citric acid solution (HNO_3:water = 1:1) kept stirred. After a few seconds, a strong exothermic reaction begun, dissolving the titanium precipitate. The strontium carbonate was dissolved in water after adding a few millilitres of HNO_3 while the Mo precursor was dissolved in the lowest amount of water. The solution obtained by the addition of solutions of precursors was neutralized to pH 7-8 by adding NH_4OH and evaporated on heater to form a gel. The gel achieved was finally burn in a self-combustion ignited by the heater. The powders obtained were grinded and calcined under wet hydrogen at 1200 °C for 6 h in a tube reactor. The thermal treatments used for Ti-based perovskite are reported in table 2.1, table 2.2, table 2.3, table 2.4 and table 2.5 for $SrTi_{0.9}Mo_{0.1}O_3$, $SrTi_{0.6}Mo_{0.4}O_3$, $Ba_{0.5}Sr_{0.5}Ti_{0.9}Mo_{0.1}O_3$, $Sr_{0.5}Ba_{0.5}Ti_{0.9}Fe_{0.1}O_3$ and $Sr_{0.5}Ba_{0.5}Ti_{0.6}Fe_{0.4}O_3$ respectively [104].

The cobalt based perovskites were obtained with the same procedure used for the Ti-based ones but the final thermal treatment was at 900 °C under air. The precursors used were: $SrCO_3$ (Sigma Aldrich ≥98%), La_2O_3 (Aldrich ≥99.9%), Co(III) acetylacetonate (Aldrich 98%), CuO (Aldrich 99.99%) and NiO (Aldrich 99%). The thermal treatments used for Co-based perovskite are reported in table 2.6. The synthesis procedures reported was used and optimized for 5 grams per synthesis and all the powders obtained were grinded manually on agate mortar.

Table 2.1: Thermal treatments and optimization used for $SrTi_{0.9}Mo_{0.1}O_3$ preparation.

Composition	Pre-Treatments	Thermal treatment			Correct Phase
		[°C]	Environment	[h]	
$SrTi_{0.9}Mo_{0.1}O_3$	400 °C, 2 h, Air	1000	Air	6	No
	400 °C, 2 h, Air	850	Air	6	No
	400 °C, 2 h, Air	850	H_2	6	No
	400 °C, 2 h, Air	1000	5% H_2/Ar	6	Yes with Mo impurity
	No	1000	5% H_2/Ar	6	Yes with Mo impurity
	No	1000	20% H_2/Ar	6	Yes with Mo impurity
	No	1000	5% H_2/Ar wet	6	Yes with trace of impurity
	400 °C, 2 h, Air	1000	5% H_2/Ar wet	6	Yes with trace of impurity
	No	1000	5% H_2/Ar wet	12	Yes with trace of impurity
	No	1200	5%H_2/Ar wet	6	Yes

Table 2.2: Thermal treatments and optimization used for $SrTi_{0.6}Mo_{0.4}O_3$ preparation.

Composition	Pre-Treatments	Thermal treatment			Correct Phase
		[°C]	Environment	[h]	
$SrTi_{0.6}Mo_{0.4}O_3$	No	1000	Air	6	No

	No	1000	5% H2/Ar	6	Yes with Mo impurity
	No	1000	5% H2/Ar wet	6	Yes with trace of Mo impurity
	No	1200	5%H2/Ar wet	6	Yes with trace of Mo impurity

Table 2.3: Thermal treatments and optimization used for $Ba_{0.5}Sr_{0.5}Ti_{0.9}Mo_{0.1}O_3$ preparation.

Composition	Pre-Treatments	Thermal treatment			Correct Phase
		[°C]	Environment	[h]	
$Ba_{0.5}Sr_{0.5}Ti_{0.9}Mo_{0.1}O_3$	400 °C, 2 h, Air	1000	Air	6	No
	400 °C, 2 h, Air	1000	5% H_2/Ar	6	No
	400 °C, 2 h, Air	1000	5% H_2/Ar wet	6	No
	No	1000	5% H_2/Ar wet	6	Yes with trace of Mo impurity
	No	850	5% H_2/Ar Ethanol	6	No
	No	1000	5% H_2/Ar Ethanol	6	Yes with impurity
	No	1000	5% H_2/Ar Ethanol/water 50% vol	6	Yes

Table 2.4: Thermal treatments and optimization used for $Ba_{0.5}Sr_{0.5}Ti_{0.9}Fe_{0.1}O_3$ preparation.

Composition	Pre-Treatments	Thermal treatment			Correct Phase
		[°C]	Environment	[h]	
$Sr_{0.5}Ba_{0.5}Ti_{0.9}Fe_{0.1}O_3$	400 °C, 2h, Air	1000	Air	6	Yes
	No	1000	Air	6	Yes

Table 2.5: Thermal treatments and optimization used for $Ba_{0.5}Sr_{0.5}Ti_{0.6}Fe_{0.4}O_3$ preparation.

Composition	Pre-Treatments	Thermal treatment			Correct Phase
		[°C]	Environment	[h]	
$Sr_{0.5}Ba_{0.5}Ti_{0.6}Fe_{0.4}O_3$	400 °C, 2h, Air	1000	Air	6	Yes
	No	1000	Air	6	Yes with trace of impurity
	No	1100	Air	6	Yes

Table 2.6: Thermal treatments used for $(LaSr)_2Co_{0.5}Cu_{0.5}O_4$ and $(LaSr)_2Co_{0.5}Ni_{0.5}O_4$ preparation.

Composition	Pre-Treatments	Thermal treatment			Correct Phase
		[°C]	Environment	[h]	
$(LaSr)_2Co_{0.5}Cu_{0.5}O_4$	No	900	Air	6	Yes

$(LaSr)_2Co_{0.5}Ni_{0.5}O_4$	No	900	Air	6	Yes

2.7 Wet deposition

In order to enhance the catalytic and electrocatalytic activity of Ti-based perovskites, the deposition of nickel precursors was carried out through the wet impregnation method. 0.5 g of the compounds where placed in a becker with 30mL of water. Then the equivalent 30%mol of $Ni(NO_3)_2$ was added to the solution under stirring. The solution was kept under stirring for 24 hours at room temperature and, successively, slowly evaporated at 80°C (still under stirring). The sample prepared where then burned at 450°C in oven in order to decompose the nitrates. The powders prepared were finally treated at 800 °C under 5% H_2/Ar for one hour before the characterization.

Chapter 3

3.1 Introduction to chapter 3

In this chapter titanium based perovskites, doped with barium, molybdenum and iron, were studied as potential anode for Solid Oxide Fuel Cell. The materials developed have been tested also toward sustainable reaction such as carbon monoxide oxidation, methane dry reforming and methane oxidation with the purpose to explore their catalytic behaviour. Finally, on the most promising materials, the electrochemical investigation on symmetric cells was performed at "Institut de Chimie de la Matière Condensée de Bordeaux CNRS" under the supervision of prof. Fabris Mauvy. Five Ti-based perovskites have been considered as anode for solid oxide fuel cell:

1. $SrTi_{0.9}Mo_{0.1}O_3$
2. $SrTi_{0.6}Mo_{0.4}O_3$
3. $Ba_{0.5}Sr_{0.5}Ti_{0.9}Mo_{0.1}O_3$
4. $Ba_{0.5}Sr_{0.5}Ti_{0.9}Fe_{0.1}O_3$
5. $Ba_{0.5}Sr_{0.5}Ti_{0.6}Fe_{0.4}O_3$

3.2 Material preparation

3.2.1. Synthesis

The titanates were prepared through citrate method followed by an auto combustion and thermal treatment. Due to the formation of secondary phases observed after thermal treatment in air, an optimized synthesis step was required, table 3.1. All the materials prepared follow a different thermal treatment so as to obtain the wanted phase. The detailed steps of the synthesis were already described in chapter 2.

Table 3.1: Optimized parameters for the reduction treatment of each prepared compounds

Sample	Label	Conditions
$Ba_{0.5}Sr_{0.5}Ti_{0.9}Mo_{0.1}O_3$,	BST9M1	1000 °C, 6 h, 5%H_2/Ar+EtOH
$SrTi_{0.9}Mo_{0.1}O_3$,	ST9M1	1200 °C 6 h, 5%H_2/Ar+Water
$SrTi_{0.6}Mo_{0.4}O_3$,	ST6M1	1200 °C 6 h, 5%H_2/Ar+Water
$Ba_{0.5}Sr_{0.5}Ti_{0.9}Fe_{0.1}O_3$	BST9F1	1000 °C, 6 h, Air
$Ba_{0.5}Sr_{0.5}Ti_{0.6}Fe_{0.4}O_3$	BST6F4	1000 °C, 6 h, Air

All the thermal treatments were performed in a tubular furnace with a heating rate of 6°C/min.

3.3 Characterization

3.3.1 Structure investigation (XRD)

All the material prepared show a high degree of crystallinity and no significant undesired phases were detected. This is probably due to the high temperature

involved during the synthesis. The phase formation was confirmed by the comparison of XRD patterns with JCPDS database.

3.3.1.1 Mo-doped Titanates

Figure 3.1, displays the diffraction patterns of $SrTi_{0.9}Mo_{0.1}O_3$ sample. The thermal treatment under air shows the presence of two phases, the $SrTiO_3$ and the secondary phase $SrMoO_4$ which is an undesired insulator material that segregates during the synthesis at low temperature [105][106][107]. In order to avoid the formation of $SrMoO_4$, the thermal treatment was performed under reducing environment. Different procedures were used changing temperature and O_2 partial pressure (chapter 2). The optimized conditions were reported in table 3.1. Taking in consideration the reference pattern $SrTiO_3$ a small shift to lower angle can be observed in the Mo-doped $SrTiO_3$ confirming the Ti substitution.

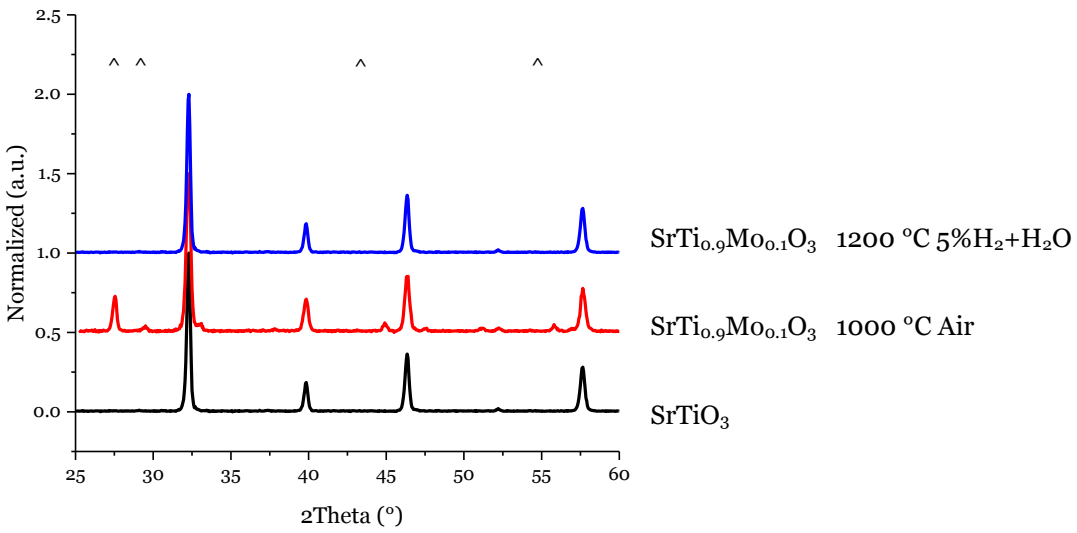

Figure 3.1: XRD patterns of $SrTi_{0.9}Mo_{0.1}O_3$ with different treatments.

(^) $SrMoO_4$ (tetragonal) 01-085-0586 JCPDS database

$SrTiO_3$ (cubic) 00-040-1500 JCPDS database

In figure 3.2 can be observed the XRD patterns of $SrTi_{0.6}Mo_{0.4}O_3$. As already seen in the sample $SrTi_{0.9}Mo_{0.1}O_3$, the thermal treatment under air induced the formation of clearly visible $SrMoO_4$. The XRD pattern of $SrTi_{0.6}Mo_{0.4}O_3$ revealed also a small segregation of Mo(0) at 40.5° indicating that the severe reducing treatment, essential for the phase formation, induced the molybdenum segregation. The molybdenum outside the perovskite structure was then reduced.

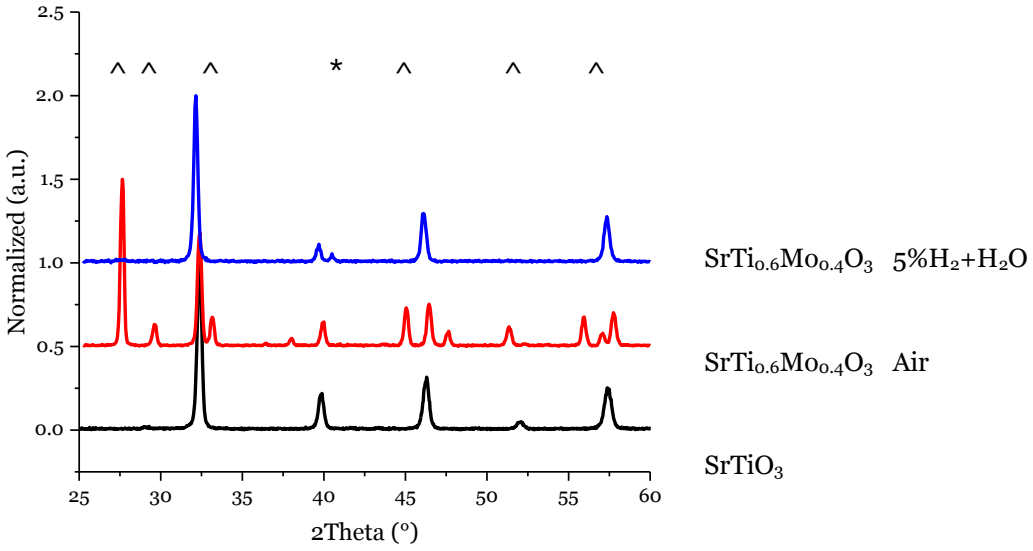

Figure 3.2: XRD patterns of $SrTi_{0.6}Mo_{0.4}O_3$ with different treatments.

(^) $SrMoO_4$ (tetragonal) 01-085-0586 JCPDS database

(*) Mo(0) (cubic) 00-042-1120 JCPDS database

$SrTiO_3$ (cubic) 00-040-1500 JCPDS database

Figure 3.3 shows the patterns after the thermal treatment carried out on $Ba_{0.5}Sr_{0.5}Ti_{0.9}Mo_{0.1}O_3$. The Sr substitution with Ba in $SrTi_{0.9}Mo_{0.1}O_3$ required peculiar pO_2 conditions in order to be carried out. Treatment in air induces the oxidation of Mo(IV) to Mo(VI) with a segregation of a secondary phase ($BaMoO_4$ / BaO, MoO_3), while a reductive treatment in 5%H_2 dry and wet condition induce the formation of Mo(0) and $BaMoO_4$/BaO, MoO_3, respectively. The optimized

conditions to obtain the material were achieved by flowing 5% H_2/Ar in a mixture of 50% Ethanol in H_2O [104].

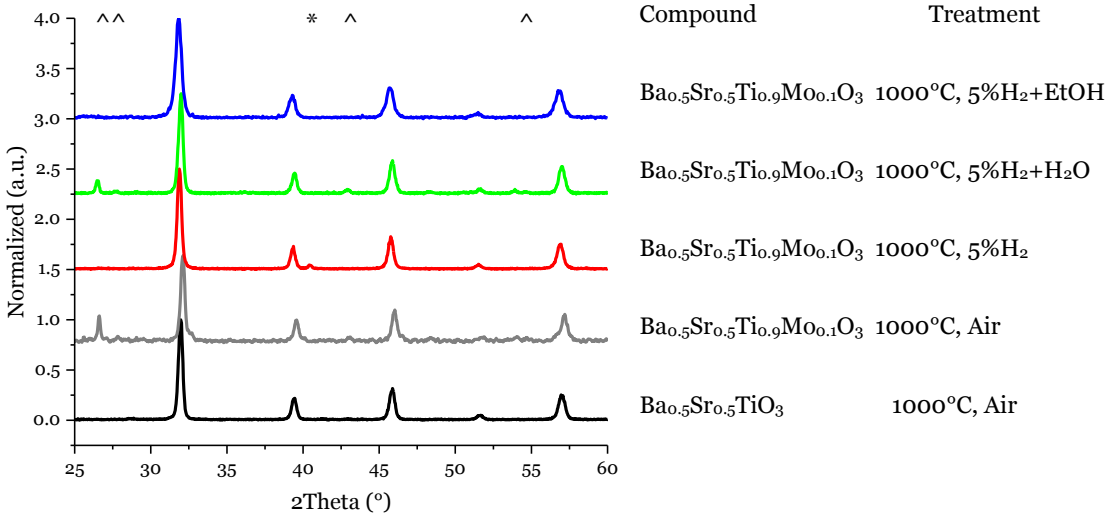

Figure 3.3: XRD patterns of $Ba_{0.5}Sr_{0.5}Ti_{.9}Mo_{0.1}O_3$ with different treatments.

(^) $BaMoO_4$ / BaO, MoO_3 (tetragonal) 00-029-0193 JCPDS database;

(*) Mo(0) (cubic) 00-042-1120 JCPDS database;

$Ba_{0.5}Sr_{0.5}TiO_3$ (cubic) 00-039-0039 JCPDS database.

The successful syntheses of Mo-doped titanates were strongly pO_2 dependent. Oxidising atmospheres promote the higher oxidation state of Mo and so the segregation of undesired $SrMoO_4$ and $BaMoO_4$ insulating phases. On other hand a strong reducing environments induce the reduction to Mo metal avoiding the Ti substitution in the structure.

3.3.1.2 Fe-doped Titanates

Unlike Mo-doped materials, Fe-doped titanates were all prepared at 1000 °C in air. As can be seen from the patterns in figure 3.4, trace of a secondary phase

($BaFe_2O_4$) was observed in the compounds with high Fe concentration. Low concentration of Fe dopant does not induce the formation of secondary phases.

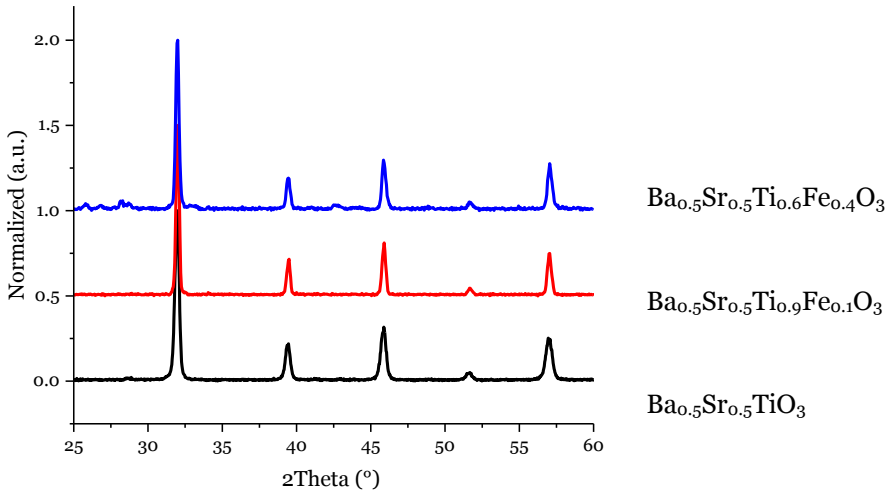

Figure 3.4: XRD patterns of $Ba_{0.5}Sr_{0.5}Ti_{1-x}Fe_xO_3$ series with different treatments.

(^) $BaFe_2O_4$ (Orthorhombic) 00-046-0113 JCPDS database;

$Ba_{0.5}Sr_{0.5}TiO_3$ (cubic) 00-039-0039 JCPDS database.

3.4 Redox behaviour

3.4.1 Temperature programmed reduction

The temperature programmed reduction (TPR) was utilized to determine the reducibility of cations and their stability under reducing condition. According to literature,[108] titanium base perovskite did not show any reduction peak, figure 3.5, in the temperature range explored and shown stability under 5%H_2 up to 900°C. This confirms that Mo(IV) is stabilized by perovskite structure.

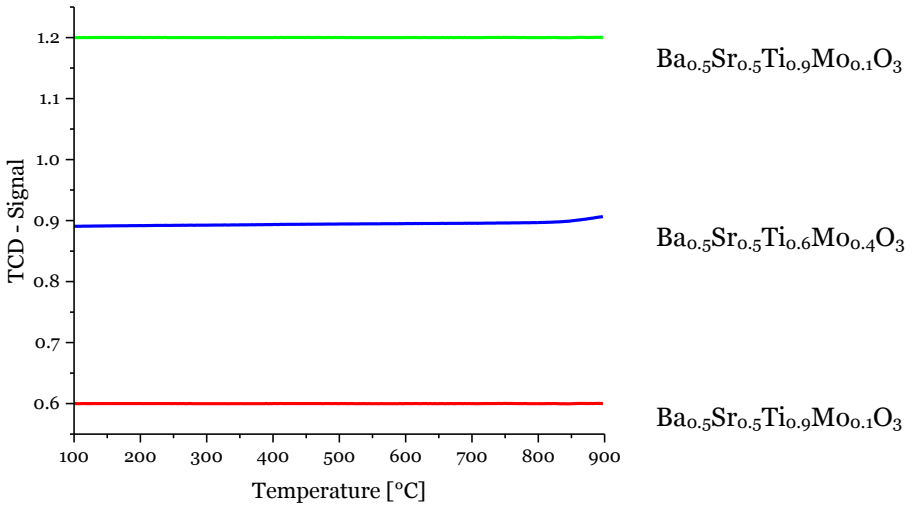

Figure 3.5: Temperature programmed reduction on $Ba_{1-y}Sr_yTi_{1-x}Mo_xO_3$. 5%$H_2$/Ar from RT to 900 °C.

Fe-doped titanates, instead, show signals related to Fe reduction, figure 3.6. The sample $Ba_{0.5}Sr_{0.5}Ti_{0.9}Fe_{0.1}O_3$ shows one peak at 605 °C with a shoulder at 653 °C which are attributable, following literature, at the reduction of Fe(III) to Fe(II) and Fe(II) to Fe(0). The Fe doping increase, $Ba_{0.5}Sr_{0.5}Ti_{0.6}Fe_{0.4}O_3$, induces the formation of Fe(IV) (reduction Fe(IV)/Fe(III) at 444 °C). The main reduction peak is observed at 670 °C with a shoulder at 730 °C. As reported in literature, they were attributed to the reduction Fe(III)/Fe(II) and Fe(II)/Fe(0), respectively [109][110]. The presence of Fe(0) is confirmed also by XRD carried out in the sample after TPR (figure 3.7). In both samples the total iron reduction was not reached. The H_2 consumption revealed the higher stability of Fe(III) in $Ba_{0.5}Sr_{0.5}Ti_{0.9}Fe_{0.1}O_3$, with only 28% of H_2 consumption, respect the total theoretical reduction, than $Ba_{0.5}Sr_{0.5}Ti_{0.6}Fe_{0.4}O_3$ with 67% of H_2 consumption, table 3.2.

Table 3.2: $\%H_2$ consumption data obtained by TPR analysis on Fe-doped samples.

Sample	Experiment/theoretical H_2 consumption %
$Ba_{0.5}Sr_{0.5}Ti_{0.9}Fe_{0.1}O_3$	28%
$Ba_{0.5}Sr_{0.5}Ti_{0.6}Fe_{0.4}O_3$	67%

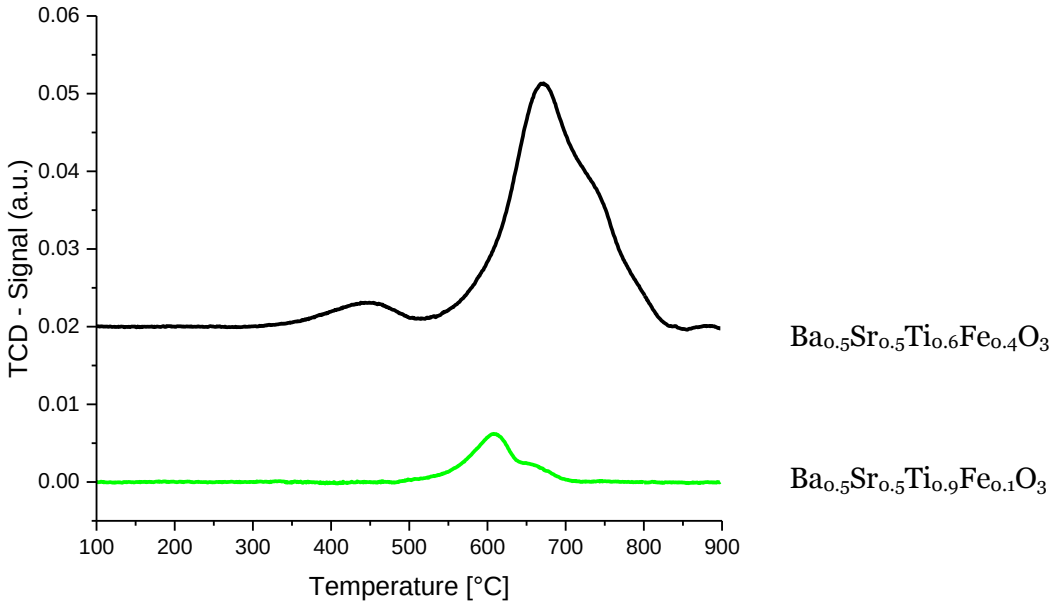

Figure 3.6**:** Temperature programmed reduction on $Ba_{0.5}Sr_{0.5}Ti_{1-x}Fe_xO_3$.

In order to study the stability of the materials, XRD analyses were performed after TPR. As expected after TPR, Mo-doped titanates did not shown any structural change while $Sr_{0.5}Ba_{0.5}Ti_{1-x}Fe_xO_3$ samples displayed, figure 3.7, a slight segregation of Fe(0).

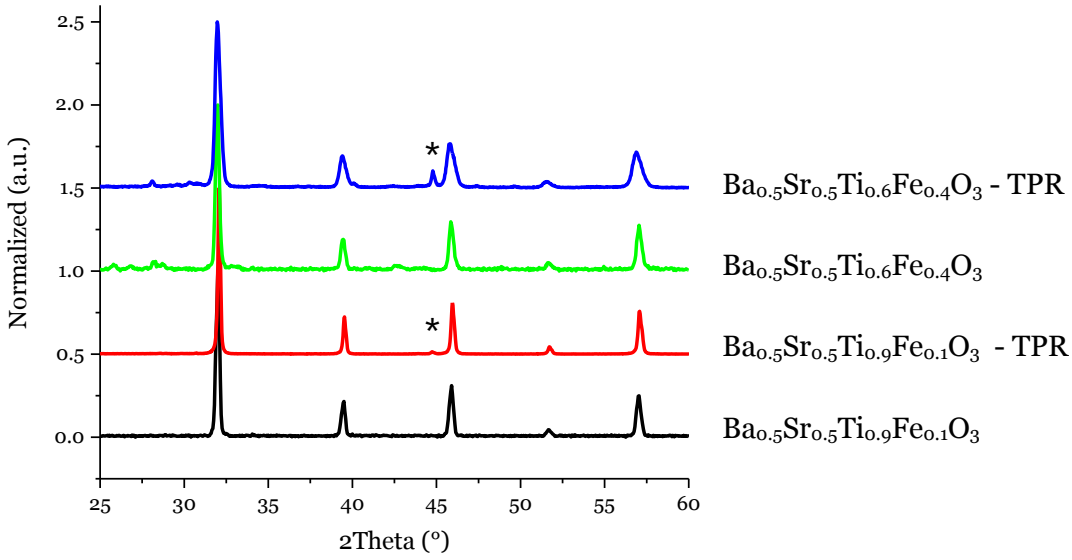

Figure 3.7: XRD patterns of $Ba_{0.5}Sr_{0.5}Ti_{1-x}Fe_xO_3$ before and after TPR.

(*) Fe(0).

XRD performed after TPR suggest a very good stability of Mo-doped materials and $Ba_{0.5}Sr_{0.5}Ti_{0.9}Fe_{0.1}O_3$ under reducing conditions.

3.4.2 Temperature programmed oxidation

The temperature programmed oxidation (TPO) was carried out with the purpose to investigate the stability of Mo-doped titanates under oxidising condition, figure 3.8.

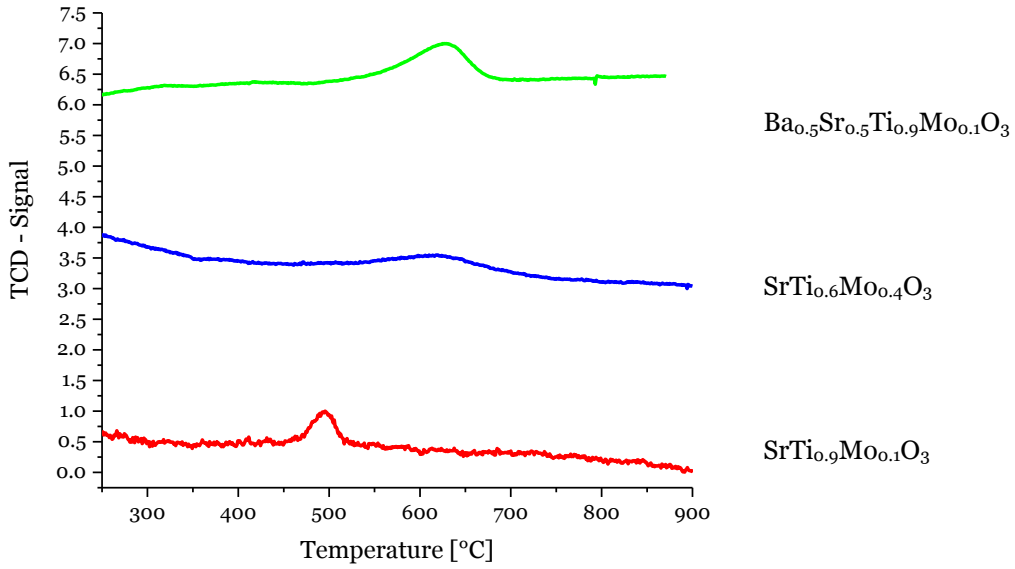

Figure 3.8: Temperature programmed oxidation on $Ba_{1-y}Sr_yTi_{1-x}Mo_xO_3$. The signals were normalized to a better comparison.

The TPO in figure 3.8 shown that Mo-doped were susceptible to oxidising atmosphere. In $SrTi_{0.9}Mo_{0.1}O_3$ can be seen a narrow peak centred at 497 °C. The peak was attributed to the one step oxidation of Mo(IV) to Mo(VI) and the consequent formation of $SrMoO_4$. This was also confirmed by the XRD pattern, figure 3.9, carried out after TPO. The redox behaviour is in agreement with literature in which thermo gravimetric analysis shown the oxidation of Mo(IV) to Mo(VI) between 500 °C and 700 °C [111][112][113]. The same redox behaviour was observed in $SrTi_{0.6}Mo_{0.4}O_3$ and $Ba_{0.5}Sr_{0.5}Ti_{0.9}Mo_{0.1}O_3$ displaying two wide peaks at 621 °c and 629 °C, respectively. The higher temperature required for Mo(IV) oxidation suggested a higher cation stability. The larger peaks shape could be explained by the presence of Mo metal on $SrTi_{0.6}Mo_{0.4}O_3$, visible in figure 3.2 at 40.5°, and by the presence of MoO_2 observed with XPS analysis. The $\%O_2$ consumption data, table 3.3, revealed only partial oxidation of Mo(IV) to Mo(VI) suggesting the Mo(IV) stability in $SrTiO_3$ structure. The compound

$Ba_{0.5}Sr_{0.5}Ti_{0.9}Mo_{0.1}O_3$ has shown the lower O_2 consumption, 27.9%, which was significantly smaller than the compounds without Ba doping that shown 45.3% and 60.9% for $SrTi_{0.9}Mo_{0.1}O_3$ and $SrTi_{0.6}Mo_{0.4}O_3$ 45.3%, respectively. This result seemed point out a greater stability for barium doped compound when compared with no barium doped ones. The large O_2 consumption detected for $SrTi_{0.6}Mo_{0.4}O_3$ was justified by the oxidation of Mo metal to MoO_3 has shown in figure 3.9.

Table 3.3: $\%O_2$ consumption data obtained by TPO analysis on Mo-doped samples, considering the oxidation of MoO_2 to MoO_3.

Sample	**Experiment/theoretical O_2 consumption %**
$SrTi_{0.9}Mo_{0.1}O_3$	45.3
$SrTi_{0.6}Mo_{0.4}O_3$	60.9
$Ba_{0.5}Sr_{0.5}Ti_{0.9}Mo_{0.1}O_3$	27.9

In order to study the stability of the materials, XRD analyses were performed after TPO.

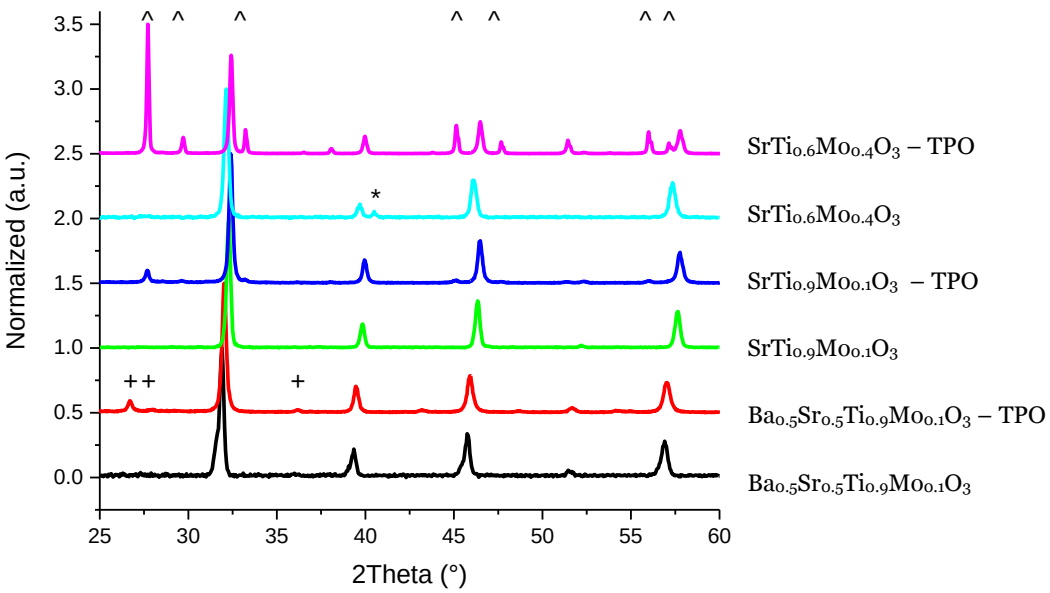

Figure 3.9**:** XRD patterns of $Ba_ySr_{1-y}Ti_1Mo_xO_3$ before and after TPO.

(*) Mo(0) (cubic) 00-042-1120 JCPDS database;

(^) $SrMoO_4$ (tetragonal) 01-085-0586 JCPDS database

(+) $BaMoO_4$ / BaO, MoO_3 (tetragonal) 00-029-0193 JCPDS database.

The XRD patterns after TPO, figure 3.9, have shown the presence of secondary phases in all the samples. They were attributed to the segregation of Mo(VI), $BaMoO_4$ and $SrMoO_4$, after its oxidation. The observed impurities are well known electrical insulators but the reductive environment to which the anodes are undergone under working conditions will avoid the oxidation of Mo(IV) [105][106][107]. Focusing on table 3.1 and figure 3.9 it could be noted that $SrTi_{0.6}Mo_{0.4}O_3$ underwent a larger segregation while $SrTi_{0.9}Mo_{0.1}O_3$ and $Ba_{0.5}Sr_{0.5}Ti_{0.9}Mo_{0.1}O_3$ shown only trace of $SrMoO_4$ and $BaMoO_4$, respectively. With the purpose of verifying the re-reduction of samples, TPR after TPO were performed and the phases were checked by XRD. Only the compound $SrTi_{0.9}Mo_{0.1}O_3$ has shown a complete structure restoration while $SrTi_{0.6}Mo_{0.4}O_3$

and $Ba_{0.5}Sr_{0.5}Ti_{0.9}Mo_{0.1}O_3$ still kept trace of secondary phases. The temperature programmed oxidation carried out on Fe-doped compounds did not show any alteration after TPO.

Fe-doped materials were easily obtained by calcination in air, whereas Mo-doped material required specific thermal treatment in order to find the proper O_2 partial pressure condition. The data collected have given important advice regarding the possible synthesis of Mo-doped titanates and the stability of the different titanates under oxidizing and reducing conditions.

3.5 Powder morphology

The powders prepared by means of the citrated method, see details chapter 2, were investigate through Scanning Electron Microscopy (SEM), to study the particles morphology, BET analysis, to detect the surface area, and laser diffusion, to observed the particle size distribution (Matersizer 2000).

The SEM images of Mo-doped samples are reported in figure 3.10. All the samples revealed particle homogeneity with an aggregate morphology. This aggregate morphology, composed by particles with a diameter of 100-200nm, was induced probably by the high temperatures involved during the synthesis. It is interesting to notice that $Ba_{0.5}Sr_{0.5}Ti_{0.9}Mo_{0.1}O_3$ shown a slightly bigger particles diameter (200nm) than the others compounds although it was prepared at lower temperatures, chapter 2. The different synthesis temperatures, chapter 2, did not affect the specific surface area which resulted between 4 and 5 m^2/g, table 3.4.

The particle size distributions displayed the presence of two main diameters for $SrTi_{0.9}Mo_{0.1}O_3$ $SrTi_{0.6}Mo_{0.4}O_3$, figure 3.11 and figure 3.12. The most abundant at around 4μm and the second one at 0.5μm. Although both sample analysed have a similar trend in the particle distributing, $SrTi_{0.6}Mo_{0.4}O_3$ shown larger difference

between small and big diameters than the $SrTi_{0.9}Mo_{0.1}O_3$. This could be explained by the higher temperature needed for the sinterization of titanium based compounds; in fact both the samples were prepared at the same temperature (1200 °C) but with a remarkable difference in Ti amount. The common parameter the describe the particle size distribution is d(0.5). It is the diameter where the 50% of the particles are smaller than that value. The d(0.5), that is common parameter the diameter of $SrTi_{0.9}Mo_{0.1}O_3$ and $SrTi_{0.6}Mo_{0.4}O_3$ were 4.014 μm and 4.200 μm respectively.

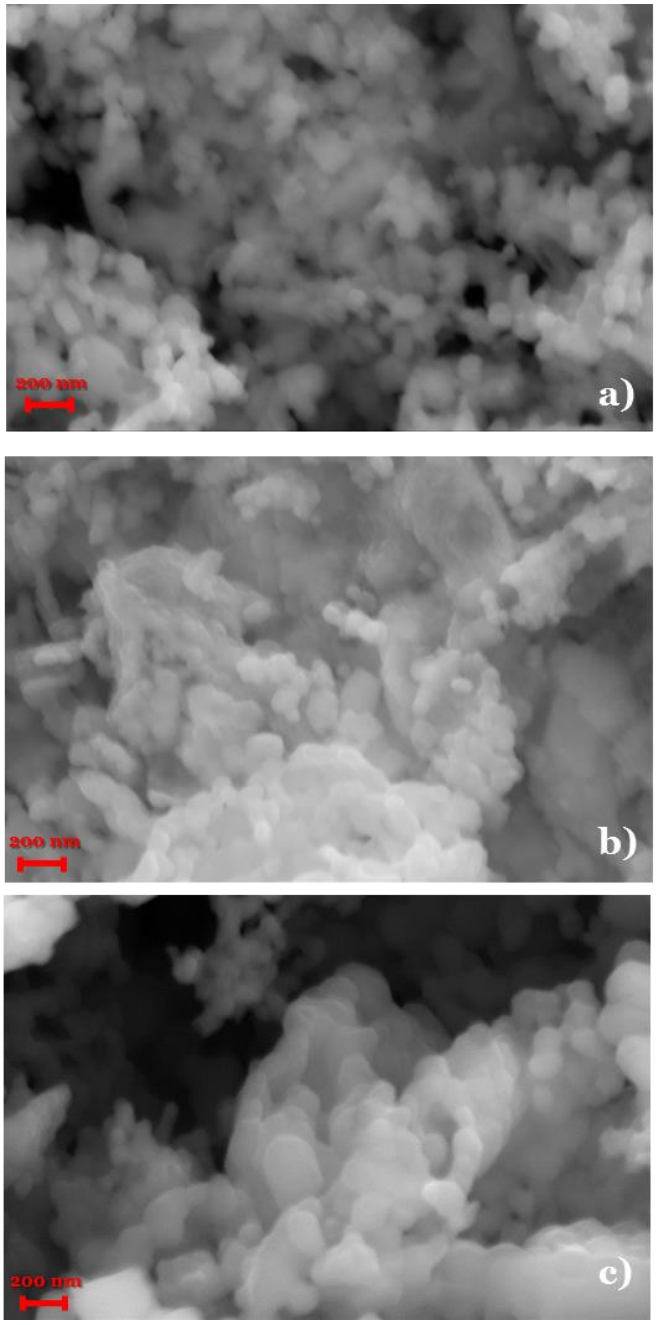

Figure 3.10: SEM images for a) $SrTi_{0.9}Mo_{0.1}O_3$, $SrTi_{0.4}Mo_{0.6}O_3$ b) and $Ba_{0.5}Sr_{0.5}Ti_{0.9}Mo_{0.1}O_3$ c).

Table 3.4: Surface area of $SrTi_{0.9}Mo_{0.1}O_3$, $SrTi_{0.4}Mo_{0.6}O_3$ and $Ba_{0.5}Sr_{0.5}Ti_{0.9}Mo_{0.1}O_3$.

Sample	Surface area [m²/g]
$SrTi_{0.9}Mo_{0.1}O_3$	5
$SrTi_{0.4}Mo_{0.6}O_3$	4
$Ba_{0.5}Sr_{0.5}Ti_{0.9}Mo_{0.1}O_3$	4

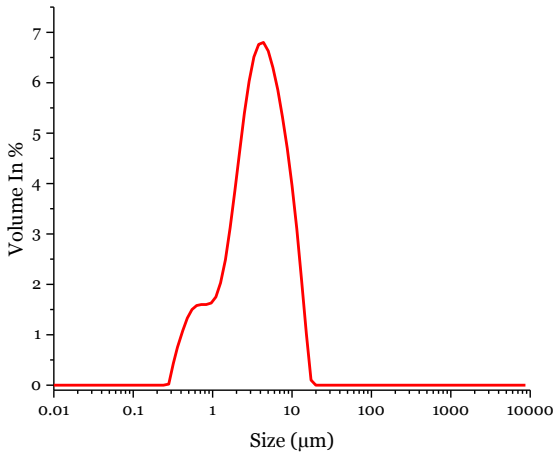

Figure 3.11: Particle size distribution of $SrTi_{0.9}Mo_{0.1}O_3$.

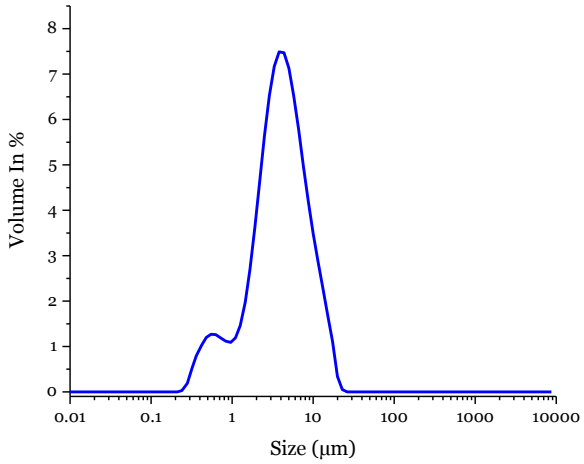

Figure 3.12: Particle size distribution of $SrTi_{0.4}Mo_{0.6}O_3$

3.6 Surface characterization

3.6.1 X-ray photoelectron spectroscopy

The surface investigation was performed by means X-ray photoelectron spectroscopy (XPS) on Mo-doped titanates. The XPS spectra and peak positions are displayed in figure 3.13 and in table 3.5, respectively. The Sr 3d signal shown two peaks centred at 134.7-134.8 eV and 132.2-132.5 eV. The Sr 3d peaks fitting suggests the ovelapping of two doublets attribuited, in according with literature,

to perovskite phase (133.8-132.2 eV) and a surface segregation of SrO and $Sr(OH)_2$ (134.9 eV and 132.2) [114][115][116]. The asymmetric Ba $3d_{5/2}$ XPS signal is centred at 779.4 eV which is characteristic BE for Ba in $BaTiO_3$. The shoulder observed at high BE is due to the contribution of $BaCO_3$ which is typically centred at 779.1 eV and to $Ba(OH)_2$ that is reported to have a binding energy of 779.3 eV [117][118]. The Ti $2p_{3/2}$ XPS peak position 458.6-458.4 eV (figure 3.13) agrees with how expected for titanium in $SrTiO_3$ and $BaTiO_3$ [114]. The Ti 2p signal on sample $Ba_{0.5}Sr_{0.5}Ti_{0.9}Mo_{0.1}O_3$ shows a contribution at 460.5 eV attribuited to Ti^{3+} probably induced by the reduction theatment that the sample underwent [119]. The signal Mo 3d centred at 235.5-235.6 eV and 232.5 eV releved the presence of MoO_3 on the surface but the fitting of the XPS signal suggested the also a small contribution of MoO_2 [120][121][122]. Although the XRD pattern of $SrTi_{0.6}Mo_{0.4}O_3$ shown a small Mo metal phase, figure 3.2, the absence of Mo(0) XPS signal revealed the tendecy of molybdenum to reach the higher and more stable oxidation state. Focussing on the O 1s XPS peak, spectra reveal two contributions: one (529.6 eV) is due to lattice oxygen whereas the other one (about 531.8 eV) suggests the presence of hydroxide species, such as $Ba(OH)_2$ that can be found at 531.2 eV, and non-perovskitic oxides (MoO_3 and TiO_2) [123] [124][125].

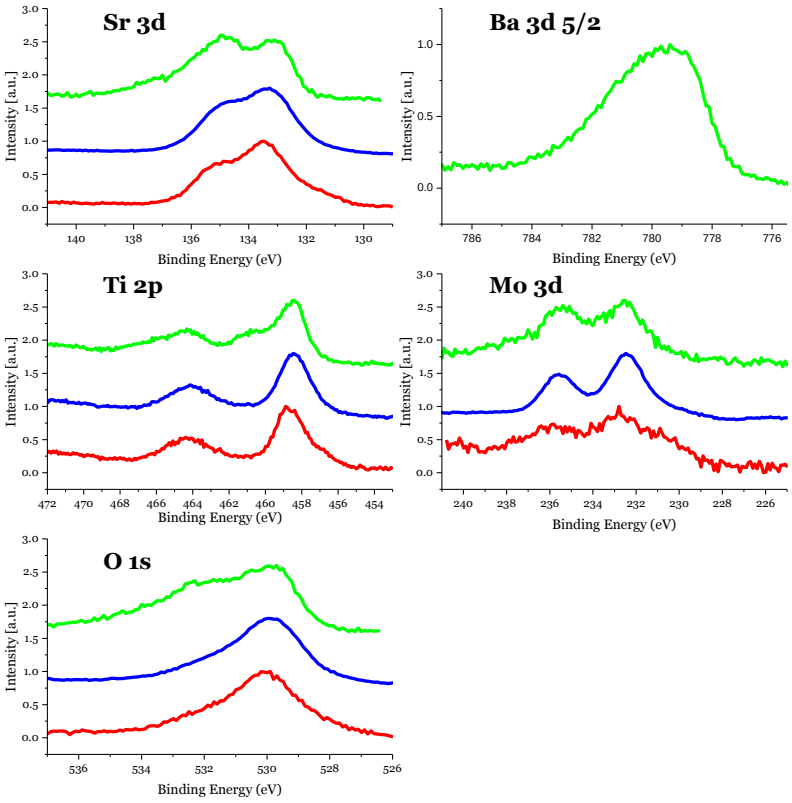

Figure 3.13: XPS spectra obtained for $SrTi_{0.9}Mo_{0.1}O_3$ (Red), $SrTi_{0.4}Mo_{0.6}O_3$ (Blue) and $Ba_{0.5}Sr_{0.5}Ti_{0.9}Mo_{0.1}O_3$ (Green).

Table 3.5: XPS peak positions in Binding Energy [eV] for $SrTi_{0.9}Mo_{0.1}O_3$, $SrTi_{0.4}Mo_{0.6}O_3$ and $Ba_{0.5}Sr_{0.5}Ti_{0.9}Mo_{0.1}O_3$.

	Ba 3d 5/3	**Sr 3d**	**Ti 2p 3/2**	**Mo 3d**	**O 1s**
$Ba_{0.5}Sr_{0.5}Ti_{0.9}Mo_{0.1}O_3$	779.4	134.8 /133.2	458.4	235.5 / 232.5	531.8 / 529.9
$SrTi_{0.4}Mo_{0.6}O_3$	-	134.7/133.2	458.4	235.6 / 232.5	529.9
$SrTi_{0.9}Mo_{0.1}O_3$	-	134.7 / 133.3	458.6	235.6 / 232.5	539.9

The XPS quantitative analysis of Mo-doped titanates is reported in table 3.6. For a comparison the samples $SrTiO_3$ and $Sr_{0.5}Ba_{0.5}TiO_3$ were prepared trough citrated synthesis and treated under reductive atmosphere and finally characterized by XPS. All the samples analysed had oxygen over stoichiometry on surface confirming the presence of carbonates and hydroxides. Barium doping did not induce any change in oxygen surface concentration and it was always under the nominal values. The presence of large ion Ba^{2+} in $Ba_{0.5}Sr_{0.5}Ti_{0.9}Mo_{0.1}O_3$ seems to keep the cation concentration close to the nominal value probably due to lesser constrain in the crystal structure [126]. Strontium instead was always over the nominal values with the exception of $SrTiO_3$ in which it was below the nominal value and in $Ba_{0.5}Sr_{0.5}Ti_{0.9}Mo_{0.1}O_3$ that had the nominal one. Taking in account the ratio Mo/Ti could be noted that for small Mo doping the values were closed to the theoretical one with 0.09 and 0.06 for $Ba_{0.5}Sr_{0.5}Ti_{0.9}Mo_{0.1}O_3$ and $SrTi_{0.9}Mo_{0.1}O_3$, respectively. When large amount of Mo is introduced a significant segregation of Mo was detected. This segregation is highlighted also by the decreasing of Ti surface concentration in $SrTi_{0.4}Mo_{0.6}O_3$. Mo doping seemed also to reduce the oxygen segregation moving the value closer to the theoretical one.

Table 3.6: XPS atomic composition for the Mo doped titanates, $Sr_{0.5}Ba_{0.5}TiO_3$ and $SrTiO_3$.

Sample		Ba	Sr	Ti	Mo	O	Mo/Ti	Sr/Ti
$Ba_{0.5}Sr_{0.5}Ti_{0.9}Mo_{0.1}O_3$	Experimental	6	7	14	1	72		
		21	25	49	4	-	0.1	0.5
	Nominal	10	10	18	2	60		
		25	25	45	5	-	0.1	0.6
$SrTi_{0.9}Mo_{0.1}O_3$	Experimental	-	18	12	1	69		
		-	58	40	2	-	0.1	1.5
	Nominal	-	20	18	2	60		
		-	50	45	5	-	0.1	1.1
$SrTi_{0.4}Mo_{0.6}O_3$	Experimental	-	17	8	8	67		
		-	52	24	24	-	1.0	2.1
	Nominal	-	20	12	8	60		
		-	50	30	20	-	0.7	1.7
$Sr_{0.5}Ba_{0.5}TiO_3$	Experimental	6	8	14	-	72		
		20	29	51	-	-		
	Nominal	10	10	20	-	60		
		25	25	50	-	-		
$SrTiO_3$	Experimental	-	12	16	-	72		
		-	42	57	-	-		
	Nominal	-	20	20	-	60		
		-	50	50	-	-		

3.7 Catalytic behaviour

The catalytic reactivity towards sustainable reactions was tested in an appropriately designed reactor and the products were detected by means gas-chromatography equipped with TCD. The reactions investigated were the oxidation of carbon monoxide and methane dry-reforming. The GHSV used for tests was nearby 100,000 h^{-1}.

3.7.1 Reactivity with CO + O2

The catalytic behaviour of CO oxidation with stoichiometric amount of O_2 is reported in figure 3.14.

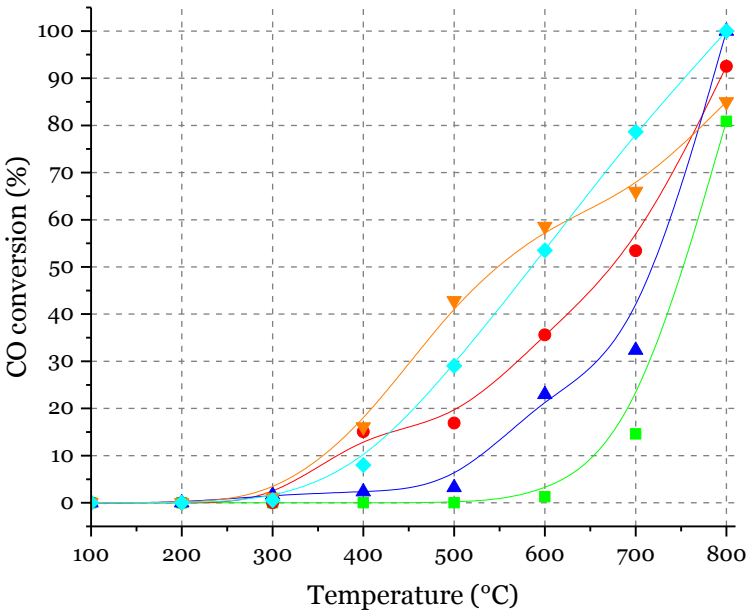

Figure 3.14: CO conversion as a function of temperature for $SrTi_{0.9}Mo_{0.1}O_3$ (Red), $SrTi_{0.4}Mo_{0.6}O_3$ (Blue), $Ba_{0.5}Sr_{0.5}Ti_{0.9}Mo_{0.1}O_3$ (Green), $Ba_{0.5}Sr_{0.5}Ti_{0.9}Fe_{0.1}O_3$ (Orange) and $Ba_{0.5}Sr_{0.5}Ti_{0.6}Fe_{.4}O_3$ (light blue).

It is well know that many perovskite are active towards the CO oxidation and as expected all the compounds prepared reach almost total CO conversion under intermediate temperature SOFC working conditions (600-800 °C) [127]. The total CO conversion is reached only by $SrTi_{0.4}Mo_{0.6}O_3$ and $Ba_{0.5}Sr_{0.5}Ti_{0.6}Fe_{.4}O_3$ at 800 °C while $SrTi_{0.9}Mo_{0.1}O_3$ at the same temperature achieved 93%. $Ba_{0.5}Sr_{0.5}Ti_{0.9}Fe_{0.1}O_3$ and $Ba_{0.5}Sr_{0.5}Ti_{0.9}Mo_{0.1}O_3$ have shown the lower CO conversion obtaining 85% and 80% respectively. Beyond the total conversion it was interesting to notice the different ignition points and the activity as a function of temperature. $Ba_{0.5}Sr_{0.5}Ti_{0.9}Fe_{0.1}O_3$ had a linear CO conversion up to

800 °C but $Ba_{0.5}Sr_{0.5}Ti_{0.6}Fe_{.4}O_3$ had a remarkable drop in activity between 600 °C and 700 °C. This drop occurred exactly in the temperature range where the Fe^{3+} was reduced to Fe^{o} in the TPR analysis, figure 3.6. Although the reactivity condition was slightly different the loss of iron from the perovskite structure, shown in the XRD pattern figure 3.7, could have led to a loss of oxygen mobility and then activity. Fe-doped compounds and $SrTi_{0.9}Mo_{0.1}O_3$ had the lower activation temperatures, below 300 °C, but while the Fe-doped titanates increase rapidly their CO conversion, $SrTi_{0.9}Mo_{0.1}O_3$ goes through a small plateau between 400 °C and 500 °C before to reach the maximum activity. The same catalytic behaviour of $SrTi_{0.9}Mo_{0.1}O_3$ was observed also on $SrTi_{0.4}Mo_{0.6}O_3$ but both the ignition point and the plateau were shifted at higher temperature, around 400 °C and between 600 °C and 700 °C, respectively. Above the plateau the activities rise up faster than Fe-doped compounds. The plateau suggested an activation process which is essential in order to achieve the best performance. Taking in account the TPO analysis, figure 3.8, it could be observed the strict relation between the re-oxidation of the structure and the CO oxidation plateau for both $SrTi_{0.9}Mo_{0.1}O_3$ and $SrTi_{0.4}Mo_{0.6}O_3$. This gave important information regarding the essential role of oxygen in these processes. In fact, the severe reducing conditions, necessary for the material preparation, were probably the cause of oxygen depletion of the material and so of the shift at higher temperatures of the ignition point. When the high temperatures allowed the oxygen restoration into the structure and therefore the oxygen ion mobility, the activity received a boost. This catalytic behaviour is in according with the Mars Van Krevelen mechanism expected for perovskite oxide [61][128][129]. The compound with the higher amount of Mo had shown the larger oxygen consumption, table 3.3, but also the greater improvement in performance, pointing out the role of molybdenum in oxygen mobility and catalytic activity. The lower performance was observed on $Ba_{0.5}Sr_{0.5}Ti_{0.9}Mo_{0.1}O_3$

with an ignition temperature of 500 °C but with the absence of an activation step. This is in agreement with the XPS quantitative analysis, table 3.6, showing the superior amount of oxygen on $Ba_{0.5}Sr_{0.5}Ti_{0.9}Mo_{0.1}O_3$ surface than the other samples. The lower reactivity towards CO oxidation could be justified by the minor oxygen consumption, table 3.6, and so probably the lower oxygen mobility of $Ba_{0.5}Sr_{0.5}Ti_{0.9}Mo_{0.1}O_3$.

3.7.2 Reactivity toward methane: Dry reforming

Methane dry reforming (MDR) is an endothermic reaction of high scientific and industrial importance that requires very high temperature [130]. The implementation of MDR directly in cell could considerably increase the total efficiency of SOFC, e.g. due to the heat transfer, and drops the complexity of final device. All the materials prepared were tested towards MDR with a GHSV of about 75,000 h^{-1}. The space velocity was decreased with the purpose to enhance the contact time of the species on the surface and so increase the performance [131].

Among all the samples, only $SrTi_{0.9}Mo_{0.1}O_3$ show an activity at 800 °C, reaching about 58% of CH_4 and 53% of CO_2 conversion, figure 3.15. The activity started at around 625 °C with a conversion linear as a function of temperature. The catalyst was kept at 800°C under working condition for 6 hours without showing any change on catalytic behaviour. Although the activity and the long run test were modest compare with those of state of art, the absence Ni metal or noble metal could encourage further study on this system [130][132][133].

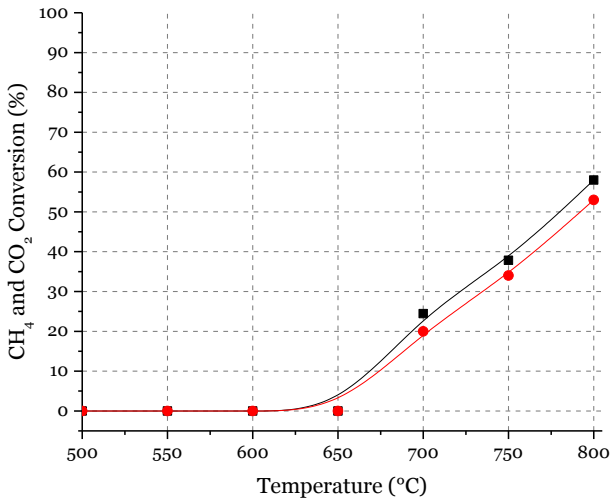

Figure 3.15: 2 %CH_4 + 2 %CO_2. % Conversion in CH_4+CO_2 (stoichiometric) from 500 °C to 800 °C. CH_4 (black) and CO_2 (Red).

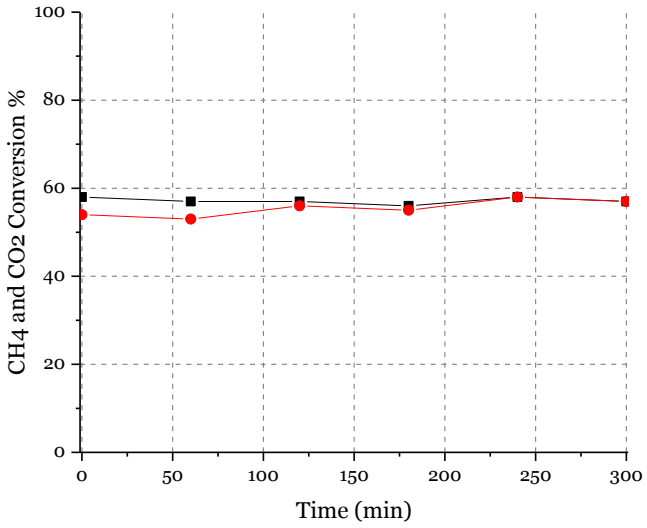

Figure 3.16: 2 %CH_4 + 2 %CO_2. % Conversion in CH_4+CO_2 (stoichiometric) at 800 °C for kept for 300 minutes. CH_4 (black) and CO_2 (Red).

3.7.3 Reactivity toward methane: direct oxidation of methane

The reactivity toward the methane oxidation was explored, figure 3.17, for the compounds $SrTi_{0.9}Mo_{0.1}O_3$ and $SrTi_{0.6}Mo_{0.4}O_3$. Although the materials showed a small activity below 800 °C the auto ignition temperature of methane, 537 °C, has to take in account [134]. The methane conversion, in fact, is probably induced by the spontaneously ignition thermally activated. The CH_4 convention reached were 46% and 47% respectively for $SrTi_{0.9}Mo_{0.1}O_3$ and $SrTi_{0.6}Mo_{0.4}O_3$ at 850 °C. Below 800 °C the methane conversion was hardly 10%.

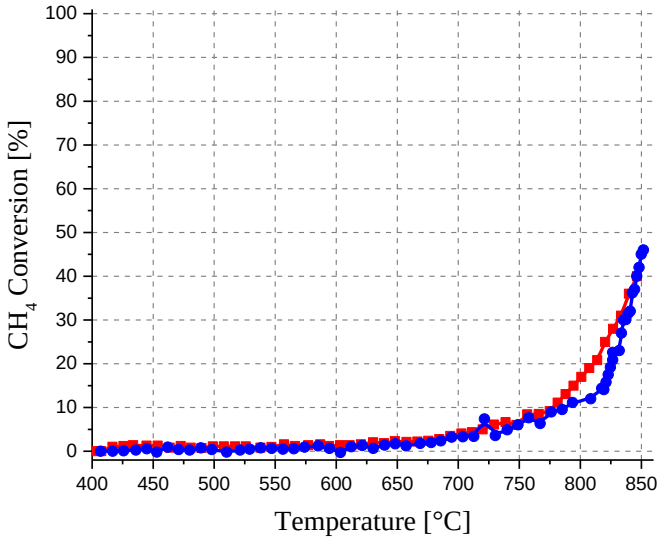

Figure 3.17: 2 $\%CH_4$ + 6 $\%O_2$. $\%CH_4$ Conversion in CH_4+O_2 (stoichiometric) from 400 °C to 850 °C. $SrTi_{0.9}Mo_{0.1}O_3$ (Red) and $SrTi_{0.6}Mo_{0.4}O_3$ (Blue). The GHSV used for tests was 75,000 h^{-1}.

3.7.4 Enhancing methane dry reforming through nickel deposition

The methane reforming, as previously highlighted, is a scientific and industrial important reaction for the production of syngas. Many catalysts were studied for

this purpose but he most used due to the combination of activity, availability and price are nickel metal based [135][136]. For this reason a wet impregnation on the powders was carried out starting from a water solution of nickel nitrates precursors, detail on chapter 2. The compounds obtained had 30% mol/mol of nickel loading. The TPR analysis, table 3.7, revealed the successful of Ni deposition showing the reduction of 88% and 93% of the Nickel expected for $Ni/SrTi_{0.9}Mo_{0.1}O_3$ and $Ni/SrTi_{0.6}Mo_{0.4}O_3$, respectively. The large presence of nickel on surface was confirmed also by the XPS quantitative analysis, table 3.8. Ni deposition did not affect the cation surface concentration of Mo-doped titanates as can be seen comparing table 3.6 and table 3.8. On other hand a larger amount of oxygen was detected due to the hydroxylation of the surface.

In figure 3.18 the results of CO conversion of Ni impregnated compounds vs as prepared $SrTi_{0.9}Mo_{0.1}O_3$ and $SrTi_{0.6}Mo_{0.4}O_3$ are reported. The deposition of 30% mol/mol of Ni have greatly increased the activity on the materials: $SrTi_{0.9}Mo_{0.1}O_3$ reduced its ignition temperature more than 100 °C and achieved total CO conversion at 500 °C; $SrTi_{0.6}Mo_{0.4}O_3$ shown an ignition temperature around 200 °C and its able to reach the total CO conversion at 700 °C. Both the catalysts did not display the plateau suggesting that the oxygen lacking was not the limitation steps. This appears in according with the higher amount of oxygen on the surface.

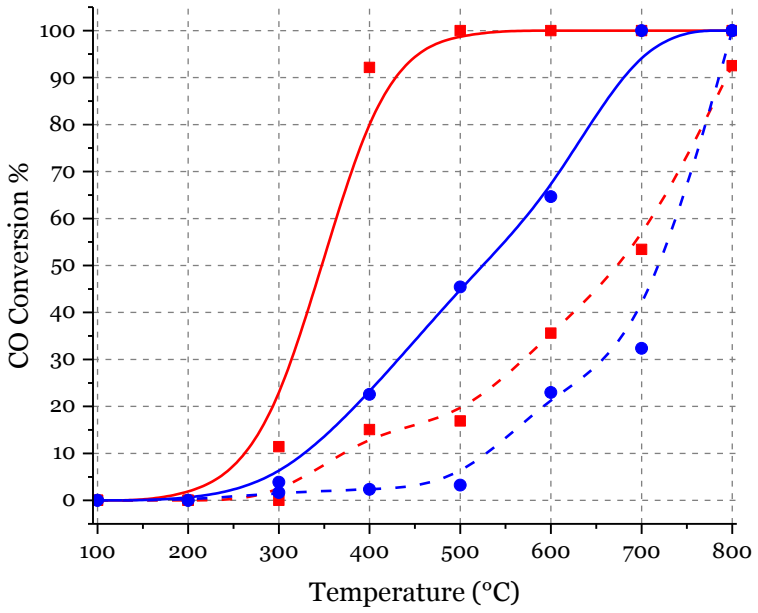

Figure 3.18: 2%CO + 1% O_2. %CO conversion as a function of temperature for 30% mol/mol Ni/$SrTi_{0.9}Mo_{0.1}O_3$ (Red line), 30% mol/mol Ni/$SrTi_{0.4}Mo_{0.6}O_3$ (Blue line), $SrTi_{0.9}Mo_{0.1}O_3$ (Red dashed line) and $SrTi_{0.4}Mo_{0.6}O_3$ (Blue dashed line). The GHSV used for tests was 100,000 h^{-1}.

Table 3.7: TPR H_2 consumption results on Ni 30% mol/mol $SrTi_{0.9}Mo_{0.1}O_3$ and $SrTi_{0.6}Mo_{0.4}O_3$.

[t]= calculated considering the presence of NiO and the reduction to Ni.

Sample	H_2 (cm^3/g) Measured	H_2 (cm^3/g) Expected[1]	H_2 (%) Measured / Expected
Ni-ST9M1	42	49	88%
Ni-ST6M4	43	46	93%

Table 3.8: XPS atomic composition for Ni 30% mol/mol $SrTi_{0.9}Mo_{0.1}O_3$ and $SrTi_{0.6}Mo_{0.4}O_3$.

Sample		Ni	Sr	Ti	Mo	O
Ni-ST9M1		10	12	6	1	72
	Experimental	36	41	21	2	-
		-	64	33	3	-

		8	18	17	2	55
	Nominal	18	41	37	4	-
		-	50	45	5	-
Ni-ST6M4		8	11	5	5	71
	Experimental	29	36	17	17	-
		-	51	24	24	-
		8	18	11	7	55
	Nominal	18	41	25	16	-
		-	50	30	20	-

The reactivity towards methane dry reforming was performed on $Ni/SrTi_{0.9}Mo_{0.1}O_3$ and $Ni/SrTi_{0.6}Mo_{0.4}O_3$, but again only $Ni/SrTi_{0.9}Mo_{0.1}O_3$ shown a decent CH_4 conversion, figure 3.19. The nickel impregnation did not increase the total CH_4 conversion inducing a slightly decreasing in activity at 800 °C: 46% and 45% for CH_4 and CO_2, respectively. On other hands the ignition temperature greatly decreased from 625 °C to 500 °C. The inversion of performance could be observed at 750 °C, where the $Ni/SrTi_{0.9}Mo_{0.1}O_3$ started to have lower conversion than $SrTi_{0.9}Mo_{0.1}O_3$. The catalyst was kept at 800 °C under working condition for 6 hours showing only a small decrease in the conversion after the first hour, 41% CH_4 and 38% CO_2. The performance loss was attributed to the well know carbon formation induced by the presence of Ni [132][135][136] [137].

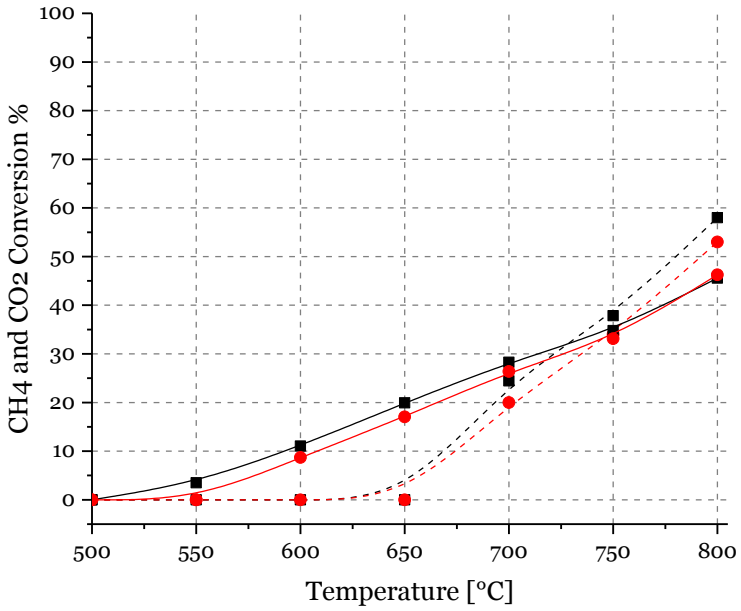

Figure 3.19: 2 %CH_4 + 2 %CO_2. % Conversion in CH_4+CO_2 (stoichiometric) from 500 °C to 800 °C. CH_4 (black line) and CO_2 (Red line) for Ni 30% mol/mol $SrTi_{0.9}Mo_{0.1}O_3$ and CH_4 (black dashed line) and CO_2 (Red dashed line) for $SrTi_{0.9}Mo_{0.1}O_3$. The GHSV used for tests was 75,000 h^{-1}.

The introduction of Ni had induced remarkable improvements on the catalytic behaviour of materials, especially in the CO oxidation. The best advantage on methane dry-reforming was the noteworthy ignition temperatures drop. Although a small deactivation was observed after 1 hour of working, the system $Ni/SrTi_{0.9}Mo_{0.1}O_3$ was active towards methane dry reforming. Notwithstanding the modest results under MDR, the high activity versus CO oxidation has encouraged the electrochemical investigation of $Ni/SrTi_{0.9}Mo_{0.1}O_3$.

3.8 Electrochemical investigation

Among the samples prepared and characterized, the electrochemical investigation was carried on $SrTi_{0.9}Mo_{0.1}O_3$, $Ni/SrTi_{0.9}Mo_{0.1}O_3$ and $Ni/SrTi_{0.6}Mo_{0.4}O_3$. The selection was based on results obtained by catalytic tests in which the compounds

$SrTi_{0.9}Mo_{0.1}O_3$ and $Ni/SrTi_{0.9}Mo_{0.1}O_3$ resulted the most promising and the stability tests under reduction conditions, TPR.

3.8.1 Compatibility between Electrodes and Electrolytes

To investigate the chemical compatibility, the X-ray diffraction (XRD) technique was used. The electrodes and electrolytes were mixed and grinded together in a mortar. The mixed powders were finally fired at high temperature under the same conditions selected for symmetric SOFC preparation, table 3.9.

Table 3.9: Condition used for electrodes/electrolytes compatibility.

Sample	Electrolyte	Conditions
$SrTi_{0.9}Mo_{0.1}O_3$	YSZ	1400 °C 5%H_2/Ar
$SrTi_{0.9}Mo_{0.1}O_3$	GDC	1400 °C 5%H_2/Ar
$SrTi_{0.6}Mo_{0.4}O_3$	YSZ	1400 °C 5%H_2/Ar
$SrTi_{0.6}Mo_{0.4}O_3$	GDC	1400 °C 5%H_2/Ar

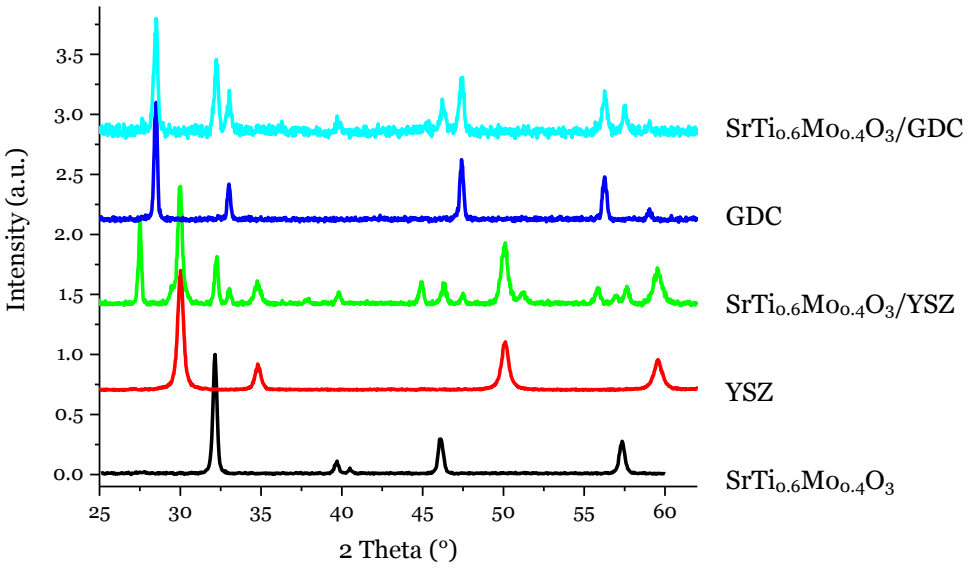

Figure 3.20: XRD patterns of $SrTi_{0.6}Mo_{0.4}O_3$ (black line), YSZ (red line), YSZ + $SrTi_{0.6}Mo_{0.4}O_3$ (green line), GCD (blue line) and GDC + $SrTi_{0.6}Mo_{0.4}O_3$ (light blue line).

The XRD patterns, figure 3.20, have shown the compatibility between titanates and the electrolytes. The electrodes developed seem to have a good chemical compatibility with GDC without displaying any secondary phases. On other hand small secondary phases, $SrMoO_4$, were detected after the treatment with Yttria stabilized zirconia. In order to avoid efficiency drop the symmetric cells prepared were based on GDC pellets and YSZ pellets with a GDC barrier layer. However, as reported in literature, GDC suffers from great thermal coefficient expansion (TEC) change under hydrogen environment [138]. With the aim of testing the expansion compatibility between the compounds, symmetric cells with GDC pellets and YSZ pellets with barrier layers were prepared and fired under hydrogen. In according with thermal expansion reported literatures, the GDC pellets suffer of electrodes delamination while the YSZ pellets with a GDC barrier layers show a perfect compatibility.

3.8.2 Symmetric cell preparation

In order to perform the electrochemical characterization a symmetric cell was prepared. The symmetric cell is a cell which has the same material both pellet faces. This particular configuration allows to study the processes of the electrode desired when both electrodes are in contact with the same environment. The impedance analyses were executed on electrolyte supported button cells: electrode/electrolyte/electrode. The steps involves in the cell assembly were: the pellet preparation, the ink formulation and printing, the electrodes adhesion and the infiltration phase.

3.8.3 Solid electrolyte: Pellet

The electrolyte selected for the tests was Yttria stabilized zirconia (YSZ) which has a high stability in reductive environments and a high mechanical resistance. The electrolyte had to be carefully prepared, in fact, in order to have a suitable ionic mobility the pellet density (d_{pellet}) has to be higher than 94%, equation eq. 3.1:

(eq. 3.1) $$d_{pellet} = (\frac{d_{sperimental}}{d_{theoretical}}) \cdot 100$$

where $d_{sperimental}$ the density of the pellet, and $d_{theoretical}$ is the theoretical density of YSZ, 6.1 g/cm^3. The pellets were prepared starting from 8% Yttria stabilized zirconia (Tosoh Corporation) through dry pressing with conditions reported on table 3.10.

Table 3.10: Condition used for electrolytes preparation

Electrolyte	Mass [g]	Diameter [mm]	Pressing	Thermal treatment	Final Density
YSZ	2.5	25	190 Bar, 30s	Air 1500 °C, 5h, 2°C/min	96-98%

The obtained pellets were finally polished with sand paper and sonicated in an ethanol bath with the purpose of removing the not sintered residues.

3.8.4 Electrodes: from ink to adhesion

The electrodes deposition was performed through a screen printing machine which allows a fine control of the thickness. The main parameters that control the electrodes morphology are: the particles size, the ink and the final thermal treatment.

The particles size were measured by laser diffusion showing a d(0.5) of 4.014 μm and 4.200 μm respectively for $SrTi_{0.9}Mo_{0.1}O_3$ and $SrTi_{0.6}Mo_{0.4}O_3$ which are considerate slightly bigger for anodes applications [19].

The inks printed on electrolyte were prepared with the following formulation, table 3.10.

Table 3.11: Recipe used for ink preparation

% m/m	GDC Barrier layer (%)	Electrode (%)
Electrode powders	38.0	44.0
Dispersant (Terpineol)	10.0	14.0
Binder (ethyl cellulose)	0.7	2.0
Solvent (Dupont)	51.3	50.0
Number of Layers	1	2

Before the ink preparation, the electrode powders were mixed with the 3%wt of pore former, Carbon Super P® (TIMCAL), in order to allow a high porosity after the thermal treatment. The electrode ink and the GDC barrier layer had different formulation since they must have a different morphology. The barrier layer had to be dense and avoid interaction between the YSZ and the electrodes while the electrodes must have a high porosity. For this purpose a careful optimization of ink recipe was carried out.

The thermal treatment was the final step for the cell preparation, figure 3.21. It was the step where the sintering and the adhesion occurred.

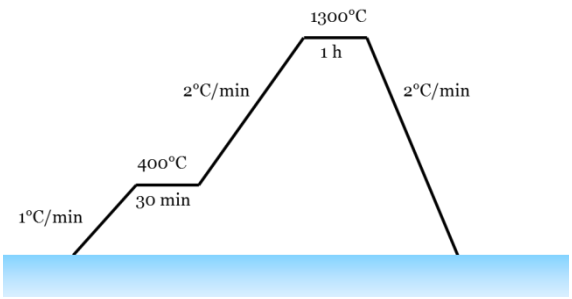

Figure 3.21: Thermal treatment used for titanates electrode adhesion.

The treatment consisted in a very slow heating rate up to 400 °C with the purpose of burning the organic compounds of the ink, followed by a slow heating rate up to the final thermal treatment (sintering and adhesion). Four temperatures were tested in order to verify the adhesion of the electrodes: 1000 °C, 1200 °C, 1300 °C and 1400 °C. Temperatures up to 1200 °C did not allow a good adhesion of the electrodes resulting in the detaching of the layers deposited using a scotch tape. 1300 °C and 1400 °C permit a good adhesion but induce a different morphology that could be observed in figure 3.22. Also the heating rates were optimized in order to improve the final performance of the device.

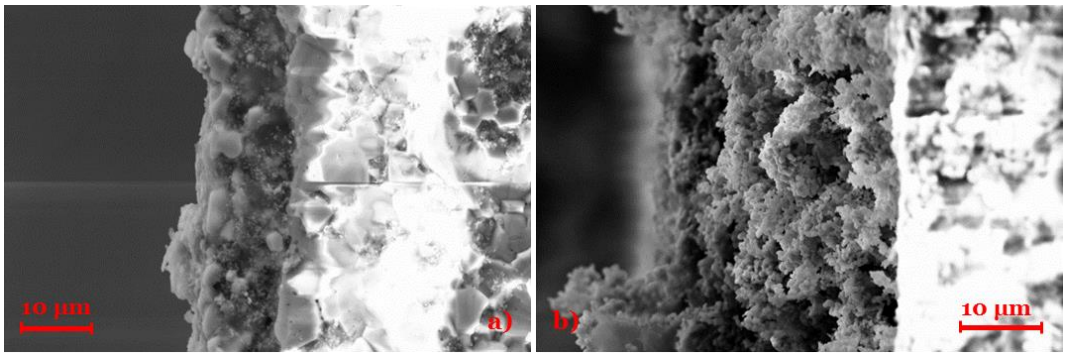

Figure 3.22: SEM images of $SrTi_{0.9}Mo_{0.1}O_3$ treated at 1400 °C a) and 1300 °C b).

The best compromise between adhesion and the porosity, figure 3.22, was observed at 1300 °C.

Before the ink deposition, a GDC barrier layer was printed and treated at 1300 °C in order to obtain a thin dense layer. The temperature chosen was the highest possible without exceed the electrode final thermal treatment. The thickness of the final electrode layer was around 30 µm. Two types of symmetric cells were prepared, one with only the electrodes and second one with nickel infiltrated in the electrodes backbones.

3.8.5 Infiltration

Nickel infiltration has the purpose of increasing the electrochemical activity of the device. The infiltration procedure was performed on the symmetric electrode/electrolyte/electrode completed cell. A water solution of 1M of nickel nitrates was dripped on the electrode. Then the cell was placed under vacuum for 2 minutes. The excess of solution was removed with a paper and the cell was heated up to 450 °C for 30 minutes in order to decompose the nitrates. This procedure was repeated three times for each side of the cell. At the end a thermal treatment at 800 °C under 5% H_2/Ar for 1 hour was performed. The final loading result around 14% wt respect to electrode corresponding to around 30% mol/mol. The success of infiltration was confirmed by the SEM investigation carried out on the final pellets. The figure 3.23 and figure 3.24 show the homogeneous dispersion of Ni particles on the backbone of $SrTi_{0.9}Mo_{0.1}O_3$ and $SrTi_{0.6}Mo_{0.4}O_3$ respectively. $SrTi_{0.6}Mo_{0.4}O_3$ shown a higher porosity and smaller Ni particle diameters (the average diameter is 20-30 nm) compared with $SrTi_{0.9}Mo_{0.1}O_3$ (about 100nm particle diameters). This behaviour was observed in all the samples prepared suggesting the contribution of backbone to the particles formation.

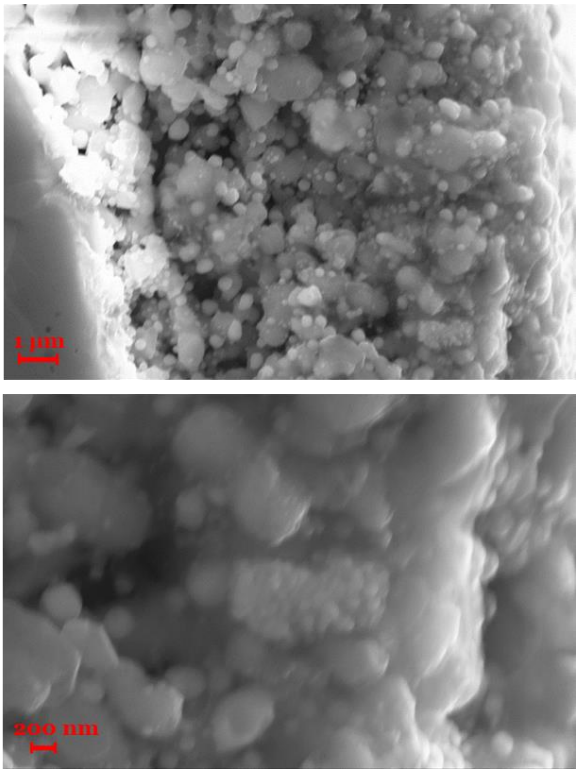

Figure 3.23: SEM images of $Ni/SrTi_{0.9}Mo_{0.1}O_3$ treated at 1300 °C

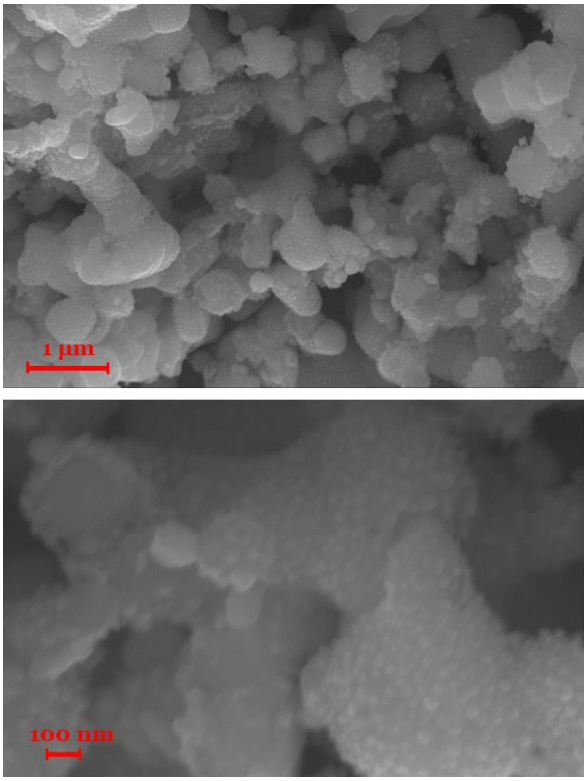

Figure 3.24: SEM images of Ni/$SrTi_{0.6}Mo_{0.4}O_3$ treated at 1300 °C

A current collector based on Ni was printed on both the sides of the cell with the aim of collecting the electrons and help the gas diffusion on the electrodes. The prepared cell was finally treated at 800 °C for 1 h under 5% H_2/Ar. The schematic representation of symmetric cell is display in figure 3.25.

Figure 3.25: Pictures of final symmetric cell (left) and the schematic representation of it (right).

3.8.6 Impedance analysis

Impedance spectroscopy is one of the main techniques for SOFC materials characterization and evaluation of electrochemical performance. It is highly sensitive toward sample configuration and fabrication but allow to investigate the polarization processes of the material. In fact, every polarization losses have a different frequency of response (semi-circle signal). The shape and the size of the impedance signal give useful information about the system studied. The electrochemical measurements (EIS) were performed in an appropriate furnace using a PGSTAT 302 Autolab Frequency Response Analyser [134]. The symmetric cell was placed between two gold grids and pressed with a mechanical load. The measurements were carried out at steady state condition (zero DC current) in the frequency range of 10^{-2}-10^{6} Hz and with signal amplitude of 50mV. The explored temperature range was between 500 °C and 830 °C and the cell was kept under constant flow of 100mL/min of 5%H_2 in argon. A pre-treatment under 5% H_2/Ar at 800 °C for 1 hour was performed every time before the electrochemical measurements.

Impedance spectra were collected for thee symmetric cells: $SrTi_{0.9}Mo_{0.1}O_3$, Ni/$SrTi_{0.9}Mo_{0.1}O_3$ and Ni/$SrTi_{0.6}Mo_{0.4}O_3$. In figure 3.26 an example of impedance spectra is reported.

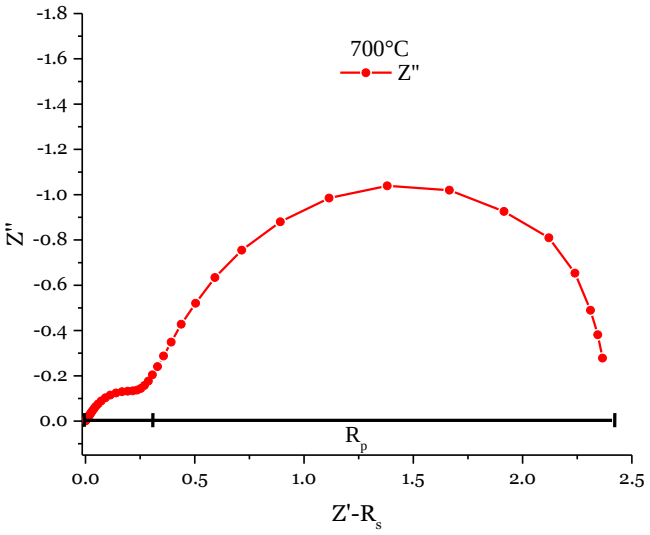

Figure 3.26: Nyquist plot of Ni-$SrTi_{0.6}Mo_{0.4}O_3$ at 700°C under 100 cm^3/min of Hydrogen.

The electrolyte resistance (R_s) represents the contribution of bulk diffusion and inter grain diffusion on the electrolyte. It depends on the type, the thickness and the preparation history of the electrolyte. In order to have an easily understanding of the Nyquist plot, R_s was subtracted from figure 3.26. The R_p is the resistance polarization; it is the sum of interface, reaction and gas diffusion resistance. In order to compare the results obtained by impedance analysis, the R_p is usually normalized by the surface area of the electrodes, eq.3.2, so as to obtain the Area Specific Resistance.

(eq. 3.2) $$ASR = (R_{interface} + R_{reacton} + R_{diffusion\ gas}) \cdot \frac{S_{electrde}}{2}$$

Where $R_{interface}$, $R_{reaction}$ and $R_{diffusion\ gas}$ are the resistances respectively of interface processes, the electrochemical reactions on surface and the gas diffusion. $S_{electrode}$ is the area of the electrodes used.

In figure 3.27 the evolution of ASR versus the temperature from 500 °C to 830 °C for the samples $SrTi_{0.9}Mo_{0.1}O_3$, Ni-$SrTi_{0.9}Mo_{0.1}O_3$ and Ni-$SrTi_{0.6}Mo_{0.4}O_3$ can be observed.

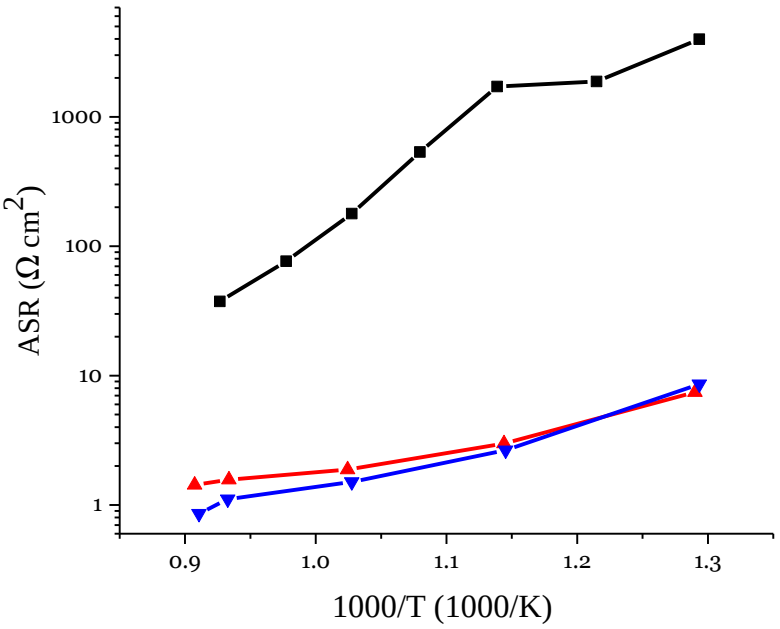

Figure 3.27: The area specific resistance (ASR) Arrhenius plot for: $SrTi_{0.9}Mo_{0.1}O_3$ (black), Ni/$SrTi_{0.9}Mo_{0.1}O_3$ (red) and Ni/$SrTi_{0.6}Mo_{0.4}O_3$ (blue).

The ASR observed in all the samples decreased as function of the temperatures confirming the thermal activation of the electrodes. The ASR values achieved at 700 °C were 178.70 Ω·cm², 1.88 Ω·cm² and 1.50 Ω·cm² for $SrTi_{0.9}Mo_{0.1}O_3$, Ni/$SrTi_{0.9}Mo_{0.1}O_3$ and Ni/$SrTi_{0.6}Mo_{0.4}O_3$. By increasing the temperature up to 800 °C the ASR fall down resulting 37.48 Ω·cm², 1.57 Ω·cm² and 1.10 Ω·cm², respectively. Although $SrTi_{0.9}Mo_{0.1}O_3$ showed the highest ASR in all the samples tested, by increasing the working temperatures from 700 °C to 800 °C its resistance dropped of 79% while all the others electrodes improved only of 20%.

The best result, 0.85 Ω·cm², was obtained with $SrTi_{0.6}Mo_{0.4}O_3$ infiltrated with 14%wt of Ni at 830°C. The value found is two orders of magnitude better than the sample $SrTi_{0.9}Mo_{0.1}O_3$ without Ni infiltration (27.2 Ω·cm²) and 0.57 Ω·cm² less than the sample $Ni/SrTi_{0.9}Mo_{0.1}O_3$. These results displayed that Ni particles on $SrTi_{1-x}Mo_xO_3$ can impressively improve the performances. Although the great decrease of ASR is promising, a reasonable ASR value for a SOFC anode should be around 0.15 Ω·cm² [139]. In order to compare the results, a symmetric cell based on a GDC backbone infiltrated with the same amount of Nickel in $Ni/SrTi_{0.9}Mo_{0.1}O_3$ was prepared with the same procedure used for Mo-doped perovskites and tested (Ni-GDC/GDC layer/YSZ/GDC layer/Ni-GDC). The ASR observed, 5.68 Ω·cm², is far away from the value expected from literature, around 0.05 Ω·cm² at 700 °C [140]. This suggests that the preparation steps could require an attention optimization and leaves room for improvement for Mo-doped titanates infiltrated with nickel.

The Arrhenius plot of ASR allowed to calculate the activation energy for the different electrodes by the use of the following equation:

(eq. 3.3) $$E_a = k \cdot \frac{8.32 \cdot \ln(10) \cdot 1000}{96485}$$

Where k is the angular coefficient obtained by the linear fitting of the ASR for different temperatures.

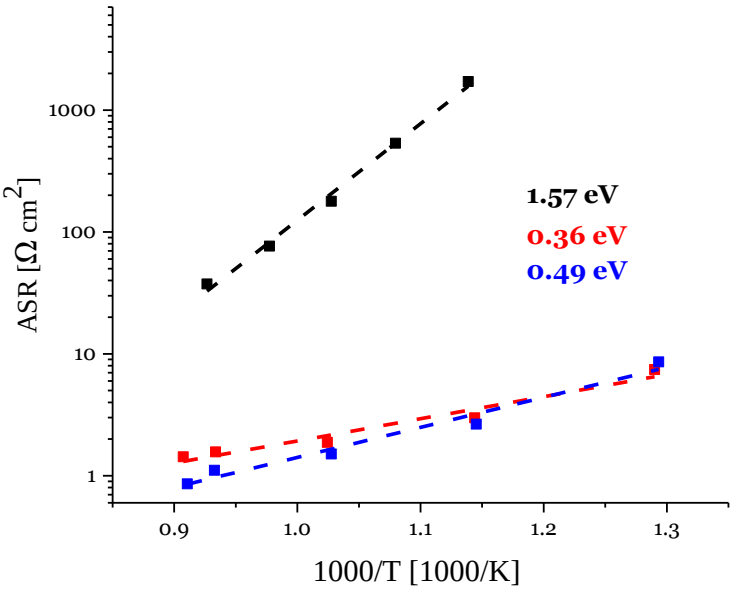

Figure 3.28: Fitting of ASR values as function of temperature for, $SrTi_{0.9}Mo_{0.1}O_3$ (black), $Ni/SrTi_{0.9}Mo_{0.1}O_3$ (red) and $Ni/SrTi_{0.6}Mo_{0.4}O_3$ (blue) and their activation energies.

The Ni infiltration induced a great decrease of the E_a for $SrTi_{0.9}Mo_{0.1}O_3$ dropping the value from 1.57 eV to 0.36 eV which is even better than the E_a calculated for $Ni/SrTi_{0.6}Mo_{0.4}O_3$ (0.49 eV).

With the purpose of understanding which processes were involved in the polarization loss of $Ni/SrTi_{0.9}Mo_{0.1}O_3$ and $Ni/SrTi_{0.6}Mo_{0.4}O_3$, the impedance spectra were fitted and starting from the data collected it was possible to propose the equivalent circuits for the systems studied.

The spectra registered above 600 °C could be modelled with equivalent circuit reported in figure 3.29, while from 600 °C and below 700 °C the contribution of charge transfer electrode/electrolyte rise up at high frequencies and another contribution appear. In figure 3.30 is reported, as an example, the fitting result carried out on $Ni/SrTi_{0.6}Mo_{0.4}O_3$ at three different temperatures. The equivalents

circuits, thought the equation eq. 3.4, allowed to calculate the capacitance of each contributions, C_e, and so to distinguish the processes,[141]

(eq. 3.4) $$C = R^{[\frac{1-n}{n}]} \times CPE^{(\frac{1}{n})}$$

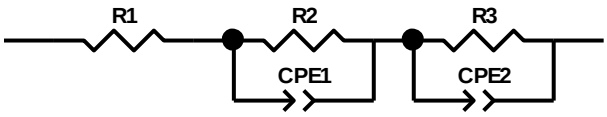

Figure 3.29: The equivalent circuit used to fitting the electrochemical impedance spectra above 600 °C.

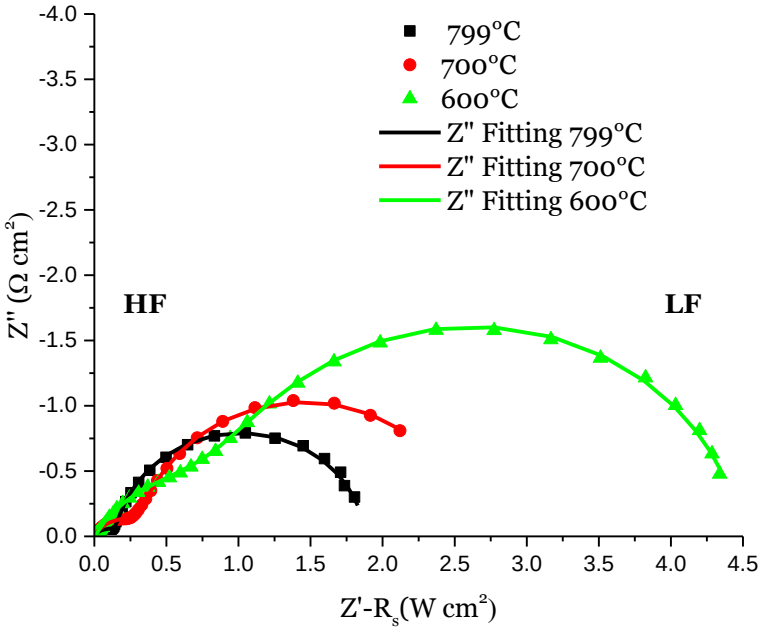

Figure 3.30: Nyquist plot of Ni-$SrTi_{0.6}Mo_{0.4}O_3$ at 600 °C (green), 700 °C (red) and 799 °C (black) under 100 cm^3/min of Hydrogen in argon. The electrolyte resistance R_s was subtracted for a better comparison. Dots are the experiment data and lines are the fitting used for the analysis. High frequencies (HF), Low frequencies (LF).

The data analysed, for both the symmetric cells, suggested two large contributions associated to the electrode processes. The capacitance values found,

figure 3.31, are in agreement showing the main contributions in the range at 10^{-2}-10^{0} F [141][142]. This could be explained by the low electro-catalytic performance of titanates [19]. The two contributions in fact were probably related to the reactions occurred on three phase boundaries formed between Ni and the backbone, smaller contribution, and the reactions occurred on perovskites surface, larger contribution. The absence of the charge transfer electrode/electrolyte at high temperature indicated that electrochemical reactions on the surface could be the rate determining step of the electrode [142]. It is to point out that the absence other contributions could be hidden by bigger polarization resistances. The impedance spectra, figure 3.30, and the small change observed for the capacitances, figure 3.31, as the function of temperatures suggested that there are not significant changes in the microstructures or in the compositions in the electrodes or at interfaces at the tested conditions (830 °C under 5% dry H_2/Ar) [141].

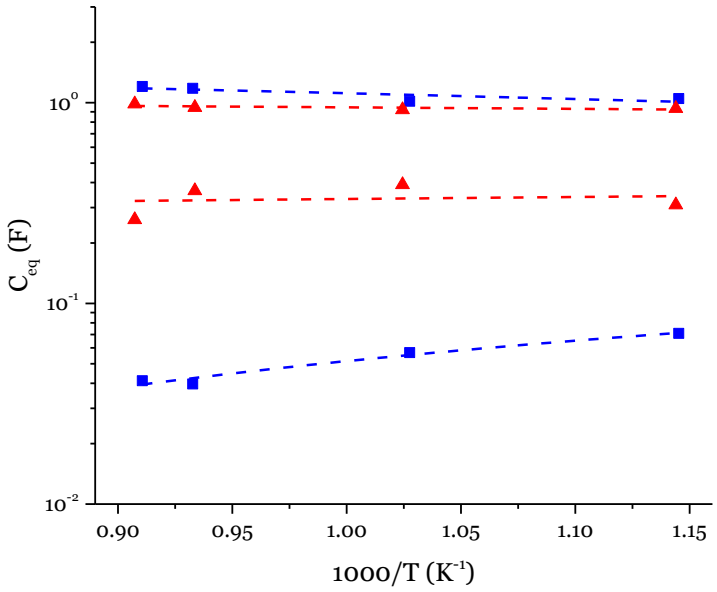

Figure 3.31: Arrhenius plot of the capacitances for Ni/$SrTi_{0.9}Mo_{0.1}O_3$ (red) and Ni/$SrTi_{0.6}Mo_{0.4}O_3$ (blue).

3.9 Chapter conclusions

In this work the Mo-doped and Fe-doped $Ba_{1-x}SrTiO_3$ (x= 0.5, 1) were studied as anode for solid oxide fuel cell directly feed with bio-gas (CH_4 and CO_2). Particular attention was given to the elements selection in order to avoid critical raw materials (CRM) due to their high cost and supply difficulties [72].

The citrate method used allowed to obtain high crystalline purity on all the compounds prepared. The Fe-doped titanates were easily synthetized through calcination under air (1000 °C for 6 hours) while Mo-doped titanates required peculiar pO_2 pressure conditions. The desired phases of $SrTi_{0.9}Mo_{0.1}O_3$, $SrTi_{0.6}Mo_{0.4}O_3$ and $Ba_{0.5}Sr_{0.5}Ti_{0.9}Mo_{0.1}O_3$ were achieved through reductive thermal treatments (1200 °C under 5% wet H_2/Ar the Mo-doped and 1000 °C under 5% H_2/Ar with ethanol-water vapour $Ba_{0.5}Sr_{0.5}Ti_{0.9}Mo_{0.1}O_3$) .

The high temperatures involved in the compounds preparations could be the causes of the large particle diameters observed with the SEM images and with laser diffusion technique, d(0.5) nearly 4µm. SEM images have also proven a partial sinterization between the starting particles.

The stability tests (TPR/TPO) performed on samples powders have revealed high stability of $SrTi_{0.9}Mo_{0.1}O_3$, $SrTi_{0.6}Mo_{0.4}O_3$ and $Ba_{0.5}Sr_{0.5}Ti_{0.9}Mo_{0.1}O_3$ under reductive conditions (5% H_2/Ar up to 900 °C) but an insulation phase segregation, $SrMoO_4$ and $BaMoO_4$ depending from the A-site cations, appeared above 500 °C under oxidising conditions. The instability under oxidizing environment did not affect the performance under working conditions but it might induce particular attention during the cell preparation. Only the compound $SrTi_{0.9}Mo_{0.1}O_3$ has shown a total structure restoration after TPO/TPR treatments. The Fe-doped titanates displayed different redox behaviour. Although they have been calcinated under air, under reducing atmosphere both $Ba_{0.5}Sr_{0.5}Ti_{0.9}Fe_{0.1}O_3$ and $Ba_{0.5}Sr_{0.5}Ti_{0.6}Fe_{0.4}O_3$ shown large reduction of Fe(III) to Fe(0). The presence of Fe metal is also clearly visible from XRD pattern carried out after TPR. However the H_2 consumption, table 3.2, shown that the total iron reduction was not achieved suggesting the partial stabilization of iron cation in the perovskite structure.

All the materials were highly active towards CO oxidation under working temperature condition. The total CO conversion was observed on $Ba_{0.5}Sr_{0.5}Ti_{0.9}Fe_{0.1}O_3$ and $SrTi_{0.6}Mo_{0.4}O_3$ while $SrTi_{0.9}Mo_{0.1}O_3$ stopped at 93% at 800 °C. $Ba_{0.5}Sr_{0.5}Ti_{0.9}Fe_{0.1}O_3$ and $Ba_{0.5}Sr_{0.5}Ti_{0.9}Mo_{0.1}O_3$ reached 85% and 80% respectively. Among the samples tested, $SrTi_{0.9}Mo_{0.1}O_3$ was the only material that reached a decent activity versus methane dry reforming, 58% of CH_4 and 53% of CO_2 conversion at 800 °C. The material was kept in working condition for 6 hours

without showing decreasing in conversion. The curious activity observed is probably due to a synergic effect between Ti and Mo (Ti/Mo = 9/1) which was not observed on the other Mo-doped compounds. The higher stability and the interesting reactivity observed for $SrTi_{0.9}Mo_{0.1}O_3$ and $SrTi_{0.6}Mo_{0.4}O_3$ had encouraged focusing on these systems as anode for solid oxide fuel cell. With the purpose to enhancing the catalytic behaviour nickel deposition (30%mol) on $SrTi_{0.9}Mo_{0.1}O_3$ and $SrTi_{0.6}Mo_{0.4}O_3$ was carried out. As expected the CO oxidation received a remarkable boost achieving the total conversion at 500 °C and 700 °C respectively for $SrTi_{0.9}Mo_{0.1}O_3$ and $SrTi_{0.6}Mo_{0.4}O_3$. Again only $Ni/SrTi_{0.9}Mo_{0.1}O_3$ showed a decent activity toward methane dry reforming. Although the CH_4 conversions slightly decrease from 58% to 41%, the ignition temperature drops (from 650 °C to 500 °C). The reactivity tests confirms that although some optimization steps are still required such as synthesis and the nickel particles dispersion, $Ni/SrTi_{0.9}Mo_{0.1}O_3$ could be used as material for the methane dry reforming.

Due to the instability observed for the Fe-doped compounds under reductive environment, TPR analysis, the electrochemical investigation was performed only on Mo-doped titanates.

The realization of symmetric cells and impedance spectra investigation has demonstrated the feasibility to use $SrTi_{0.9}Mo_{0.1}O_3$ and $SrTi_{0.6}Mo_{0.4}O_3$ infiltrated with 15wt% with nickel as anode for solid oxide fuel cell. The area surface resistance detected (ASR) for $Ni/SrTi_{0.9}Mo_{0.1}O_3$ and $Ni/SrTi_{0.6}Mo_{0.4}O_3$ at 800 °C under 5% of dry H_2 were 1.57 $\Omega \cdot cm^2$ and 1.10 $\Omega \cdot cm^2$ respectively. A reasonable ASR value for a SOFC anode should be around 0.15 $\Omega \cdot cm^2$; however the materials studied are still interesting since many optimizations could be performed in the synthesis and in the electrode preparation (adhesion and infiltration) [139].

Moreover the tests were performed at low dry H_2 concentration which is reported to affect negatively the anode performance [143][144]. The lowest ASR, 0.85 Ω·cm², was achieved at 830 °C with $Ni/SrTi_{0.6}Mo_{0.4}O_3$ which is a remarkable value comparing with other titanates from literatures: $La_{0.5}Sr_{0.5}Ti_{0.75}Ni_{0.25}O_3$ 0.55 Ω·cm² (800 °C pure H_2), 6.3%Ni-8.3GDC-$La_{0.57}Sr_{0.15}TiO_3$ 0.73 Ω·cm² (800 °C pure wet H_2), $La_2Sr_4Ti_6O_{19}$ 2.97 Ω·cm² (900 °C pure wet H_2), 0.5 Ω·cm² Ni 4%wt CeO_2 6%wt $La_{0.3}Sr_{0.7}TiO_3$ (800 °C pure H_2) and 1 Ω·cm² Ni-GDC 30% $La_{0.2}Sr_{0.8}TiO_3$ 70% wt (800 °C wet pure H_2) [19][35][38][145][146].

The ASR values observed at 800 °C for the compounds prepared are still high for a real application in a fuel cell. However the absences of critical raw materials, especially rare earth elements, encourage more study on these materials.

Chapter 4

4.1 Introduction to chapter 4

In this chapter Ruddlesden Popper cobalt base perovskite, A_2BO_4, doped with strontium in the A-site and copper or nickel in the B-site have been studied as electrodes for symmetric solid oxide fuel cell fed with methane. The materials were developed starting from the promising results obtained on cobalt based ABO_3 perovskite ($La_{0.5}Sr_{0.5}Co_{0.5}CuO_3$) as cathode for intermediate temperatures [22]. The compounds prepared were tested under CO oxidation and methane oxidation with the aim to understand their catalytic proprieties. Subsequently their electrochemical proprieties as cathode were investigated on symmetric cells at "Institut de Chimie de la Matière Condensée de Bordeaux CNRS" under the supervision of prof. Fabris Mauvy while their behaviour as anode, under methane environments, were studied at University of Padova under the supervision of prof. Antonella Glisenti.

Two Co-based perovskites with Ruddlesden Popper structure have been considered as electrodes for symmetric solid oxide fuel cell [147]:

1. $(LaSr)_2Co_{0.5}Cu_{0.5}O_4$
2. $(LaSr)_2Co_{0.5}Ni_{0.5}O_4$

4.2 Material preparation

4.2.1 Synthesis

The cobaltates were prepared through citrate method followed by auto-combustion and a thermal treatment under air. The detailed steps of the synthesis were already described in chapter 2. In table 4.1 the parameters used for thermal treatments are summarized.

Table 4.1: Optimized parameters for thermal treatment of each prepared compounds

Sample	Label	Conditions
$(LaSr)_2Co_{0.5}Cu_{0.5}O_4$	(LS)2CC	900 °C, 6 h, 6 °C/min, Air
$(LaSr)_2Co_{0.5}Ni_{0.5}O_4$	(LS)2CN	900 °C, 6 h, 6 °C/min, Air

4.2.2 Characterization

The material prepared shown a good degree of crystallinity but also the presence of secondary phases, whose presence, however, could be an interesting added value. The phase formation was confirmed by the comparison of XRD patterns with JCPDS database.

4.2.3 Structure investigation (XRD)

The synthesis succesful of $(LaSr)_2Co_{0.5}Cu_{0.5}O_4$ was confirmed by the XRD pattern in figure 4.1. The reflexes of the desired phases were compared with $(LaSr)_2CoO_4$ from JCPDS database showing a shift to lower 2theta angles confirming the cobalt substitution with copper into the perovskite cell. The shift to lower angles in fact was explained by the different cation radius between Co(III), 0.55 Å, and Cu(II), 0.73 Å. The secondary phase observed was $La_2Co_{0.75}Cu_{0.25}O_4$ which is an ionic-electronic conduction phase which should be no negatively affecting the

final performance of electrode [126][147]. Beside $La_2Co_{0.75}Cu_{0.25}O_4$ no other secondary phases were observed.

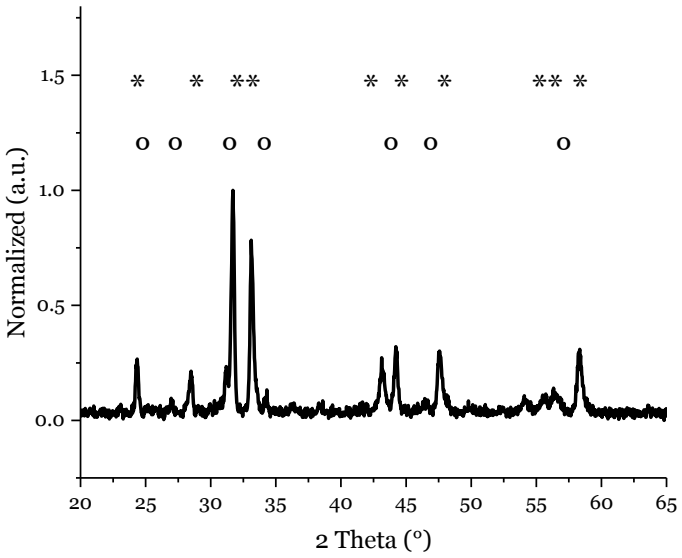

Figure 4.1: XRD patterns of $(LaSr)_2Co_{0.5}Cu_{0.5}O_4$ (black line).

(*) $(LaSr)_2CoO_4$ (tetragonal) 01-083-2408 JCPDS database

(°) $La_2Co_{0.75}Cu_{0.25}O_4$ (Orthorombic) 01-082-1940 JCPDS database

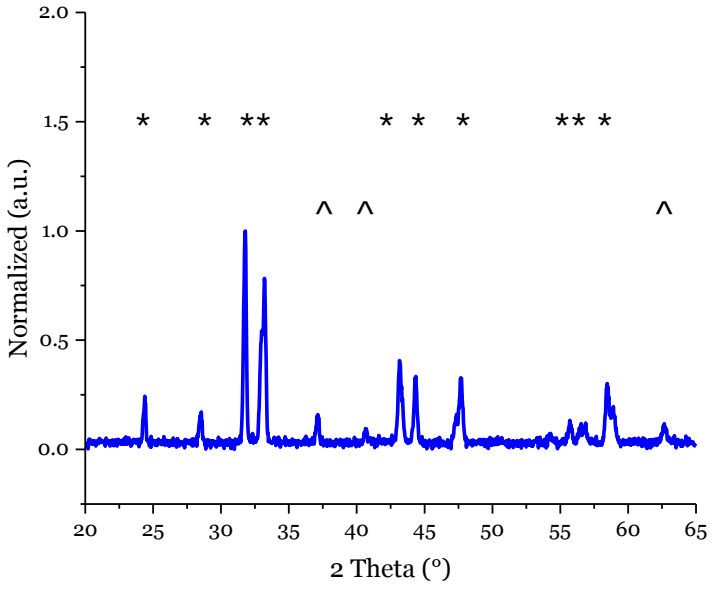

Figure 4.2: XRD pattern of $(LaSr)_2Co_{0.5}Ni_{0.5}O_4$(blue line).

(*) $(LaSr)_2CoO_4$ (tetragonal) 01-083-2408 JCPDS database

(^) NiO (cubic) 01-078-0429 JCPDS database

Figure 4.2 displays the XRD patterns diffraction of $(LaSr)_2Co_{0.5}Ni_{0.5}O_4$ confirming the presence of the desired phase. Traces of NiO were also detected. As in the previous sample, comparing the XRD patterns of $(LaSr)_2Co_{0.5}Ni_{0.5}O_4$ with $(LaSr)_2CoO_4$ from JCPDS database it could be observed a shift to lower angles. This is in according with the ionic radius for Co(III), 0.55 Å, and Ni(III), 0.60 Å, cations [126]. The magnification of the most intense reflex, 31.7°-31.8°, has highlighted the shift of doped cobaltates compared with $(LaSr)_2CoO_4$. It shown also the larger shift induced by copper than nickel, figure 4.3. This was explained, beside segregation detected, by the higher ionic radius difference between cobalt and copper respect cobalt and nickel.

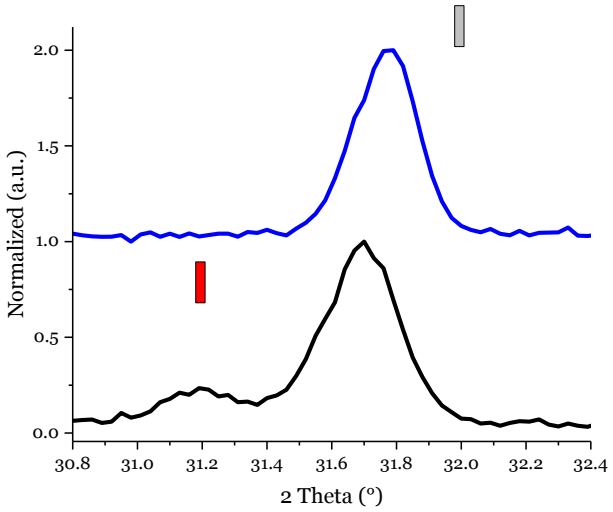

Figure 4.3: magnification of the most XRD intense reflex of $(LaSr)_2Co_{0.5}Cu_{0.5}O_4$ (black line) and $(LaSr)_2Co_{0.5}Ni_{0.5}O_4$ (blue line).

(red bar) $La_2Co_{0.75}Cu_{0.25}O_4$ (Orthorombic) 01-082-1940 JCPDS database

(grey bar) $(LaSr)_2CoO_4$ (tetragonal) 01-083-2408 JCPDS database

4.3 Redox behaviour

4.3.1 Temperature programmed reduction

The materials were developed with the aim of being used as electrodes in symmetric cells. For this reason the temperature programmed reduction (TPR) was utilized to determine the reducibility of cations and their stability under reducing condition.

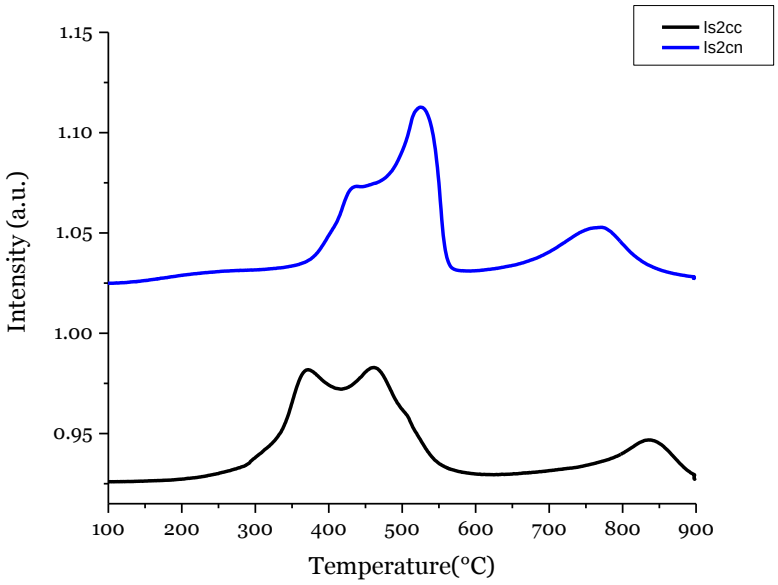

Figure 4.4: Temperature programmed reduction on $(LaSr)_2Co_{0.5}Cu_{0.5}O_4$ (black line) and $(LaSr)_2Co_{0.5}Ni_{0.5}O_4$ (blue line). 5%H_2/Ar from RT to 900 °C.

The sample $(LaSr)_2Co_{0.5}Ni_{0.5}O_4$ in figure 4.4 shows three main reduction peaks: 435 °C, 523 °C and 765 °C. As suggested from literature, the reduction occurs into multiple steps [148][149][150][151]. According with literature, the two low temperature peaks, 435 °C and 523 °C, should be attributed to the sum of two processes: the reduction Ni(III)/Ni(II) and Co(III)/Co(II). However the total H_2 consumption Table 4.2, revealed an experimental consumption higher than the theoretical one (calculated consider Co(III) and Ni(III)). This this could be explained by the partial presence of Co(IV) (placed between 400 °C and 450°C) in $(LaSr)_2Co_{0.5}Ni_{0.5}O_4$ induced by the A-site cation Sr(II) [64]. The fitting procedure suggested that only cobalt was partially oxidised to Co(IV) whereas nickel kept three as oxidation state. The estimation of Co(IV) calculated by the H_2 consumptions, table 4.2, was around 50% of the total cobalt. Taking in account the H_2 peak consumptions, table 4.3, it could be observed that the reduction M(II)/M(0) did not occur only at 765 °C (peak II) but also at lower temperatures

(peak I). The double reduction steps of M(II)/M(0) could be explained by the two different structures (perovskite and rock salt) presented in K_2NiF_4 [152]. First the reduction of M(II)/M(0) cations in the perovskite lattice and then at higher temperature in the rock salt one.

The peak placed at 765 °C, in according with the literature for $(LaSr)_2CoO_4$ and $(LaSr)_2NiO_4$ compounds, could have led to the breakdown of structure to discrete phases, La_2O_3, SrO, Ni and Co [152][153][154][155]. $(LaSr)_2Co_{0.5}Cu_{0.5}O_4$, in figure 4.4, shows a TPR data similar to the $(LaSr)_2Co_{0.5}Ni_{0.5}O_4$. It has shown three main peaks: 368 °C, 468 °C and 840 °C. As reported in literatures, copper doping induces higher ion mobility and therefore a low reduction temperature of cations [21][148]. As observe in $(LaSr)_2Co_{0.5}Ni_{0.5}O_4$, several reductions processes are involved. The main peaks were attributed at Cu(II)/Cu(0) and Co(III)/Co(II), at 368 °C and 460 °C respectively. However the fitting analysis and the total H_2 consumption suggest the presence of the species Co(IV) and Cu(III) (between 300 °C and 400 °C) induced by Sr(II). The Co(II)/Co(0) was placed at 839 °C which was considerably higher than the reduction M(II)/M(0) observed in $(LaSr)_2Co_{0.5}Ni_{0.5}O_4$ but in according with what observed in literature on $(LaSr)_2CoO_4$ and $(PrSr)_2CoO_4$ [153][156]. Copper doping usually induce lower reducibility of cations, due to higher hydrogen dissociation on copper surface when segregated [157][158][159]. However this effect was not observed on Co(II) bulk probably due to the particular K_2NiF_4 type structure which could not allow the copper activation on deep bulk cobalt cations. The H_2 peak consumption revealed also in this case the partial reduction of Co(II)/Co(0) at around 500 °C.

Table 4.2: H_2 consumption data obtained by TPR analysis on $(LaSr)_2Co_{0.5}Ni_{0.5}O_4$ and $(LaSr)_2Co_{0.5}Cu_{0.5}O_4$.
*theoretical values were calculated considering the reduction Co(III)/Co(0), Ni(III)/Ni(0) and Cu(II)/Cu(0).

	H_2 Total Consumption (mol/mol)		**Δ(%)**
	Experiment	**Theoretical***	
$(LaSr)_2Co_{0.5}Ni_{0.5}O_4$	1.63	1.50	9
$(LaSr)_2Co_{0.5}Cu_{0.5}O_4$	1.74	1.25	39

Table 4.3: H_2 peak consumption data obtained by TPR analysis on $(LaSr)_2Co_{0.5}Ni_{0.5}O_4$ and $(LaSr)_2Co_{0.5}Cu_{0.5}O_4$.
*% respect the total H_2 consumption.

	H_2 Peak consumption			
	I peak (mol/mol) 300-600°C	**(%)***	**II peak (mol/mol) 700-800°C**	**(%)***
$(LaSr)_2Co_{0.5}Ni_{0.5}O_4$	1.24	76	0.39	24
$(LaSr)_2Co_{0.5}Cu_{0.5}O_4$	1.48	84	0.27	16

4.4 Powder morphology

The powders prepared by means of the citrated method, see details chapter 2, were investigate through Scanning Electron Microscopy (SEM), to study the particles morphology, BET analysis, to detect the surface area, and laser diffusion, to observed the particle size distribution (Matersizer 2000).

The SEM images of cobaltates prepared are reported in figure 4.5. The images revealed homogeneity in particles shape and size. $(LaSr)_2Co_{0.5}Cu_{0.5}O_4$ displayed particles diameters bigger than $(LaSr)_2Co_{0.5}Ni_{0.5}O_4$, between 200-300 nm and less than 200 nm respectively. Although both the compounds shown a partial

sinterization creating aggregate structures, $(LaSr)_2Co_{0.5}Ni_{0.5}O_4$ exhibited a more compacted structure than $(LaSr)_2Co_{0.5}Cu_{0.5}O_4$.

The particle size distributions, figure 4.6 and figure 4.7, displayed two maximum for both the samples. The two peaks of $(LaSr)_2Co_{0.5}Cu_{0.5}O_4$ were placed at 0.7 μm and 13.2 μm while the peaks in $(LaSr)_2Co_{0.5}Ni_{0.5}O_4$ could be found at 0.7 μm and 17.1 μm. The large particles diameters observed could be explained by the high temperature used for the synthesis of these compounds (900°C). The analysis shown that $(LaSr)_2Co_{0.5}Ni_{0.5}O_4$ had larger and wider particles than $(LaSr)_2Co_{0.5}Cu_{0.5}O_4$, 13.2 μm versus 17.1 μm looking the most abundant peak. The large particle diameters with a sintered compact morphology suggest lower surface area. This is in according with the surface area obtained through BET analysis. The surface areas of samples were 7 and 6 m^2/g for $(LaSr)_2Co_{0.5}Cu_{0.5}O_4$ and $(LaSr)_2Co_{0.5}Ni_{0.5}O_4$, table 4.4, which was slightly smaller compared with similar compounds prepared in the same conditions (9-12 m^2/g) [21].

The common parameter to describe the particle size distribution is d(0.5). It is the diameter within the 50% of the particles is smaller than. The d(0.5) of $(LaSr)_2Co_{0.5}Cu_{0.5}O_4$ and $(LaSr)_2Co_{0.5}Ni_{0.5}O_4$ were 11.8 μm and 14.5 μm respectively.

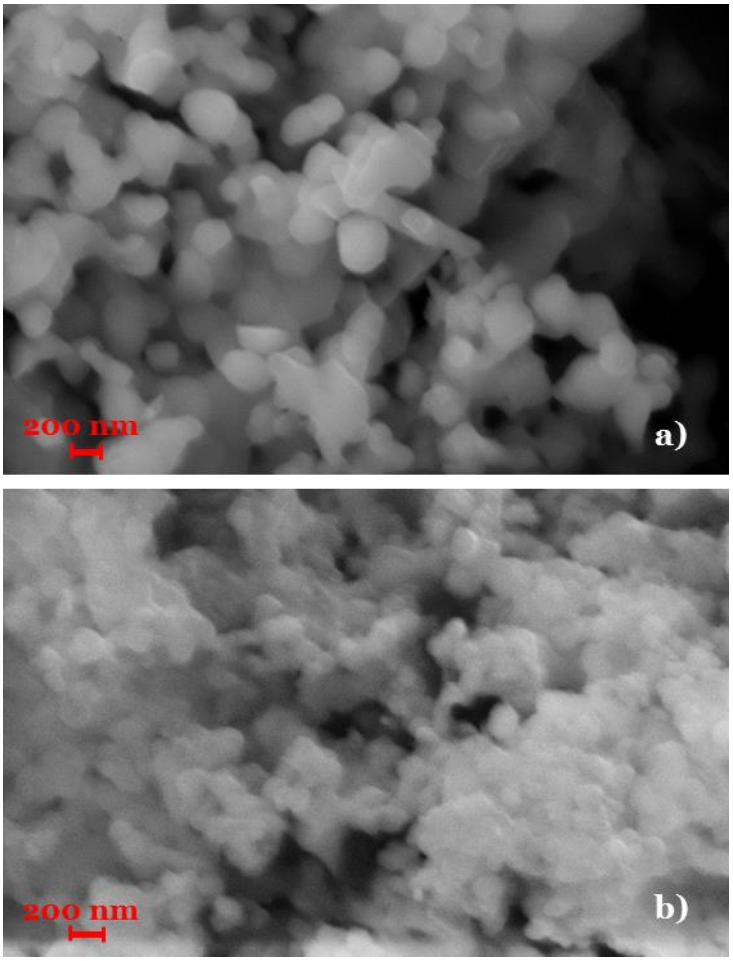

Figure 4.5: SEM images for $(LaSr)_2Co_{0.5}Cu_{0.5}O_4$ a) and $(LaSr)_2Co_{0.5}Ni_{0.5}O_4$ b).

Table 4.4: Surface area of $(LaSr)_2Co_{0.5}Cu_{0.5}O_4$ and $(LaSr)_2Co_{0.5}Ni_{0.5}O_4$.

Sample	**Surface area [m²/g]**
$(LaSr)_2Co_{0.5}Cu_{0.5}O_4$	7
$(LaSr)_2Co_{0.5}Ni_{0.5}O_4$	6

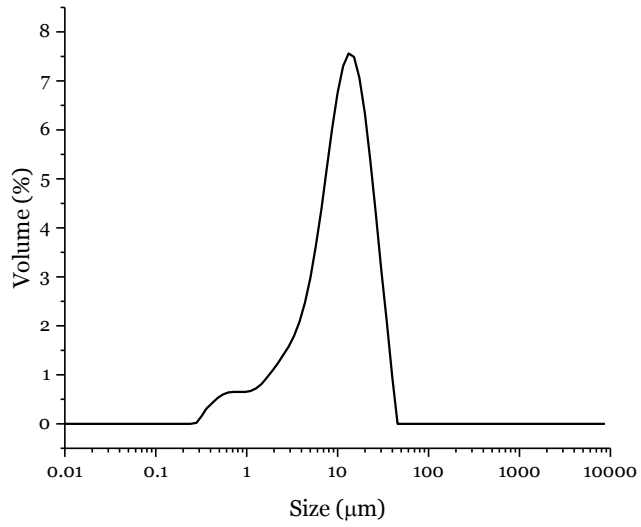

Figure 4.6: Particle size distribution of $(LaSr)_2Co_{0.5}Cu_{0.5}O_4$.

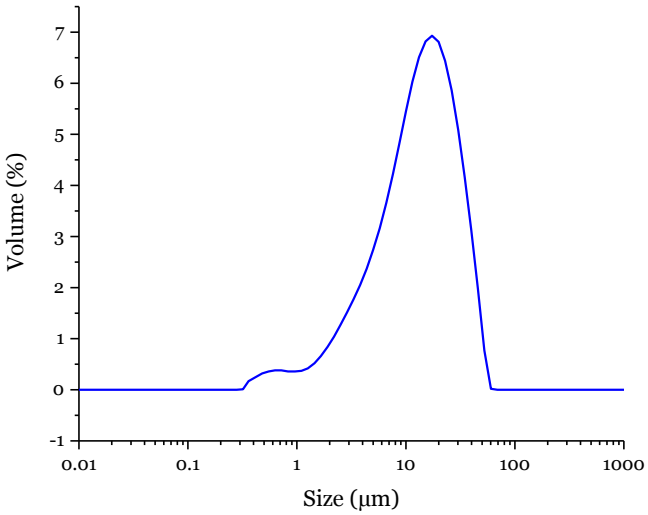

Figure 4.7: Particle size distribution of $(LaSr)_2Co_{0.5}Ni_{0.5}O_4$.

4.5 Surface characterization

The surface investigation was performed by means X-ray photoelectron spectroscopy (XPS) on $(LaSr)_2Co_{0.5}Cu_{0.5}O_4$ and $(LaSr)_2Co_{0.5}Ni_{0.5}O_4$. The XPS spectra and the peak position are reported in figure 4.8 and in table 4.6

respectively. The La 3d 5/2 signals were centred at 834.6-834.9 eV showing the typical shake-up contribution (837.8 eV) of lanthanum (III) in both the samples [160]. The main contribution was positioned at characteristics signal for La $3d_{5/2}$ of perovskites oxides (834.4 eV and 834.7 eV) [103][161]. In $(LaSr)_2Co_{0.5}Ni_{0.5}O_4$ La 3d 5/2 signal appeared wider than $(LaSr)_2Co_{0.5}Cu_{0.5}O_4$ with a less pronounced shake up peak. This is probably due to the presence of oxide and hydroxyl species on its surface (La_2O_3, $La(OH)_3$ and LaOOH respectively at 833.7 eV, 834.6 eV and 834.9 eV) [162][163][164][165][166]. The Sr 3d signal shown a large peak attributed, through fitting procedure, to the presence of two contributions: the strontium of perovskite phase, 132.2 eV, and the $SrCoO_3$, 134.4 eV [160][167][168]. The Co $2p_{3/2}$ values found for both the samples, 780.4 eV and 780.8 eV for $(LaSr)_2Co_{0.5}Cu_{0.5}O_4$ and $(LaSr)_2Co_{0.5}Ni_{0.5}O_4$ respectively, were in agreement with the data reported in literatures for the compounds $La_{1.5}Sr_{0.5}Co_{05}Ni_{0.5}O_4$ and $La_{1.5}Sr_{0.5}Co_{05}Ni_{0.5}O_{3.75}$ (780.2 and 780.5 eV).[169] The fitting procedure on $Co2p_{3/2}$ peak in $(LaSr)_2Co_{0.5}Ni_{0.5}O_4$ suggested also a small presence of Co_3O_4 at 780.7 eV. This seems to agree with the segregation of strontium and lanthanum observed. Several contributions have been found in broad O 1s XPS signals. The typical O 1s signal for perovskite oxides is placed at 529.1 eV but it was not observed in the compounds [21][148]. Instead hydroxyl and carbonate oxygen species were detected on the surface (531.2-531.4-531.8eV) [170][103]. The Cu 2p signal had a binding energy of 933.3 eV which is the characteristic energy for Cu(II) in perovskite structure [21][157]. The oxidation state was also confirmed by the presence of the shake up of Cu(II) at 942.2 eV. The Ni 2p XPS signal was partially overlapped by the XPS signal of $La3d_{3/2}$ resulting in a difficult interpretation. However the peak position, 855.5 eV, and the satellite peak, at 862.6 eV, were attributed to NiO in according with literature [171].

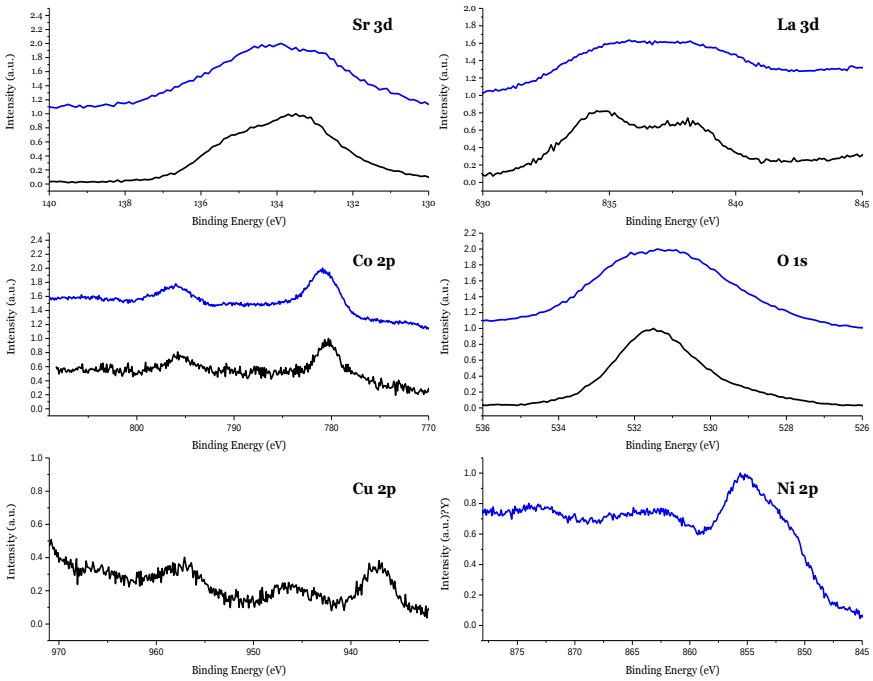

Figure 4.8: XPS spectra obtained for $(LaSr)_2Co_{0.5}Cu_{0.5}O_4$ (black line) and $(LaSr)_2Co_{0.5}Ni_{0.5}O_4$ (blue line)

Table 4.5: XPS peak positions in Binding Energy [eV] for $(LaSr)_2Co_{0.5}Cu_{0.5}O_4$ and $(LaSr)_2Co_{0.5}Ni_{0.5}O_4$.

	La 3d 5/2	**Sr 3d**	**Co 2p**	**Cu 2p**	**Ni 2p**	**O1s**
$(LaSr)_2Co_{0.5}Ni_{0.5}O_4$	834.9 / 837.8	134.6 / 133.4	780.8	-	855.5	531.4
$(LaSr)_2Co_{0.5}Cu_{0.5}O_4$	834.6 / 837.8	134.2 / 133.2	780.4	933.3	-	531.5

Table 4.6: XPS atomic composition for the $(LaSr)_2Co_{0.5}Cu_{0.5}O_4$ and $(LaSr)_2Co_{0.5}Ni_{0.5}O_4$.

Sample		La	Sr	Co	Ni	O	Ni/Co
$(LaSr)_2Co_{0.5}Ni_{0.5}O_4$	Experimental	6	9	12	13	60	
		15	23	30	33	-	1.1
	Nominal	14	14	7	7	57	
		33	33	17	17	-	1.0

Sample		La	Sr	Co	Cu	O	Cu/Co
$(LaSr)_2Co_{0.5}Cu_{0.5}O_4$	Experimental	5	16	4	1	74	
		18	62	15	5	-	0.3
	Nominal	14	14	7	7	57	
		33	33	17	17	-	1.0

The XPS quantitative analysis is displayed in table 4.6. The data shown that both cobalt based perovskites had oxygen over stoichiometry confirming a surface rich of carbonates, oxides and hydroxides. Beside the oxygen amount on the surface, $(LaSr)_2Co_{0.5}Cu_{0.5}O_4$ and $(LaSr)_2Co_{0.5}Ni_{0.5}O_4$ revealed a remarkable difference in cations segregation. The Cu doped sample shown a segregation of A-site cation, strontium, while Ni doped compound displayed the B-site cations segregation, nickel and cobalt. The strontium segregation tendency is well-know and reported in literature [172][173]. Although strontium in $(LaSr)_2Co_{0.5}Ni_{0.5}O_4$ was below the nominal value, it was still above the lanthanum concentration. The remarkable segregation of strontium in $(LaSr)_2Co_{0.5}Cu_{0.5}O_4$ seems to afflict more the copper surface concentration instead the cobalt one. Cobalt in fact shown values close to the nominal one (15% versus 17% of atomic concentration) while copper exposed only 5% respect the cations surface concentration. This appeared more evident looking the surface Cu/Co ratio. It is to notice that the copper surface depletion is often observed in cobalt base perovskites [21][157]. Differently from Cu-doped sample, $(LaSr)_2Co_{0.5}Ni_{0.5}O_4$ had a great cobalt and nickel segregation. Both the cations were almost the double of the nominal values. This together with XRD analysis highlights the difficult in the cobalt substitution with nickel in $(LaSr)_2Co_{0.5}Ni_{0.5}O_4$ compounds.

4.6 Catalytic behaviour

The catalytic reactivity versus carbon monoxide oxidation and methane oxidation was tested in a quartz reactor and the products were detected towards gas-chromatography equipped with TCD. The GHSV used for tests was nearby 100,000 h^{-1}.

4.6.1 Reactivity with CO + O_2

The catalytic behaviour of CO oxidation with stoichiometric amount of O_2 is reported in figure 4.9. The only product detected was carbon dioxide.

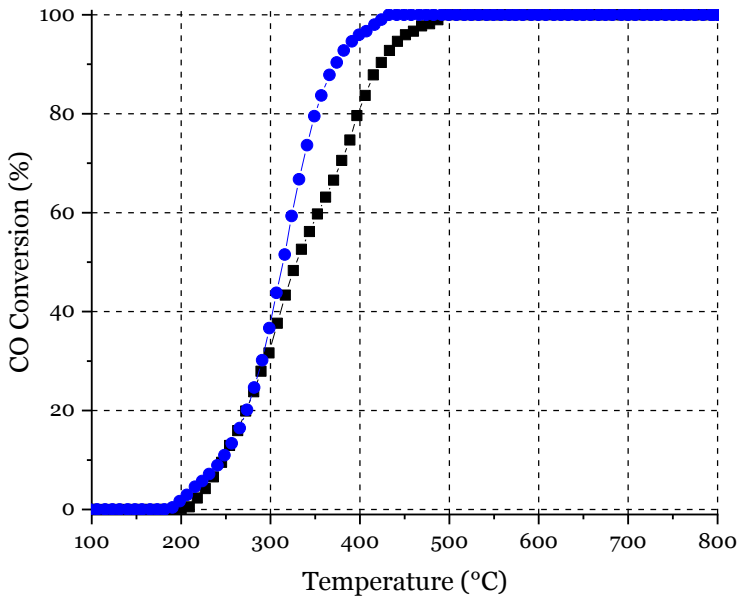

Figure 4.9: CO conversion as a function of temperature for $(LaSr)_2Co_{0.5}Cu_{0.5}O_4$ (black line) and $(LaSr)_2Co_{0.5}Ni_{0.5}O_4$ (blue line).

The well known activity toward oxidation of cobalt based perovskite was confirmed by the tests [21][25][60][157]. As expected the compounds achieved the total CO conversion at 400 °C and 500 °C, respectively for $(LaSr)_2Co_{0.5}Cu_{0.5}O_4$ and $(LaSr)_2Co_{0.5}Ni_{0.5}O_4$, which were values remarkably lower than the typical

intermediate temperature SOFC working condition (600-800 °C). The ignition temperatures for both the samples were around 200 °C. Below 300 °C the CO conversion trend was the same; above 300 °C $(LaSr)_2Co_{0.5}Ni_{0.5}O_4$ boosted its performance achieving the total CO conversion 70°C before $(LaSr)_2Co_{0.5}Cu_{0.5}O_4$. The results obtained were particularly interesting comparing $LaCo_{0.5}Cu_{0.5}O_3$ and $La_{0.5}Sr_{0.5}Co_{0.5}Cu_{0.5}O_3$, prepared with the same procedure (citrate method and calcined at 900 °C), which achieved 10% and 85% of CO conversion at 400 °C respectively [21][157]. To understand the different catalytic behaviour between $(LaSr)_2Co_{0.5}Cu_{0.5}O_4$ and $(LaSr)_2Co_{0.5}Ni_{0.5}O_4$ the atomic surface concentration (XPS analysis) has to be take in account, table 4.6. It has to take in account also the cations surface segregation. The large strontium amount on the $(LaSr)_2Co_{0.5}Cu_{0.5}O_4$ could have affected negatively the performance by covering the active sites. On other hand the great cobalt and nickel segregation, observed on $(LaSr)_2Co_{0.5}Ni_{0.5}O_4$, could instead have increased noteworthy the catalytic activity. The results suggested the great improvement of nickel doping than the copper doping in $(LaSr)_2CoO_4$ perovskite structure for CO oxidation [61].

4.6.2 Reactivity toward methane: direct oxidation of methane

The reactivity towards methane oxidation was explored, figure 4.10, with the purpose to study the catalytic behaviour versus not hydrogen fuels that could be used in solid oxide fuel cell. Both the materials displayed a good activity reaching 75% and 80% of CH_4 conversion for $(LaSr)_2Co_{0.5}Cu_{0.5}O_4$ and $(LaSr)_2Co_{0.5}Ni_{0.5}O_4$, respectively. The materials had an ignition temperature around 450 °C, compatible with what observed in literatures for perovskite based materials [174] [175]. Initially Cu-doped compound had a better CH_4 conversion but above 650 °C it could be observed the inversion of activity. The deactivation observed on

$(LaSr)_2Co_{0.5}Cu_{0.5}O_4$ could be induced by the Cu/Co ratio change during the test. The fresh material was richer in cobalt than copper; however during the reactivity the copper could have segregated inducing a lower activity toward methane. It has to be noticed that in perovskite cobalt is reported to be more active than copper for methane oxidation [176][177].

Over 650 °C the conversion increased as function of the temperature for both the samples.

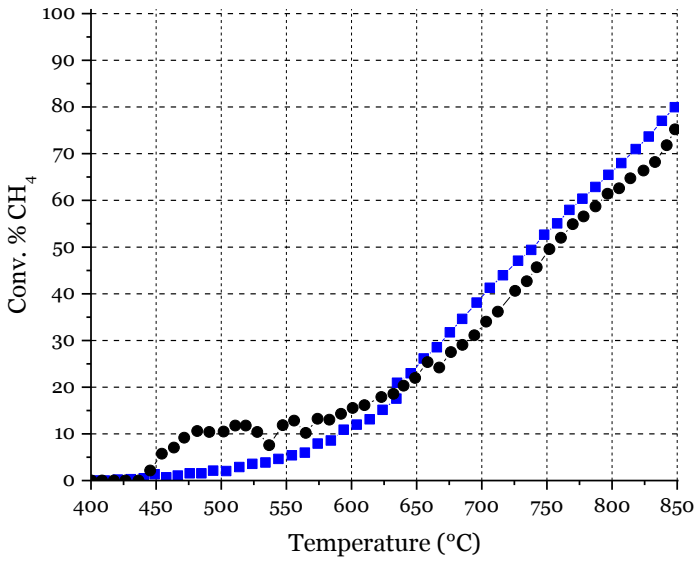

Figure 4.10: 2 $\%CH_4$ + 6 $\%O_2$. $\%CH_4$ Conversion in CH_4+O_2 (stoichiometric) from 400° to 850 °C for $(LaSr)_2Co_{0.5}Cu_{0.5}O_4$ (black line) and $(LaSr)_2Co_{0.5}Ni_{0.5}O_4$ (blue line).

The XRD investigation carried out on the exhausted compounds did not shown structural change, figure 4.11.

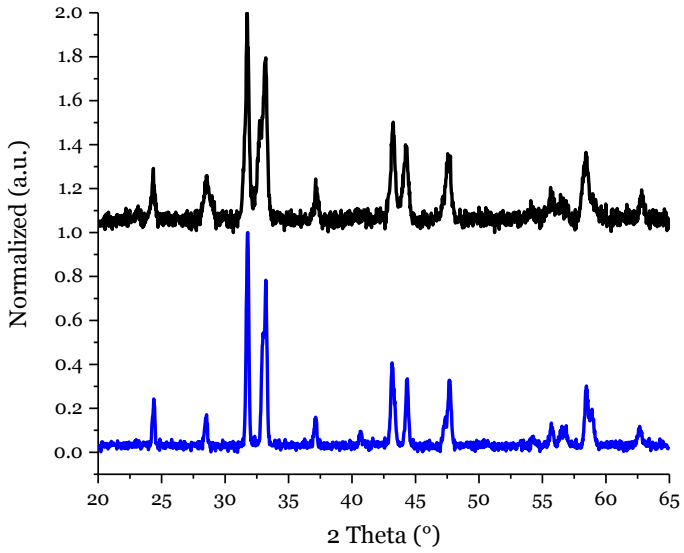

Figure 4.11: XRD pattern of $(LaSr)_2Co_{0.5}Ni_{0.5}O_4$ (blue line) and $(LaSr)_2Co_{0.5}Ni_{0.5}O_4$ exhaust (black line).

4.7 Electrochemical investigations

In order to study the materials prepared as electrodes for symmetric solid oxide fuel cell at intermediate temperatures (600-800 °C), the electrochemical investigation was carried out on $(LaSr)_2Co_{0.5}Ni_{0.5}O_4$ and $(LaSr)_2Co_{0.5}Cu_{0.5}O_4$. During the investigation the chemical reactivity and the mechanical incompatibility between $(LaSr)_2Co_{0.5}Cu_{0.5}O_4$ and gadolinium doped ceria has been found (paragraph 4.7.2). Therefore only Ni-doped compound was characterized by means electrochemical impedance spectroscopy (EIS) under air and under methane.

4.7.1 Compatibility between Electrodes and Electrolytes powders

To investigate the chemical compatibility, the X-ray diffraction (XRD) technique was used. The electrodes and electrolytes were mixed and grinded together in a

mortar. The mixed powders were finally fired at high temperature under the same conditions selected for symmetric SOFC preparation, table 4.7.

Table 4.7: Condition used for electrodes/electrolytes compatibility.

Sample	Electrolyte	Conditions
$(LaSr)_2Co_{0.5}Cu_{0.5}O_4$	GDC	1200 °C; under air; 1 hour
$(LaSr)_2Co_{0.5}Ni_{0.5}O_4$	GDC	1200 °C; under air; 1 hour

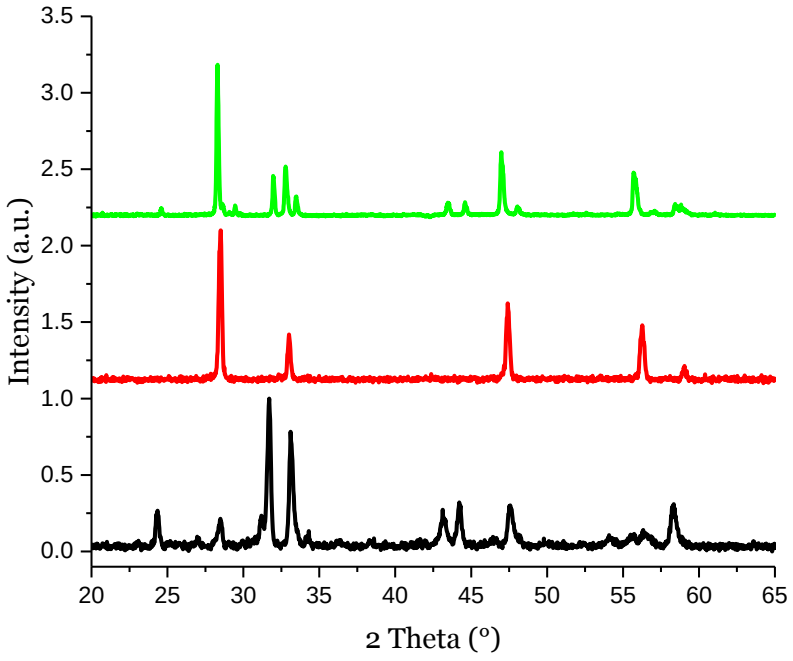

Figure 4.12: XRD patterns of $(LaSr)_2Co_{0.5}Cu_{0.5}O_4$ (black line), GDC (red line), $(LaSr)_2Co_{0.5}Cu_{0.5}O_4$ + GDC calcined at 1200 °C (green line).

The figure 4.11 displayed the results on compatibility between $(LaSr)_2Co_{0.5}Cu_{0.5}O_4$ and GDC powders. The XRD pattern did not show the formation of secondary phases. It could be noted only a shift to lower angle of GDC peaks after the thermal treatments at 1200 °C. This was induced by the expansion of GDC lattice

as confirmed also by literature [178]. For this reason the symmetric cells $(LaSr)_2Co_{0.5}Cu_{0.5}O_4$/GDC/$(LaSr)_2Co_{0.5}Cu_{0.5}O_4$ have been prepared.

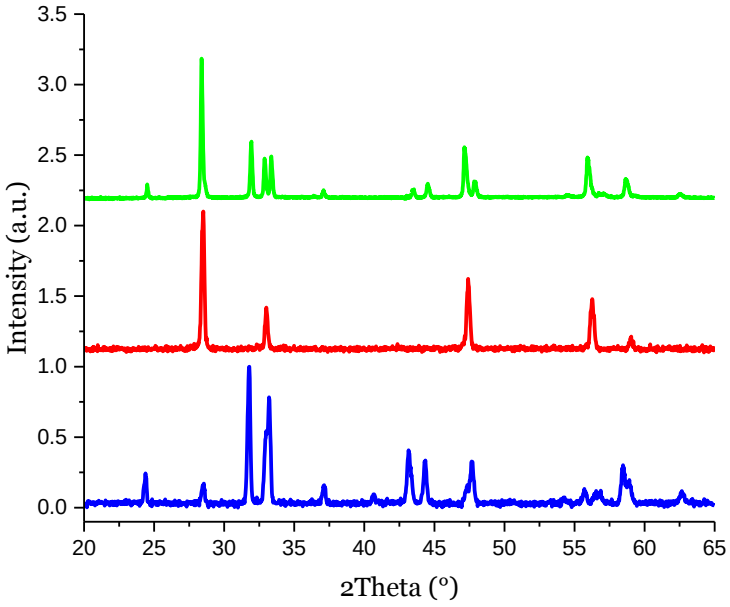

Figure 4.13: patterns of $(LaSr)_2Co_{0.5}Ni_{0.5}O_4$ (blue line), GDC (red line), $(LaSr)_2Co_{0.5}Ni_{0.5}O_4$ + GDC calcined at 1200 °C (green line).

The XRD pattern obtained after the annealing a 1200 °C under air is reported in figure 4.12. As in the previous sample, no secondary phases were detected and only a small shift to lower angle of GDC peaks was observed.

With the purpose of testing the materials under H_2 and CH_4 environment, symmetric cells with material/GDC/material were prepared and treated at 850 °C under hydrogen and methane for 1h. After the thermal treatment under hydrogen both $(LaSr)_2Co_{0.5}Ni_{0.5}O_4$ and $(LaSr)_2Co_{0.5}Cu_{0.5}O_4$ lost their adhesion with the GDC electrolyte resulting in the impossibility of further tests. The thermal treatments under methane for both the electrodes did not induce the electrodes breaking suggesting the compatibility towards methane.

4.7.2 Symmetric cell preparation: pellet, ink, adhesion

With the aim of performing the electrochemical characterization symmetric cells were prepared. This particular configuration allows to study the processes of the desired electrode while keeping both the electrodes in contact with the same environment (this allows to deeply understand the behaviour of the electrode). The impedance analyses were executed on electrolyte supported button cells: electrode/electrolyte/electrode. The steps involved in the cell assembly were: the pellet preparation, the ink formulation and printing, the electrodes adhesion and the infiltration phase. The detailed procedures were exposed in chapter 3. The summery of parameters used for the preparation of electrolyte, ink and the adhesion treatment are reported below (table 4.8, table 4.9 and figure 4.14).

Table 4.8: Condition used electrolytes preparation

Electrolyte	Mass [g]	Diameter [mm]	Pressing	Thermal treatment	Density
GDC	2.5	20	190 Bar, 30s	Air 1500°C, 5h, 2°C/min	95-96%

Table 4.9: Recipe used for ink preparation

% m/m	Electrode
Electrode	44
Dispersant (Terpineol)	14
Binder (ethyl cellulose)	2
Solvant (Dupont)	50

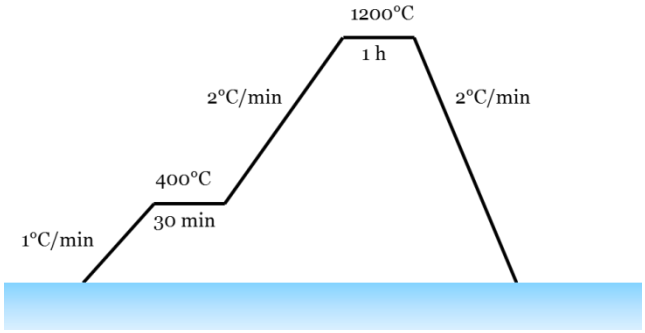

Figure 4.14: Thermal treatment used for electrode adhesion.

The final treatment consisted in a very slow heating rate up to 400 °C with the purpose of burning the organic compounds of the ink, followed by a slow heating rate up to the final thermal treatment (sintering and adhesion) under air. Two temperatures were explored: 1000 °C and 1200 °C. At 1000 °C the electrodes did not show a good adhesion resulting in the detaching of layers by simple using the fingers. This behaviour was observed also in literatures on $(LaSr)_2CoO_4$ [24]. Instead 1200 °C allowed a good adhesion not showing detaching using a scotch tape. The morphology of symmetric cells prepared was investigated by SEM, figure 4.15.

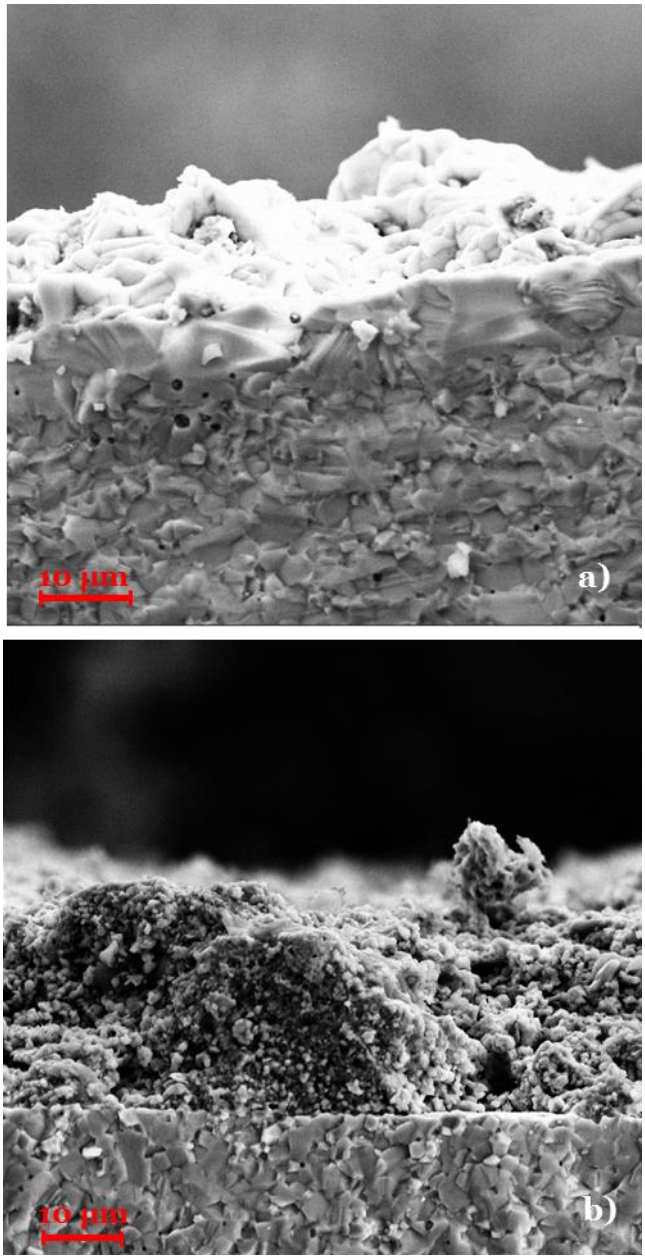

Figure 4.15: SEM images of $(LaSr)_2Co_{0.5}Cu_{0.5}O_4$ a) and $(LaSr)_2Co_{0.5}Ni_{0.5}O_4$ b).

The thickness of the final electrode layer was around 30 µm for the $(LaSr)_2Co_{0.5}Ni_{0.5}O_4$ and between 10 and 15 µm for $(LaSr)_2Co_{0.}Cu_{0.5}O_4$. The SEM images showed also a different porosity for the two cells prepared. $(LaSr)_2Co_{0.5}Ni_{0.5}O_4$ had a good porosity with clearly visible holes. $(LaSr)_2Co_{0.}Cu_{0.5}O_4$, in contrast, displayed a compact structure without a good homogeneity deposition on the electrolyte. Moreover during the sample preparation it was observed the penetration of $(LaSr)_2Co_{0.5}Cu_{0.5}O_4$ through the

GDC electrolyte suggesting a sort of reactivity (not observed during the XRD investigation on powders).

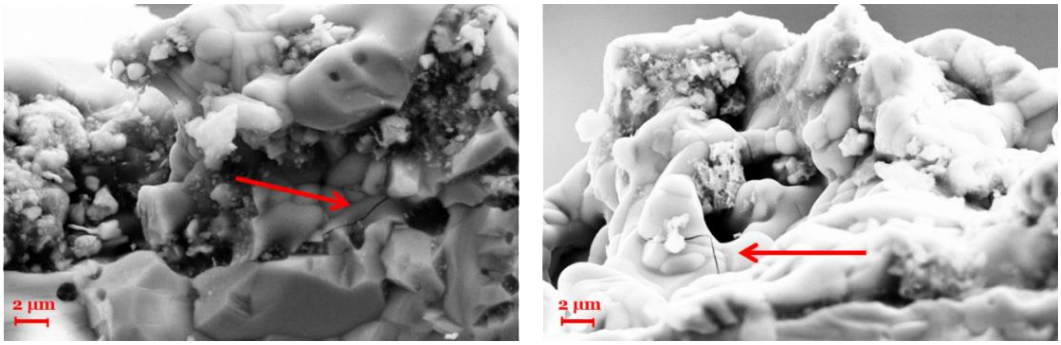

Figure 4.16: SEM images of $(LaSr)_2Co_{0.5}Cu_{0.5}O_4$ electrode breakage on GDC calcined at 1200 °C.

Focusing on the $(LaSr)_2Co_{0.5}Cu_{0.5}O_4$ electrode structure, figure 4.16, it was possible to observe the thermal expansion incompatibility between $(LaSr)_2Co_{0.5}Cu_{0.5}O_4$ and GDC10 with the formation of several cracks on the electrode. This behaviour was not observed for $(LaSr)_2Co_{0.5}Ni_{0.5}O_4$ which seemed to display a good mechanical compatibility, figure 4.17. Since the structure (K_2NiF_4) and the dopant loading were the same in both the samples, the incompatibility had to be related to copper in the Ruddlesden and Popper structure. In fact this chemical and mechanical incompatibility was not observed on $LaCo_{0.5}Cu_{0.5}O_3$ and $La_{0.5}Sr_{0.5}Co_{0.5}Cu_{0.5}O_3$ with GDC [22]. The thermal expansion mismatch observed of $(LaSr)_2Co_{0.5}Cu_{0.5}O_4$ with $Ce_{0.90}Gd_{0.10}O_{2-\delta}$ seemed to be in according with literature data for Cu-based Ruddlesden and Popper structure [24][179].

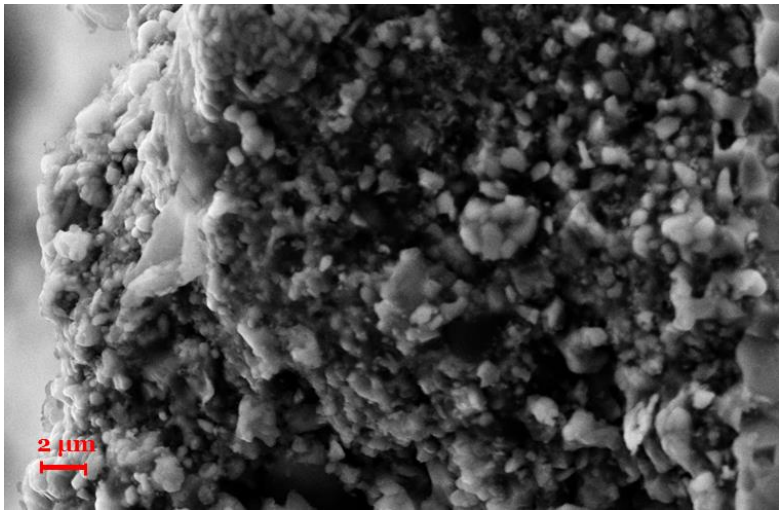

Figure 4.17: SEM images of $(LaSr)_2Co_{0.}Ni_{0.5}O_4$ electrode calcined at 1200 °C.

Although the good catalytic activity, the chemical and mechanical incompatibility of $(LaSr)_2Co_{0.5}Cu_{0.5}O_4$ versus the electrolyte, points out the impossibility to use this material as electrode on SOFC with a GDC as electrolyte.

4.8 Impedance analysis

Impedance spectroscopy is one of the main techniques for SOFC materials characterization and evaluation of electrochemical performance. It is highly sensitive toward sample configuration and fabrication but allow to investigate the polarization processes of the material.

The electrochemical measurements (EIS) were performed in a homemade device using a PGSTAT 302 Autolab Frequency Response Analyser.[134] The symmetric cell was placed between two gold grids and pressed with a mechanical load. The measurements were carried out at steady state condition (zero DC current) in the frequency range of 10^{-2}-10^{6} Hz and with signal amplitude of 50mV. The temperature range explored was from 850 °C to 500 °C with 5 °C/min cooling rate. The cell was kept under stationary air (cathode investigation) and under

constant flow of 100mL/min of 5% CH_4 in argon (anode investigation) and the impedance spectra were collected after one hour.

4.8.1 Cathode investigation

Impedance spectra were collected on symmetric cells $(LaSr)_2Co_{0.}Ni_{0.5}O_4/GDC/(LaSr)_2Co_{0.}Ni_{0.5}O_4$, in figure 4.18 an example of impedance spectra is reported. The electrolyte resistance (R_s) represents the contribution of bulk diffusion and inter grain diffusion on the electrolyte. It depends on the type, the thickness and the preparation history of the electrolyte. In order to have an easily understanding of the Nyquist plot, R_s (detailed chapter 3) was subtracted from figure 4.18.

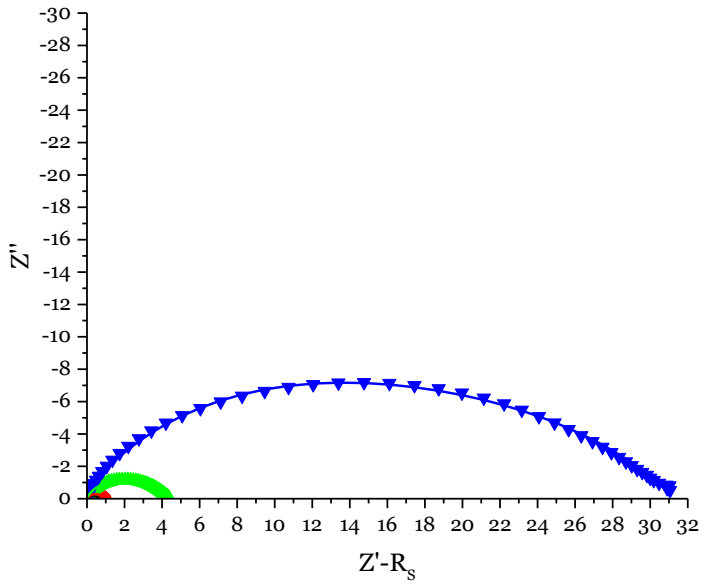

Figure 4.18: Nyquist plots of $(LaSr)_2Co_{0.}Ni_{0.5}O_4/GDC/(LaSr)_2Co_{0.}Ni_{0.5}O_4$ under air at 830 °C (black line), 800 °C (red line), 700 °C (green line) and 599 °C (blue line).

The spectra collected allow to extrapolate the area specific resistance (ASR) for each temperature studied. The ASR evolution versus the temperature for

$(LaSr)_2Co_0.Ni_{0.5}O_4$ is reported in figure 4.18. The ASR showed linear decrease as function of the temperature, confirming the thermal activation of the electrodes. The ASR value achieved at 700 °C was 2.51 Ω cm² which is too high for a SOFC application (under 1 Ω cm²) but similar for $(LaSr)_2CoO_4$ types compounds (>2 Ω cm²) and $La_{2-x}Sr_xCo_{0.5}Ni_{0.5}O_4$ (1.92 Ω·cm²) at the same temperature [24][97]. Moving at higher temperatures the ASR greatly decrease reaching 0.56 Ω cm² at 800 °C. The lowest ASR was obtained at 830 °C $(LaSr)_2Co_{0.5}Ni_{0.5}O_4$ achieving the value of 0.36 Ω cm² which is considerably close to the resistance suggested for a SOFC application, 0.15 Ω cm² [180].

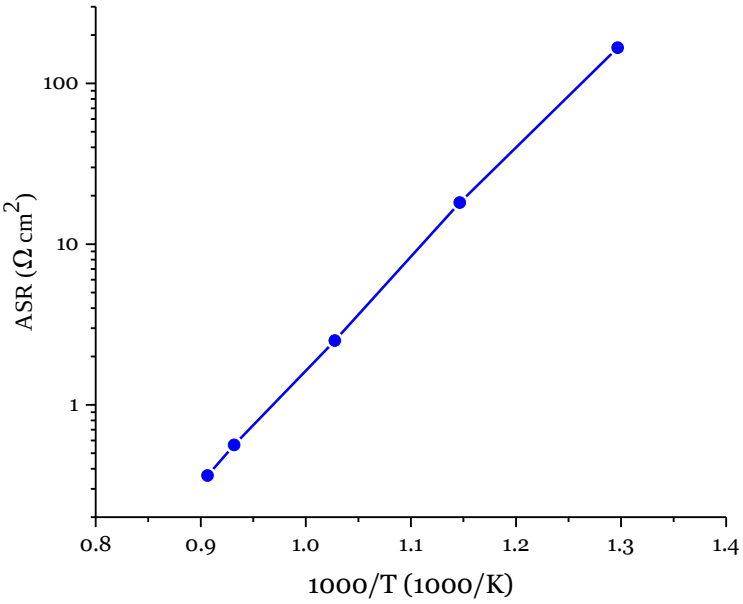

Figure 4.19: The area specific resistance (ASR) Arrhenius plot for $(LaSr)_2Co_{0.5}Ni_{0.5}O_4$.

The Arrhenius plot of ASR allowed to calculate the overall activation energy, which is directly linked with the O_2 gas diffusion, electrode reactions and interphase ionic transfer for the electrode, by the use of the equation eq. 3.3.

The activation energy obtained for $(LaSr)_2Co_{0.5}Ni_{0.5}O_4$ was 1.42 eV (figure 4.20), which is very close to the $(LaSr)_2CoO_4$ reported in literature (1.40 eV) [181].

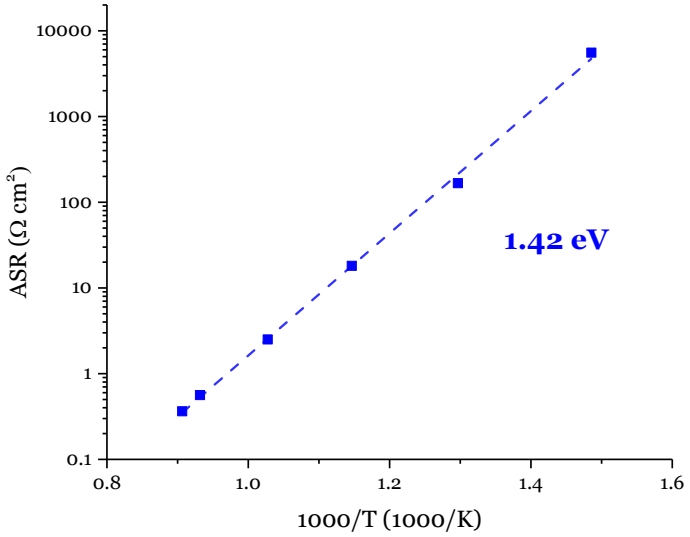

Figure 4.20: Fitting of ASR values as function of temperature for $(LaSr)_2Co_{0.}Ni_{0.5}O_4$ under air and its activation energy.

With the purpose to understand which processes were involved in the polarization loss the impedance spectra were fitted and starting from the data collected it was possible to propose the equivalent circuits for the systems studied. In figure 4.21 is reported the equivalent circuit proposed for $(LaSr)_2Co_{0.5}Ni_{0.5}O_4$ under stationary air, while in figure 4.22 the fitting graph are reported.

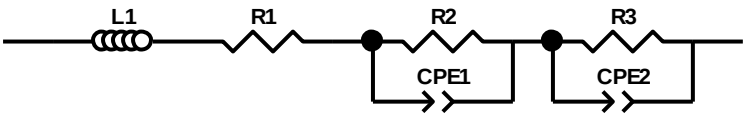

Figure 4.21: The equivalent circuit used to fitting the electrochemical impedance spectra under stationary air used at 599 °C, 700 °C, 800 °C and 830 °C.

The equivalents circuits, thought the equation in chapter 3 (eq. 3.4), allowed to calculate the capacitance of each contributions, C_e and so to distinguish the processes. The EIS spectra and the equivalent circuit proposed seem in according with literature for $(LaSr)CoO_4$ [24][141][181].

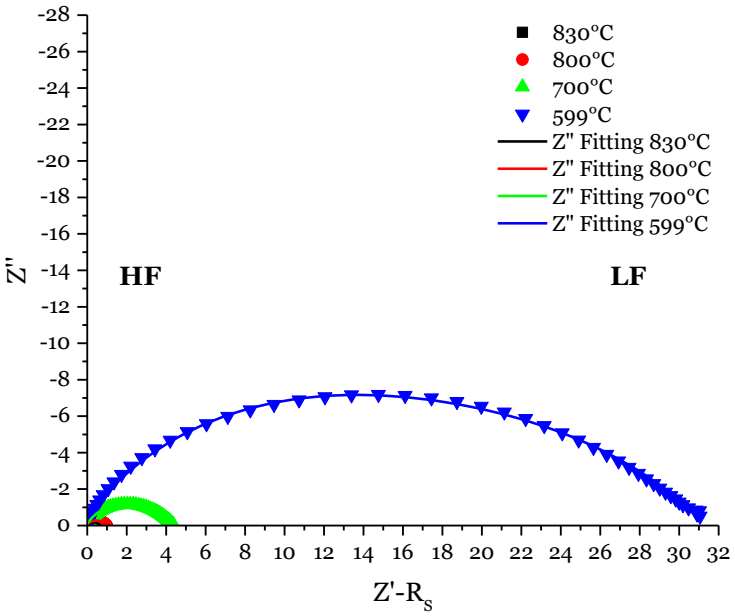

Figure 4.22: Nyquist plots of $(LaSr)_2Co_{0.}Ni_{0.5}O_4$ at 599 °C (blue), 700 °C (green), 800 °C (red) and 830 °C (black) under stationary air. Dots are the experiment data and lines are the fitting used for the analysis. High frequencies (HF), Low frequencies (LF).

The EIS spectra and the capacitances analysed suggested two contributions associated to the charge oxygen ion transfer at the interface electrode/electrolyte (high frequency) and the reaction processes, oxygen adsorption and dissociation, on the electrode surface (low frequency) [181]. The capacitances, figure 4.23, did not show large variation as a function of temperatures, suggesting that the involved processes remain almost the same in the temperatures investigated. This is in according with the data observed in literatures for highly doped Co-based perovskite [22][141].

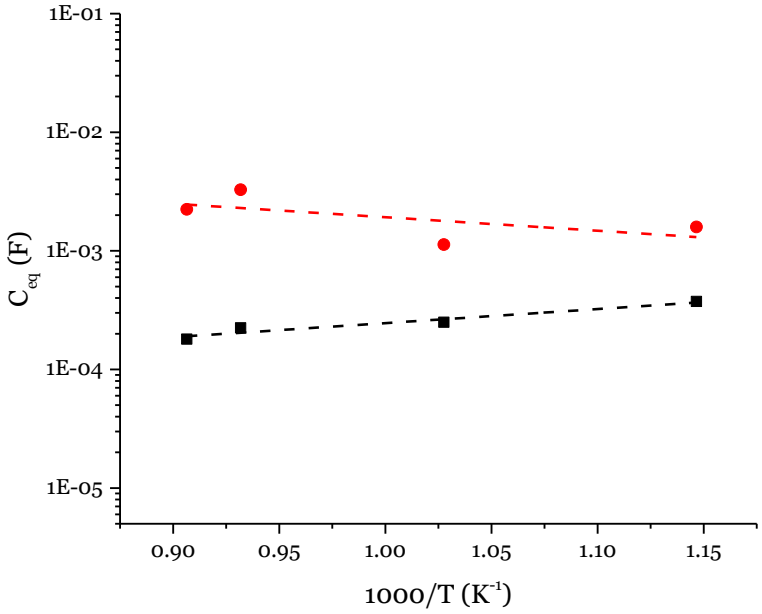

Figure 4.23: Arrhenius plot of the capacitances for $(LaSr)_2Co_{0.}Ni_{0.5}O_4$.

Although the ASR value obtained at 700 °C was still too high comparing the benchmark for a real application, the morphology optimization had still to be carried out [180]. This could enhance significantly the electrode performance [100]. Moreover, in according with what observed in literature for $(LaSr)_2CoO_4$, a composite $(LaSr)_2Co_{0.5}Ni_{0.5}O_4$-GDC could greatly boost the performance by increasing the transport oxygen ions [24][181][182].

4.8.2 Anode Investigation

Impedance spectra were collected on symmetric cells $(LaSr)_2Co_{0.}Ni_{0.5}O_4$/GDC/$(LaSr)_2Co_{0.}Ni_{0.5}O_4$, under constant flow of 100mL/min dry CH_4 5%/Ar. In order to have an easily understanding of the Nyquist plot, R_s (detailed chapter 3) was subtracted from the impedance spectra.

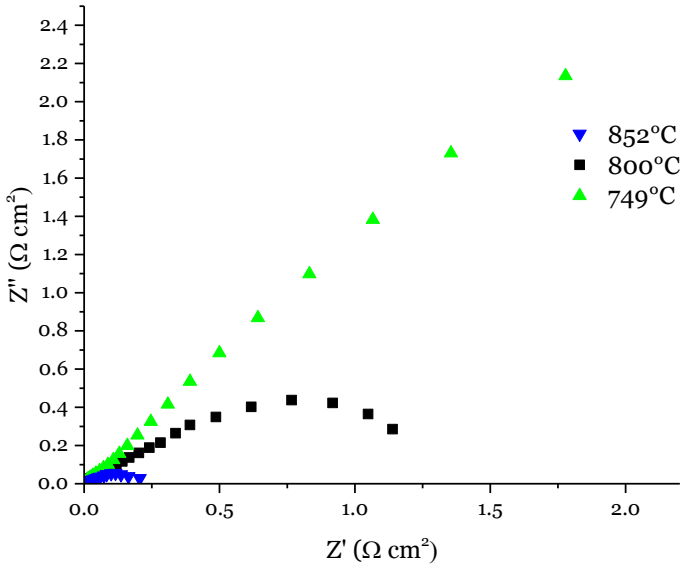

Figure 4.24: Nyquist plots of $(LaSr)_2Co_{0.}Ni_{0.5}O_4$/GDC/$(LaSr)_2Co_{0.}Ni_{0.5}O_4$ under methane at 852 °C (blue), 800 °C (black) and 749 °C (green).

The data collected allow to obtain the area specific resistance (ASR) as a function of the temperature. The ASR evolution versus the temperature for $(LaSr)_2Co_{0.5}Ni_{0.5}O_4$ is reported in figure 4.25. The ASR observed at 700 °C was very large, 290.2 Ω cm², but rapidly decrease by increasing the temperature, achieving 0.94 Ω cm² at 800 °C. Although it was not possible to obtain the ASR under hydrogen due to the instability (TPR analysis), the ASR observed under methane shown a remarkable low resistance especially compared to what reported in literature on $La_4Sr_8Ti_{11}MnO_{38-\delta}$ at 950 °C (0.7 Ω cm²) and the composite $La_{0.4}Ce_{0.6}O_{1.8}$–$La_{0.4}Sr_{0.6}TiO_3$ which displayed an ASR of 78.35 Ω cm² at 800 °C [183][184]. The lowest values observed on $(LaSr)_2Co_{0.}Ni_{0.5}O_4$ was 0.14 Ω m² at 850 °C (the maximum temperature reachable by our system) but above the intermediate temperatures (600 °C-800 °C) and the typical working condition of GDC electrolyte [185]. At temperature close to 800 °C the GDC electrolyte gains

electronic conduction characteristic which lead to a decrease of total performance (electron leakage).

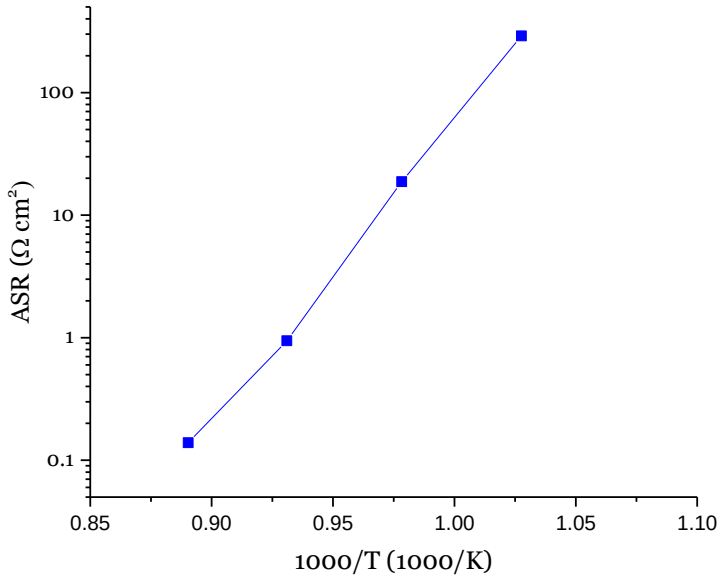

Figure 4.25: The area specific resistance (ASR) Arrhenius plot for $(LaSr)_2Co_{0.}Ni_{0.5}O_4$ under methane.

The activation energy found for $(LaSr)_2Co_{0.5}Ni_{0.5}O_4$ in methane was 4.87 eV, figure 4.26. It was larger than the typical values under hydrogen environment and the value reported for $La_4Sr_8Ti_{11}MnO3_{8-\delta}$ (1.9 eV) under methane [183].The activation energy is directly correlated with all the processes that occur on the electrode. The large E_a observed was probably related at the high activation energy required to activate the methane fuel.

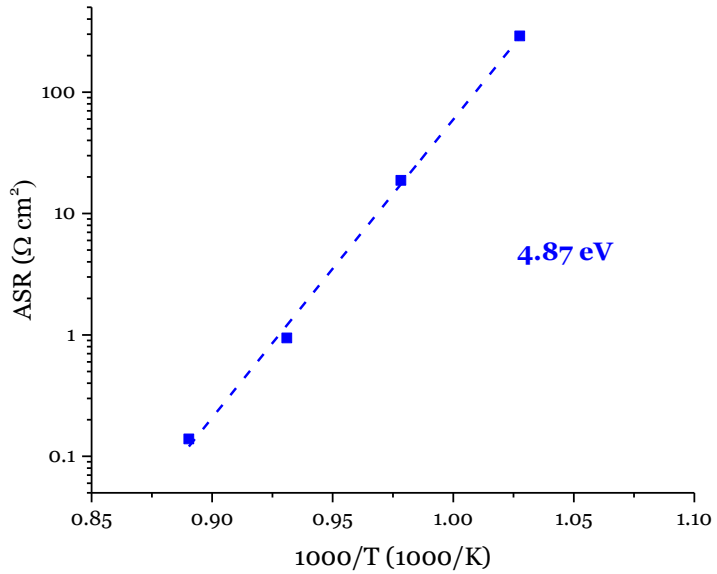

Figure 4.26: Fitting of ASR values as function of temperature for $(LaSr)_2Co_{0.}Ni_{0.5}O_4$ under methane and its activation energy.

The better equivalent circuit that fitted the impedance spectra collected is reported below, figure 4.27 and the fit curves in figure 4.28.

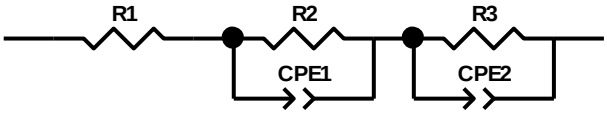

Figure 4.27: The equivalent circuit used to fitting the electrochemical impedance spectra under methane atmosphere (% CH_4 /Ar).

The proposed equivalent circuit suggest two contributions, one large related to the reaction processes on the surface and another related to the interface process between the electrode/electrolyte. The large contribution induced by the reaction surface was expected taking in account the stability of methane molecule and the high activation energy observed (4.87 eV) compared with activation energy found under air.

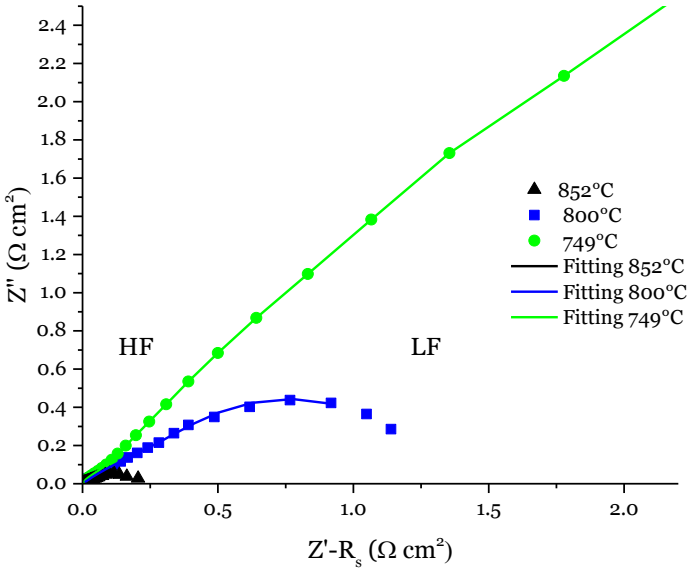

Figure 4.28: Nyquist plots of $(LaSr)_2Co_{0.5}Ni_{0.5}O_4$ at 852 °C (black), 800 °C (blue) and 749 °C (green) under methane (5%CH_4/Ar). Dots are the experiment data and lines are the fitting used for the analysis. High frequencies (HF), Low frequencies (LF).

Although $(LaSr)_2Co_{0.5}Ni_{0.5}O_4$ shown a considerable high ASR under methane (290.2 Ω m²) and under stationary air (2.51 Ω m²) at 700 °C, at higher temperature (800 °C) the electrode achieved remarkable results shown promising ASR values (0.94 Ω m² under methane vs 0.56 Ω m² under air).

4.9 Chapter conclusions

In this study $(LaSr)_2Co_{0.5}Cu_{0.5}O_4$ and $(LaSr)_2Co_{0.5}Ni_{0.5}O_4$ were investigated as electrodes for symmetric solid oxide fuel cell feed directly with methane. Co-based perovskites have been chosen due to their excellent catalytic activity towards oxidation and their proved good performance as cathode in SOFC [22][25][60].

The materials were prepared by means of citrate method followed by a thermal treatment under air at 900 °C. The synthesis procedure has allowed to obtain a

good crystalline grade however trace of secondary phases were detected in both the materials. $(LaSr)_2Co_{0.5}Cu_{0.5}O_4$ have shown the segregation of the mixed ionic-electronic conducting phase $La_2Co_{0.75}Cu_{0.25}O_4$ which was supposed to not affect negatively the electrochemical proprieties of investigated compounds. Particularly interesting was the Cu/Co (1:3) ratio calculated though the XPS quantity analysis which suggested presence of $La_2Co_{0.75}Cu_{0.25}O_4$ mainly on the surface. The $La_2Co_{0.75}Cu_{0.25}O_4$ formation could also have led to the large strontium segregation observed at XPS. The XPS analysis of strontium revealed in fact a concentration more than double of nominal value with the Sr 3d XPS signal attributed to the perovskite and to $SrCO_3$. The presence of high amount of carbonates species on surface could have partially affected the catalytic activity of $La_2Co_{0.75}Cu_{0.25}O_4$.

$(LaSr)_2Co_{0.5}Ni_{0.5}O_4$ instead has shown a small segregation of NiO visible though XRD and XPS. The XPS analysis has revealed that nickel segregation was coupled with cobalt one suggesting the difficulty of cobalt substitution with nickel on $(LaSr)_2Co_{0.5}Ni_{0.5}O_4$ with the synthesis used. However the catalytic and the electrochemical behaviours seem not to be affected by the NiO presence.

Despite the low surface area, 7 and 6 m^2/g, and the high d(0.5), 11.8 μm and 14.5 μm, for $(LaSr)_2Co_{0.5}Cu_{0.5}O_4$ and $(LaSr)_2Co_{0.5}Ni_{0.5}O_4$ respectively; both the samples have shown a good catalytic activity towards CO oxidation and methane oxidation. The total CO conversion was reached below 500 °C and with an ignition temperature of 200 °C. While the CH_4 conversion was 75% and 80% for $(LaSr)_2Co_{0.5}Cu_{0.5}O_4$ and $(LaSr)_2Co_{0.5}Ni_{0.5}O_4$ respectively at 800 °C. The ignition temperatures were around 450 °C which is in according with the literatures data for perovskite base materials [174][175]. Cu-doped compound shown a higher CH_4 conversion below 650 °C but above that the Ni-doped cobaltate boosted its

performance overtaking $(LaSr)_2Co_{0.5}Cu_{0.5}O_4$. The XRD carried out after the methane oxidation reaction on exhausted $(LaSr)_2Co_{0.5}Ni_{0.5}O_4$ confirmed the structure stability after reactivity test.

The chemical and mechanical compatibility were investigated by XRD and SEM analysis on $(LaSr)_2Co_{0.5}Cu_{0.5}O_4$ and $(LaSr)_2Co_{0.5}Ni_{0.5}O_4$ versus gadolinium doped ceria. The XRD patterns performed on mixed powders (compound/electrolyte) at 1200 °C under air did not show any structural change; however the SEM investigation revealed the chemical and mechanical incompatibility of $(LaSr)_2Co_{0.5}Cu_{0.5}O_4$ towards GDC. $(LaSr)_2Co_{0.5}Cu_{0.5}O_4$ in fact was penetrated through the electrolyte inducing colour changing. Moreover focussing on the SEM images of $(LaSr)_2Co_{0.5}Cu_{0.5}O_4$/GDC was possible to observe the breakage of electrode structure after the adhesion treatment. $(LaSr)_2Co_{0.5}Ni_{0.5}O_4$ displayed chemical and mechanical compatibility with GDC and for this reason was tested under air (cathode) and under methane (anode). The test under hydrogen was not possible due its instability under hydrogen at high temperatures observed with TPR analysis.

The symmetric cells $(LaSr)_2Co_{0.5}Ni_{0.5}O_4$/GDC/$(LaSr)_2Co_{0.5}Ni_{0.5}O_4$ tested under stationary air achieved an area specific resistance (ASR) of 2.51 Ω cm² at 700 °C which was similar to $(LaSr)_2CoO_4$ (>2 Ω cm²) and $La_{2-x}Sr_xCo_{0.5}Ni_{0.5}O_4$ (1.92 Ω cm²) reported in literature [24][97]. At higher temperatures (800 °C) the ASR decrease reaching 0.56 Ω cm² which is significantly close to the resistance suggested for a SOFC application, 0.15 Ω cm² [180]. The ASR calculated at 700 °C under methane was two magnitude of order larger than under air, 290.2 Ω cm², confirming the high activation energy required for methane utilization. However at 800 °C the ASR dropped to 0.94 Ω m² which is an noteworthy value especially taking in account the ASR reported in literature for perovskite based compounds

such as $La_4Sr_8Ti_{11}MnO_{3-\delta}$ (0.7 Ω cm² at 950 °C) and the composite $La_{0.4}Ce_{0.6}O_{1.8}$–$La_{0.4}Sr_{0.6}TiO_3$ (78.35 Ω cm² at 800 °C) [183][184].

The good catalytic and electro-catalytic performances observed on $(LaSr)_2Co_{0.5}Ni_{0.5}O_4$, confirm the feasibility to use $(LaSr)_2Co_{0.5}Ni_{0.5}O_4$ as electrode on symmetric solid oxide fuel cell feed directly with methane. The results appeared even more promising taking in account the great performance improvement that could be obtained with a morphology optimization and by preparing a composite with the electrolyte powder [24][100][181][182].

Chapter 5

5.1 Introduction to Chapter 5

The experiments conducted at ESRF were devoted to the study of the reversible structural properties of selected perovskite-type oxides toward redox pulsing as a function of temperature. This behaviour is closely related to catalytic properties. The high penetrating energy and small scattering angles of the high energy X-ray diffraction (HE-XRD) allow to follow the structural changes during the chemical reactions. In this chapter the summarized results collected during the PhD period are reported.

5.2 The Synchrotron

The synchrotron is a powerful and useful source of X-ray. These particular emitted photons are produced by electrons moving at speed close to speed of light.

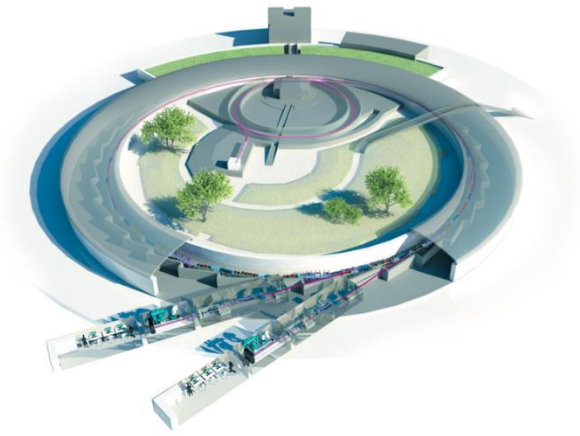

Figure 5.1: ESRF synchrotron image [186].

The ESRF synchrotron is composed by different component, figure 5.1:

- the main ring is where the electrons spend most of their time. In particular, the ESRF's ring is 844 m long and kept at 10^{-9} mbar of pressure, to preserve the electron's mean free path;
- the electrons are produced in a linear accelerator (LINAC) by the thermionic effect of a cathode. A grill is used for compact the electrons in bunches before injects they in the booster;
- Before the main ring, the electrons are accelerated by a booster to 6 GeV, a ring of 300 m circumference. The injection is performed at regular intervals in order to provide a stable intensity to the beam lines. During the travelling, energy lost by light emission is restored by means of radiofrequency cavities

The storage ring at ESRF consists of 32 straight and 32 curved sections. Inside it, couples of large bending magnets placed along the path in correspondence of the curved segments cause the deviation of the beam by applying a magnetic field. These devices are able to produce the emission of a broad continuum spectrum from microwaves to hard X-rays, but with a limitation in terms of beam focusing. In contrast, the insertion devices overcome this restriction providing higher intensity and focusing of the beam. On type of insertion device is the undulator: is made by a define number of permanent magnets periodically organized with opposite polarity, show in figure 5.2.

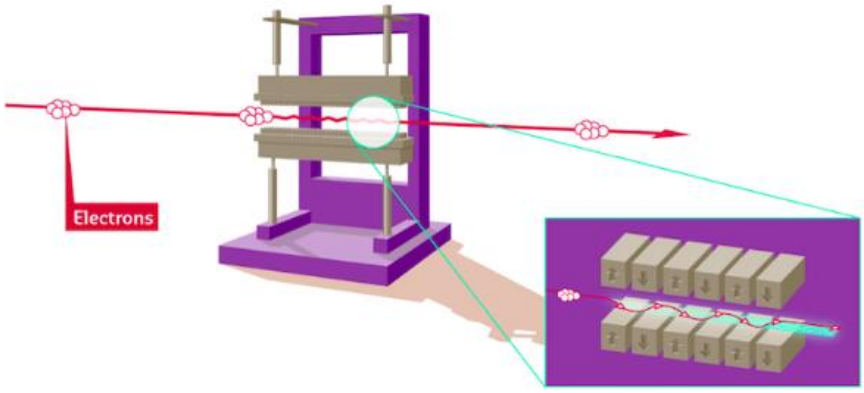

Figure 5.2: representation undulator [186].

5.3 The beamline: ID 15

The ID15 beamline is dedicated to experiments that need very high energy X-ray. The energy interval is from 20 keV to 120 keV end the beam can be focused to a minimum of 1x1 micrometers up to 8x8 mm. The geometry of the analysis is in transmission, show in figure 5.3.

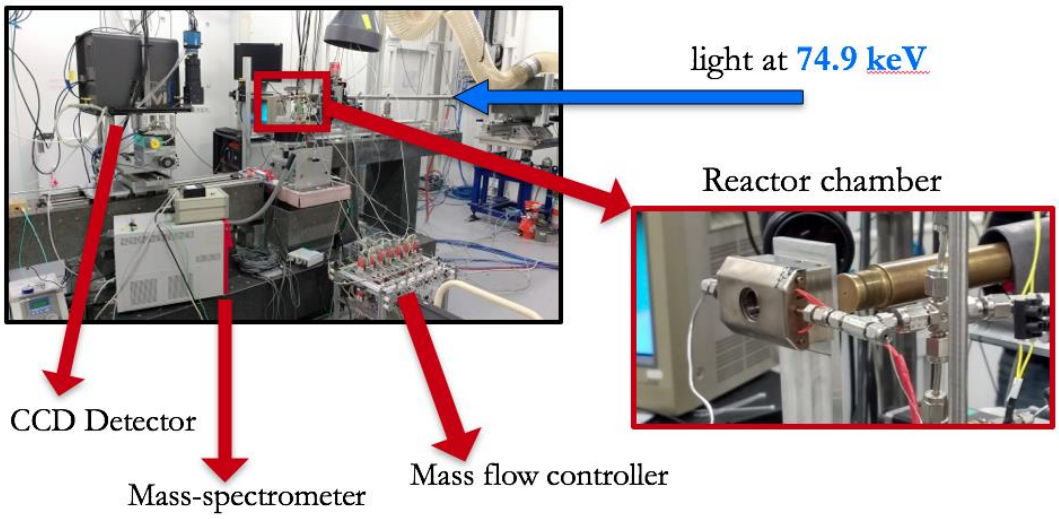

Figure 5.3: Measurement system used at the ID15 beamline.

The equipment used consist in:

- detector DETECTRIS Pilatus3X CdTe 2M,

- mass spectrometer Omnistar Pfeiffer,
- mass flow controller,
- reactor chamber

The chamber, design at the Paul Sherrer Institut, can reach the temperature of 400-450 °C. In figure 5.4 is show an explode.

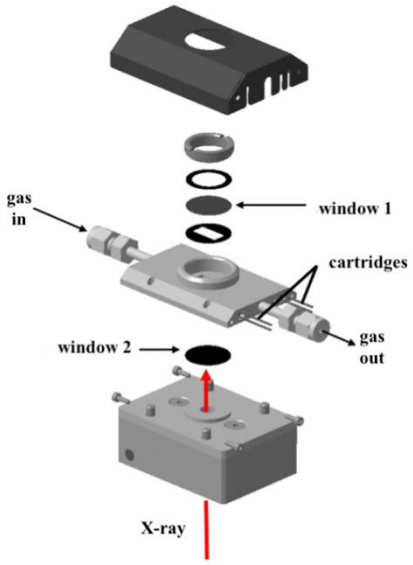

Figure 5.4 Diagram of the system used.

The reactor chamber is made of stainless steel, useful for very fast temperature ramp and not fragile. The powder sample can be arranged in a rectangular aperture where is maintained in position by two carbon windows: is used the carbon for its mostly transparency at the X-ray beam.

The temperature is monitored thanks to a 1/16 inches thermocouple K arranged in the catalytic bed.

5.4 The investigated materials

Among the various perovkite based materials considered in this PhD research, the ones investigated at the ESRF facility are $LaCoO_3$-based. In particular several doped $LaCoO_3$ in which doping was in the A-site (with Sr) and in the B-site (with

Cu). RP-based cobaltites are not still considered because of the higher complexity of the structure and the need to go deeper into the effect of doping on structure modification. Moreover, the effect of nanocomposition was investigated focussing on systems obtained by depositing CuO highly dispersed nanoparticles on $LaCoO_3$-based perovskites. The effect of the support was evaluated by comparing the behaviour of CuO containing nanocomposites obtained by deposition on lanthanum oxide. Nanocomposition and doping are a strategic opportunities in the realization of active intermediate temperature anodes. Some of the doped $LaCoO_3$ electrodes have already successfully tested inside the research group I worked in, for cathodes of Intermediate Temperature SOFCs [22].

Moreover, being my convincement that catalytic and electrocatalytic behaviour can be strictly related, the investigated materials and nanocomposites were also selected on the basis of their reactivity in several reactions with particular attention paid to those applicable to environmental catalysis, such as automobile exhaust gas treatment, have attracted particular attention [21][157]. The Three Way Catalyst (TWC) is a catalyst able of converting simultaneously the three main pollutants of a gasoline engine: uncombusted hydrocarbons, carbon monoxide and nitrogen monoxide [18]. To reach this objective Sr and Cu doped $LaCoO_3$ based perovskites and copper oxide containing nanocomposites have also been studied with respect to their reactivity in TWC reactions revealing (appendix) that oxygen vacancies and mobility are precious both for electrocatalysts and catalysts. By means of strategic doping and nanocomposition we also obtained high performance catalysts very promising in view of the substitution of noble metals in catalysis.

Both if considering application in catalysis and in SOFCs it is essential to investigate the materials' reversibility under oxidizing, reducing, and reaction

conditions. For catalysts is essential to understand the reversibility of eventual structural variation which is determinant in order to assure the catalysts durability and stability. In SOFC's application the reversibility can also be strategic, not only for stability or durability but also because it opens an interesting and highly innovative opportunity: the realization of Reversible Solid Oxide Fuel Cells [187].

5.5 Time-resolved study

Time-resolved study of the structural dynamics of the La-Co-Cu-O oxide using high energy X-ray diffraction (ESRF Experiment number MA-313)

For this experiment Cu was coupled to $LaCoO_3$, a reducible perovskite-type oxide. The aim of the experiment was to analyze the effect of Cu and Sr on the formation of oxygen vacancies and mobility and thus on catalysis under pulsed experimental conditions, which are typical of their operation, and follow the structural changes. HE-XRD data were collected continuously (0.5 s/pattern; Q= 0-12 $Å^{-1}$; 74.9 keV) while the samples were heated to 450 °C and then cooled in the reaction feed consisting of 0.7 vol% CO, 0.15 vol% NO, 0.16 vol% C_3H_6 and oscillating O_2 concentration values (1-0.7 vol%, 30 s pulse) after treatment at 400°C in 5 vol% O_2 for 30 min.

Different catalytic and structural activities were observed when the copper was inside or outside the structure in the compounds $LaCo_{0.5}Cu_{0.5}O_3$ and $CuO/La_{0.5}Sr_{0.5}CoO_3$ or in absence of copper, $La_{0.5}Sr_{0.5}CoO_3$.

$LaCo_{0.5}Cu_{0.5}O_3$ was already studied as promising cathode for SOFC and as catalyst for TWC [21][22]. Following the XRD patterns under oscillating condition has allow to observe the correlation between activity and structural changes. Although the material was not active towards NO conversion at the temperature

range investigated, the patterns coupled with MS shown that the CO conversion is linked with the extraction of oxygen atoms from the surface of the material, as can be seen in figure 5.5 and in the magnification in figure 5.6. The lattice expansion/contraction appeared below 200 °C and increased in amplitude as a function of the temperature, however a transition phase was never observed.

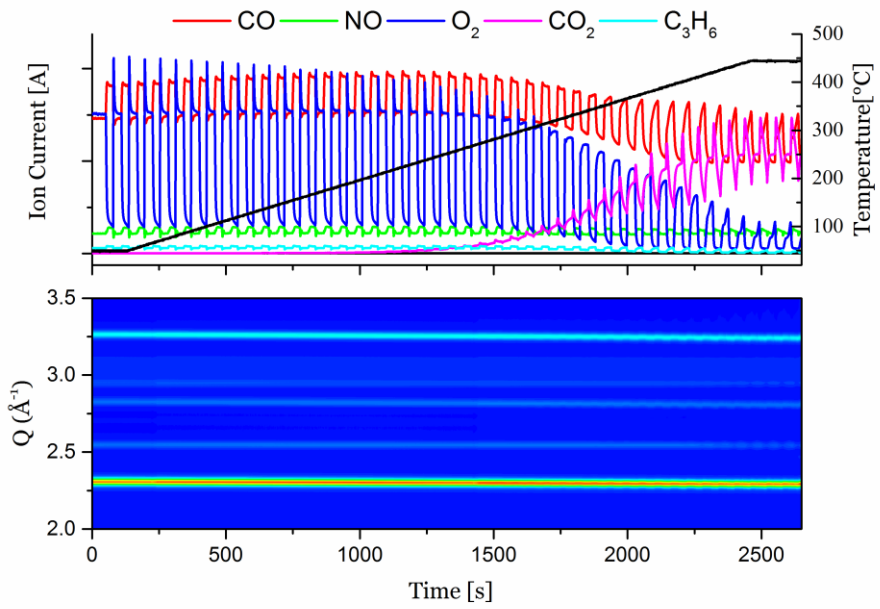

Figure 5.5: In the top panel reactants and products measured using MS, in the bottom 2D visualization of the operando time-resolved HE-XRD patterns while heating $LaCo_{0.5}Cu_{0.5}O_3$ with in 0.7 vol% CO, 0.15 vol% NO, 0.16 vol% C_3H_6 and oscillating O_2 concentration (1-0.7 vol%) between 100 °C and 450 °C.

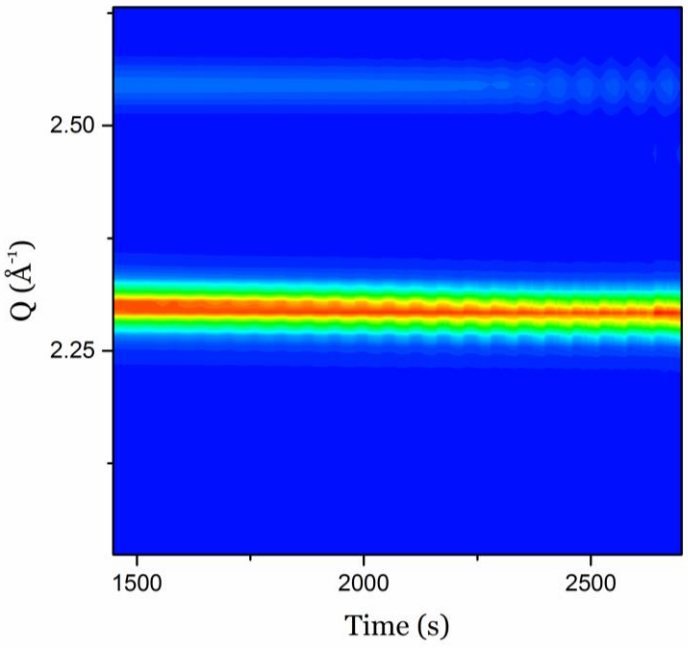

Figure 5.6: Magnification of 2D visualization of the operando time-resolved HE-XRD of $LaCo_{0.5}Cu_{0.5}O_3$

$CuO/La_{0.5}Sr_{0.5}CoO_3$ under stoichiometric conditions (without oscillating feed) has shown only CO conversion. However when the oscillating conditions were applied a remarkable change in reactivity was observed. In figure 5.7, the XRD and MS data collected for 20 wt% $CuO/La_{0.5}Sr_{0.5}CoO_3$ under oscillating feed are reported.

Both the catalytic activity and catalyst structure have shown variations allowing, beside the total CO conversion, the 90% of NO conversion at 450 °C. The observed hysteresis in NO conversion (extended down to 300 °C) was supposed to be induced by the structural changes. In fact, the XRD patterns have shown the transition from CuO to Cu_2O above 340 °C and then to Cu at 440 °C that persisted in the plateau simultaneously with the NO conversion, figure 5.7 and figure 5.8.

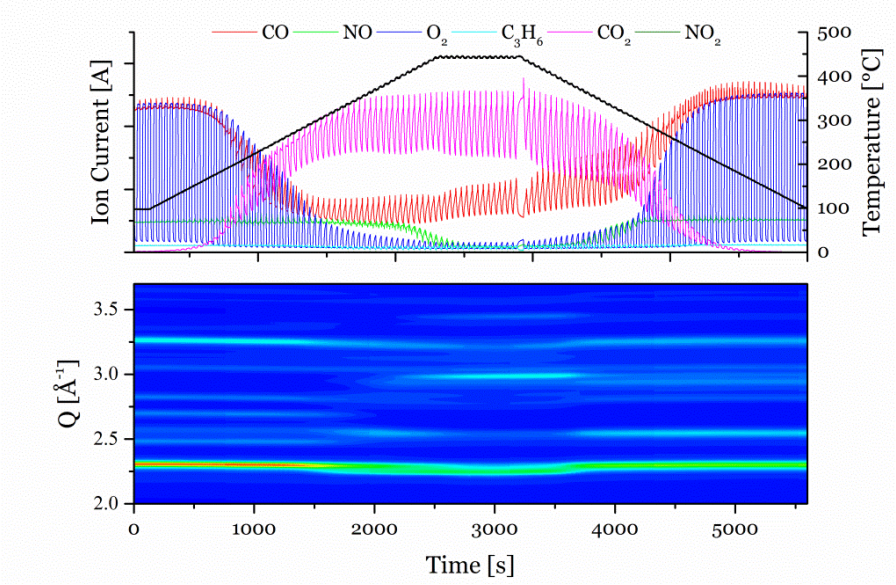

Figure 5.7 : In the top, the representation of the reactants and product gas evolution measured using a MS. In the botton 2D visualization of the operando time-resolved HEXRD patterns obtained while heating/cooling CuO/$La_{0.5}Sr_{0.5}CoO_3$ in 0.7 vol% CO, 0.15 vol% NO, 0.16 vol% C_3H_6 and oscillating O_2 conventration (1-0.7 vol%) between 100 °C and 450 °C.

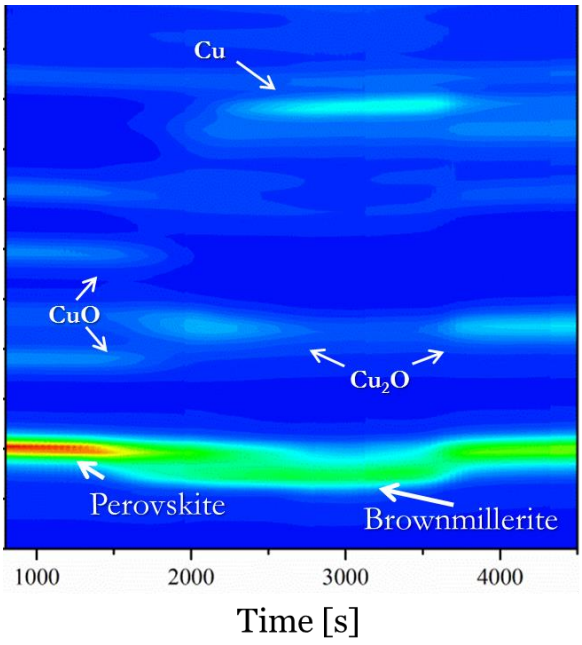

Figure 5.8: HE-XRD patterns magnification of CuO/$La_{0.5}Sr_{0.5}CoO_3$ phases transformation.

The reoxidation to CuO was not observed until 100 °C. Coupled with the copper transformation, also $La_{0.5}Sr_{0.5}CoO_3$ displayed reduction. The intense reflection (2.3 $Å^{-1}$) shifted to lower angles due to loss of O and lattice expansion and then above 350 °C the perovskite changes phase into a parent oxygen deficient brownmillerite ($La_3Co_3O_8$). The perovskite was then restored at 300 °C.

In order to going deep in the understanding of this catalytic behavior, identical experiments were performed on CuO/La_2O_3 and $La_{0.5}Sr_{0.5}CoO_3$ catalysts and in absence of propylene. The experiments carried out on 6 wt% CuO/La_2O_3 shown poor activity toward NO reduction and no CuO reduction, suggesting a synergic effect with perovskite. Also $La_{0.5}Sr_{0.5}CoO_3$ displayed low activity versus NO confirming that copper is essential to achieve deNO_x, figure 5.9. Differently from $LaCo_{0.5}Cu_{0.5}O_3$, doping with Sr has induced above 300 °C the transition phase from perovskite to brownmillerite. The absence of CuO on the surface seems not to affect the shift from perovskite to brownmillerite which appear similar to $CuO/LaCo_{0.5}Cu_{0.5}O_3$. However $La_{0.5}Sr_{0.5}CoO_3$ displayed a slower restoration of perovskite structure compare with $CuO/La_{0.5}Sr_{0.5}CoO_3$. A hypothesis could be that the copper have a role in the perovskite re-oxidation. This seems in according with the re-oxidation of Cu observed in $CuO/La_{0.5}Sr_{0.5}CoO_3$ during the cooling ramp. In fact only below the 100 °C the copper turn back to CuO while the perovskite has restored the structure above 300 °C.

Copper oxide resulted necessary in order to achieve the NO reduction but is not sufficient, pointing out an important role of perovskite. Moreover, in absence of C_3H_6 the deNO_x did not occur, suggesting that the reforming of propylene could be the responsible of NO reduction observed.

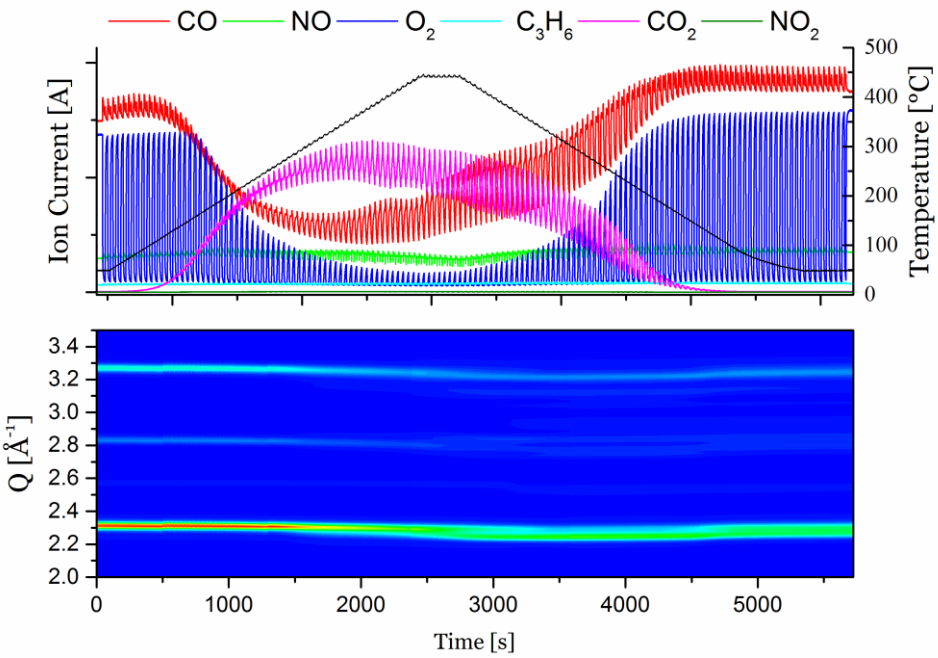

Figure 5.9: In the top, the representation of the reactants and product gas evolution measured using a MS. In the botton 2D visualization of the operando time-resolved HEXRD patterns obtained while heating/cooling $La_{0.5}Sr_{0.5}CoO_3$ in 0.7 vol% CO, 0.15 vol% NO, 0.16 vol% C_3H_6 and oscillating O_2 conventration (1-0.7 vol%) between 100 °C and 450 °C.

5.6 Chapter summary

$CuO/La_{0.5}Sr_{0.5}CoO_3$ has shown promising activity towards NO reduction under oscillating condition (1-0.7 vol%, 30 s pulse) as catalyst for automotive pollutants abatements. The synergic effect of CuO and perovskite seems the main cause of the NO reduction. The $deNO_x$ occur only when Cu(0) appeared and persist until the complete oxidation to Cu_2O (around 300 °C). Copper has shown also a possibly interaction with the perovskite during the re-oxidation of perovskite structure inducing a faster restoration. Doping with Sr induced a transition phase whereas in the same condition doping with Cu displayed only the contraction/expansion of lattice. This seems to point out strontium as a better dopant for increasing the oxygen ion mobility (reducibility) in $LaCoO_3$ based

perovskite. Finally the correlation between catalytic activity and structural changes, observed in all the compounds, were highlighted.

5.7 Acknowledgement

Greatly acknowledged goes to Dr Davide Ferri for his support and guidance and also to Dr. M. Di Michiel and the team of ID15 for their technical support during the allocated beamtime.

General conclusions and perspectives

Traditional SOFCs work between 800 °C and 1000 °C but this induces great materials deterioration and a high device cost. The development of new electrodes for SOFC application, characterized by high activity at intermediate temperatures (600-800 °C), is extremely important for the commercial diffusion and the future of this technology.

In this thesis titled "*Perovskite materials as electrodes for solid oxide fuel cells active toward sustainable reactions*", the purpose was to study two perovskite classes, titanates and cobaltites based, with the aim of verifying if they can be used as electrodes in SOFC fed with methane (Bio-gas). The methane was chosen due to its role as bio-fuel in the carbon footprint decrease (bio gas, CH_4 and CO_2). The upon mentioned perovskites were selected taking in account the literature suggestions regarding the excellent stability and poison tolerance of $SrTiO_3$ under SOFC condition and the high reactivity in oxidation and interesting cathodic performance of $La_{1-x}Sr_xCoO_3$ based perovskites. An important feature of the perovskites developed in this research was the low environmental and economic

impact. Following the suggestion of the EU report the material design and optimization was carried out avoiding platinum group metals and minimizing or avoiding rare earth elements.

$SrTiO_3$ based perovskites doped with barium in A-site and molybdenum or iron in the B-site were prepared through citrate method and studied as anode for IT-SOFC. The prepared materials were: $SrTi_{0.9}Mo_{0.1}O_3$, $SrTi_{0.6}Mo_{0.4}O_3$, $Ba_{0.5}Sr_{0.5}Ti_{0.9}Mo_{0.1}O_3$, $Ba_{0.5}Sr_{0.5}Ti_{0.9}Fe_{0.1}O_3$ and $Ba_{0.5}Sr_{0.5}Ti_{0.6}Fe_{0.4}O_3$. All the materials were obtained with high crystalline degree, however in order to successfully achieve the Ti substitution with Mo on $SrTi_{0.9}Mo_{0.1}O_3$, $SrTi_{0.6}Mo_{0.4}O_3$, $Ba_{0.5}Sr_{0.5}Ti_{0.9}Mo_{0.1}O_3$ an optimized reductive thermal treatment was necessary. The temperature programmed reduction and oxidation (TPR and TPO) carried out on the compounds followed by the XRD investigation have confirmed the great stability of $SrTi_{0.9}Mo_{0.1}O_3$, $SrTi_{0.6}Mo_{0.4}O_3$, $Ba_{0.5}Sr_{0.5}Ti_{0.9}Mo_{0.1}O_3$ under reductive environment but also have highlighted the segregation of insulating phases ($SrMoO_4$, $BaMoO_4$) when the materials are treated above 500 °C in oxidative atmosphere. If reduced, only $SrTi_{0.9}Mo_{0.1}O_3$ has shown the complete structure restoration (under 5% H_2 at 900 °C). The Fe-doped materials, in contrast, under reductive conditions suffers a large segregation of metal iron visible also at XRD. The performed reactivity tests have displayed activity toward CO oxidation for all titanates prepared at intermediate temperatures but the most curious results were observed in methane dry-reforming (CH_4:CO_2=1:1). In fact, among the samples only on $SrTi_{0.9}Mo_{0.1}O_3$ was active reaching 58% of CH_4 conversion at 800 °C. This phenomenon was probably related to a sort of synergic effect between Ti and Mo (Ti/Mo=9/1) which was not observed in the other samples. The deposition of 30% mol of Ni over $SrTi_{0.9}Mo_{0.1}O_3$ and $SrTi_{0.6}Mo_{0.4}O_3$ compounds was performed with the aim of increasing the catalytic activity. The

Ni deposition has greatly boosted the catalytic behaviour of compounds. CO oxidation were achieved at 500 °C and 700 °C for $Ni/SrTi_{0.9}Mo_{0.1}O_3$ and $Ni/SrTi_{0.6}Mo_{0.4}O_3$, respectively while methane dry reforming, still observed only on $Ni/SrTi_{0.9}Mo_{0.1}O_3$, dropped the ignition temperature from 650 °C (without nickel) to 500 °C. Although ignition temperature remarkably decreases, after one hour under methane reforming a slight reduction of CH_4 conversion, from 54% to 41%, was observed. The new activity reached was then kept for the followed five hours of test. The reactivity tests confirm that although some optimization steps are still required such as synthesis (to enhance the surface area) and the nickel particles dispersion, $Ni/SrTi_{0.9}Mo_{0.1}O_3$ could be used as material for the methane dry reforming. The electrochemical investigation (EIS) carried out on $SrTi_{0.9}Mo_{0.1}O_3$ and $SrTi_{0.6}Mo_{0.4}O_3$, infiltrated with 15 wt% of nickel, revealed an area specific resistance (ASR) under 5% of dry H_2 of 1.57 Ω cm^2 and 1.10 Ω·cm^2 respectively at 800 °C. The values are around one magnitude of order above the suggested value for a commercial application (0.15 Ω·cm^2) but definitely lower than the materials without nickel ($SrTi_{0.9}Mo_{0.1}O_3$ has 27.2 Ω cm^2). The capacitances, in according with what observed for the ASR and the reactivity tests, suggested that the limiting processes are linked to the reactions surface. The results point out the essential role of nickel as electro-catalyst in $Ni/SrTi_{1-x}Mo_xO_3$ suggesting that an optimization of the infiltration step could decrease the polarization resistance thanks to higher nickel particles dispersion. The molybdenum loading has displayed only a minor influence in the ASR values but a significant effect in reactivity tests. This has indicated that suitable Ti/Mo ratio has to be careful choose in the formulation step in order to meet the IT-SOFC, feed with bio-gas, demands. Although $Ni/SrTi_{0.9}Mo_{0.1}O_3$ has shown activity in methane dry reforming, the small deactivation observed probably induced by the carbon formation, has point out the necessity of a better formulation (alloy)

before to be study under methane. The ASR values observed at 800 °C for the compounds prepared are still high for a real use in a fuel cell. However the absences of critical raw materials, especially rare earth elements, encourage more study on these materials.

La_2CoO_4 based perovskites (K_2NiF_4 type structures) have been investigated as electrodes for symmetric IT-SOFC due to their high mixed-ionic-electronic conductivity and good mechanical and chemical compatibility with SOFC electrolyte and catalytic activity in oxidation. In order to enhance the La_2CoO_4 properties strontium was used as dopant in A-site while copper or nickel as B-site dopants. The two perovskites prepared, through citrate method, were $(LaSr)_2Co_{0.5}Cu_{0.5}O_4$ and $(LaSr)_2Co_{0.5}Ni_{0.5}O_4$. The materials were obtained at 900 °C in air but both have shown trace of secondary phases ($La_2Co_{0.75}Cu_{0.25}O_4$ and NiO) which were supposed not to negatively affecting the final performance of electrodes. The TPR analysis revealed the presence of unusual cation oxidation states, Co(IV) in both and Co(IV) and Cu(III) in Cu-doped, probably induced by the large aliovalent doping in the A-site (Sr(II)). The H_2 consumption, in according with literature data, has pointed out the completed breakdown of the structures above 750 °C under hydrogen in either $(LaSr)_2Co_{0.5}Cu_{0.5}O_4$ and $(LaSr)_2Co_{0.5}Ni_{0.5}O_4$. Instead, the stability versus methane on $(LaSr)_2Co_{0.5}Ni_{0.5}O_4$ up to 800 °C was confirmed by XRD investigation. The catalytic results have shown an excellent behaviour in CO conversion, achieving the total conversion at 500 °C and 400 °C respectively for $(LaSr)_2Co_{0.5}Cu_{0.5}O_4$ and $(LaSr)_2Co_{0.5}Ni_{0.5}O_4$, and an ignition temperature around 200 °C. Above 300 °C $(LaSr)_2Co_{0.5}Ni_{0.5}O_4$ boosted its performance achieving the total CO conversion 70 °C before $(LaSr)_2Co_{0.5}Cu_{0.5}O_4$. The achieved activities were particular interesting and superior to literature data for $LaCo_{0.5}Cu_{0.5}O_3$ and $La_{0.5}Sr_{0.5}Co_{0.5}Cu_{0.5}O_3$, prepared

with the same procedure. The compounds have shown also good activity versus direct methane oxidation, with 75% and 80% of CH_4 conversion for $(LaSr)_2Co_{0.5}Cu_{0.5}O_4$ and $(LaSr)_2Co_{0.5}Ni_{0.5}O_4$ at 800 °C. The chemical stability between samples and electrolyte powders was investigated through XRD but did not revealed incompatibility. However, SEM investigation has displayed the thermal expansion mismatch between $(LaSr)_2Co_{0.5}Cu_{0.5}O_4$ and GDC electrolyte, in addition a reactivity with electrolyte was found when the symmetrical cell section was observed. This has highlight that the XRD powders investigation could not be sufficient in order to have a chemical compatibility confirm. For this reason, only the symmetric cell $(LaSr)_2Co_{0.5}Ni_{0.5}O_4$/GDC/$(LaSr)_2Co_{0.5}Ni_{0.5}O_4$ was investigated by means of impedance spectroscopy. The ASR value detected under stationary air condition was 2.51 Ω m² at 700 °C which was found to be close to the literature values of $(LaSr)_2CoO_4$ (>2 Ω·cm²) and $La_{2-x}Sr_xCo_{0.5}Ni_{0.5}O_4$ (1.92 Ω·cm²). However at 800 °C the ASR undergoes a drop to 0.56 Ω m² which is close to the resistance suggested for a SOFC application, 0.15 Ω·cm². The data collected suggested as limiting processes the charge oxygen ion transfer at the interface electrode/electrolyte and the reaction processes, oxygen adsorption and dissociation, on the electrode surface. Optimized electrode morphology and the addiction of small quantities of electrolyte (in order to prepare a composite) could greatly enhance reaction activity and oxygen ion transfer, respectively. The most interesting data were observed under 5% CH_4/Ar flow conditions. At 700 °C, the ASR was 290.2 Ω m² confirming the high activation energy required for methane utilization but, increasing the working temperature at 800 °C, the ASR fall down to 0.94 Ω m² which is a remarkable value. The limiting processes, suggested by impedance data, are only related to the reaction processes. However other processes, covered by the large surface reaction polarization, could not be excluded taking in account the data collected under air conditions. The

investigation performed on $(LaSr)_2Co_{0.5}Ni_{0.5}O_4$ confirms the feasibility of the use $(LaSr)_2Co_{0.5}Ni_{0.5}O_4$ as electrode on symmetric solid oxide fuel cell directly fed with methane. A morphology optimization through pore former and the study of $(LaSr)_2Co_{0.5}Ni_{0.5}O_4$-GDC composite should be the next steps. Finally the test on the completed symmetric IT-SOFC should be performed in order to observe the final performance.

Summarizing $Ni/SrTi_{0.9}Mo_{0.1}O_3$ and $(LaSr)_2Co_{0.5}Ni_{0.5}O_4$ have shown good reactivity versus methane at 800 °C and promising ASR values as electrode in IT-SOFC. The best results were obtained between 700 °C and 800 °C but after the optimization of microstructural and/or the preparation of a composite, better results are expected.

Co-based perovskite-type oxides are used in various fields as catalysts, electrodes in solid oxide fuel cells and in gas separation (ceramic membranes). The large interest on these compounds is related to the tunability of their proprieties. The combination of element composition and proper doping allows the development and the control over the desired functionality. In order to go deeper inside the performance of these materials, both in term of MIEC and of catalytic activity, in situ time resolved high energy X-ray diffraction analysis was carried out to deeply investigate the structural changes of Co-based perovskite under pulsing conditions. The experiments were executed at European synchrotron radiation facility (ESRF) in Grenoble under the supervision of prof. Antonella Glisenti (Unipd) and Dr. Davide Ferri (PSI). $CuO/La_{0.5}Sr_{0.5}CoO_3$ has shown promising activity towards NO reduction under oscillating condition due to probably a synergic effect observed between CuO and the perovskite. Copper oxide resulted necessary in order to achieve the NO reduction but it was not sufficient, pointing out an important role of perovskite. Finally, Sr-doped cobaltites have shown

higher reducibility suggesting larger oxygen ion mobility than Cu-doped ones. The high reversibility observed on $LaCo_{0.5}Cu_{0.5}O_3$ and $CuO/La_{0.5}Sr_{0.5}CoO_3$ have revealed the potential of these materials encouraging further studies on more complex systems for symmetric and reversible solid oxide cell application. The data collected give useful information on structural change involved into catalytic activity.

Appendix.

Verifying reactivity through TWC reactions

A.1. Introduction

In this chapter we focus on catalytic activity of $LaCoO_3$-based perovskites in order to verify the reactivity of these catalysts, part of which investigated for reversibility under reduction, oxidation and reactive atmosphere in chapter 5, and evaluate the effect of doping and nanocomposition. To test the catalytic activity, we focused on TWC reactions, i.e. CO and HCs oxidation, together with NO reduction for the significant consequences of this application. Catalysts for automotive application, in fact, are based on noble metals (Platinum Metal Group – PGM). The development of innovative catalysts reducing (or avoiding) the use of PGMs is strategic, considering their cost and the limited supply.

A.2 Activity tests: experimental

Two series of catalytic activity tests were carried out, at atmospheric pressure. All the inlet composition and GHSV data are summarized in table A.1. The first set of measurements is based on simplified mixtures, a quartz reactor (6 mm ID) with a packed bed of powders; the temperature was monitored by a thermocouple right upstream of the bed. In this configuration two model reactions have been investigated: NO+CO and $CO+O_2$ (stoichiometric mixtures). The inert carrier was

always Ar. The flow rates were controlled by thermal mass flow meters (Vögtlin Instruments). The temperature of the bed was varied between RT and 400 °C. The composition of the gas mixture (before and after reaction) was measured by GC (Agilent 7890A), with a TCD detector and 13X (60/80 mesh, 1.8 m) and Porapak Q (1.8 m) columns.

The second set of catalytic activity measurements aimed at approaching actual conditions of an automotive exhaust. We used a different quartz flow reactor, 8 mm ID. The gas mixtures were measured by GC (Agilent 7820) with Porapak Q and MS5A packed columns in series; both TCD and FID detectors were used. The GC is online with the gas outlet and programmed to continuously sample the mixture, so that measurements can be collected at approx. 0.1 sample/min. A direct-access, 0-200amu mass spectrometer (Hiden QID-20) was also used to measure NO. The analysis with the MS is almost continuous (0.5-1 sample/min). The flow rates were controlled by mass flow meters (Brooks and Bronkhorst). The feed mixture is a complex one that approximates real automotive exhaust. It is detailed in table 2. Note that stoichiometry of O_2 is based on the amount required for all the fuels total oxidation plus the amount expected from NO conversion to N_2 and O_2.

Table A.1: Feed composition of all the measurements (Λ = O_2 fed/O_2 stoich = $[O_2]/(0.5\,[CO] + 0.5\,[H_2] + 2\,[CH_4] + 4.5\,[C_3H_6] + 5\,[C_3H_8] - 0.5\,[NO])$). For GHSV we assumed a bulk density of all the powders 1 g/ml.

Inert	CO_2	H_2O	O_2	CO	NO	H_2	CH_4	C_3H_6	C_3H_8	Λ		m_{cat}	Flow rate	GHSV
balance	%	%	%	%	%	%	ppm	ppm	ppm			mg	Sml/min	1/h
Ar	-	-	-	4	4	-	-	-	-	-		40	100	150000
Ar	-	-	2	4	-	-	-	-	-	1.0	Stoich	40	100	150000
He	15	10	0.777	0.7	0.1	0.233	230	450	230	1.0	Stoich	200	200	60000
He	15	10	0.609	0.9	0.1	0.300	300	600	300	0.6	Rich	200	200	60000

A.3 $LaCoO_3$-based perovskites: doping in A-site

The samples were prepared (table A.2) by the citrate method and characterized [21].

Table A.2: Composition and Specific Surface Area by BET, of the prepared samples.

Sample	T calcination (°C)	Specific surface area (m^2/g)
$La_{0.75}Sr_{0.25}Co_{0.5}Cu_{0.5}O_3$	900	10
$La_{0.5}Sr_{0.5}Co_{0.5}Cu_{0.5}O_3$	900	12
$La_{0.35}Sr_{0.35}Co_{0.5}Cu_{0.5}O_3$	900	8
$La_{0.5}Ba_{0.5}Co_{0.5}Cu_{0.5}O_3$	900	9
$La_{0.75}K_{0.25}Co_{0.5}Cu_{0.5}O_3$	900	9
$LaCo_{0.5}Cu_{0.5}O_3$	900	9
$LaCo_{0.5}Cu_{0.5}O_3$	600	17

A.3.1 Reactivity with CO + O_2 and CO + NO

The CO and NO conversions measured in the CO oxidation, and CO assisted NO reduction are shown in figure A.1.

In CO oxidation, figure 6A.1a, the substitution of La with Sr, Ba, and K causes a decrease of activity. The substitution of La to any extent always causes a loss of oxidation activity, reflected by a higher temperature required to initiate the reaction. The replacement with 50% of Sr determines an increment of the light off temperature of about 100-150 °C; this is observed also for the Sr-doped understoichiometric catalyst. The Ba and K doping further reduces the catalytic activity in CO oxidation; a similar behaviour is observed for $La_{0.75}Sr_{0.25}Co_{0.5}Cu_{0.5}O_3$. The shift of activity to higher temperature reflects in a lower conversion at the highest temperature sampled, i.e. 400 °C. Maximum measured conversions drop below the 95% achieved by $LaCo_{0.5}Cu_{0.5}O_3$; this is particularly evident for $La_{0.75}Sr_{0.25}Co_{0.5}Cu_{0.5}O_3$, $La_{0.75}K_{0.25}Co_{0.5}Cu_{0.5}O_3$ and $La_{0.5}Ba_{0.5}Co_{0.5}Cu_{0.5}O_3$ which reach around 60% of CO conversion. Also in the NO reduction by CO, figure A.1b and A.1c, the substitution of La reduces the activity; the reactions always start at higher temperature than $LaC_{0.5}Cu_{0.5}O_3$. Interestingly, the effect of temperature on the reactivity is very different. $La_{0.5}Sr_{0.5}Co_{0.5}Cu_{0.5}O_3$ is indeed active at higher temperature, but once it starts being active, it immediately achieves almost the same activity of $LaC_{0.5}Cu_{0.5}O_3$: 79 and 84 % for CO and NO, respectively compared to 91 and 87% of $LaC_{0.5}Cu_{0.5}O_3$; the understoichiometric $La_{0.35}Sr_{0.35}Co_{0.5}Cu_{0.5}O_3$ shows even better performance at 350 °C. Unlike Sr-doped cobaltates, $La_{0.75}K_{0.25}Co_{0.5}Cu_{0.5}O_3$ shows slightly lower ignition temperature but it reaches only 60% at 400 °C. It appears that the activity of $LaCo_{0.5}Cu_{0.5}O_3$ improves with temperature much less effectively than doped perovskites.

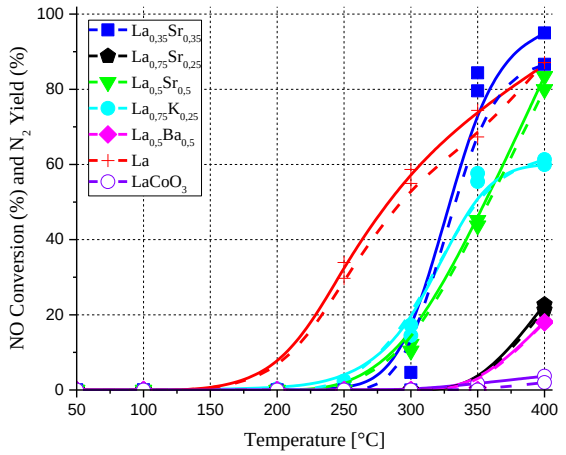

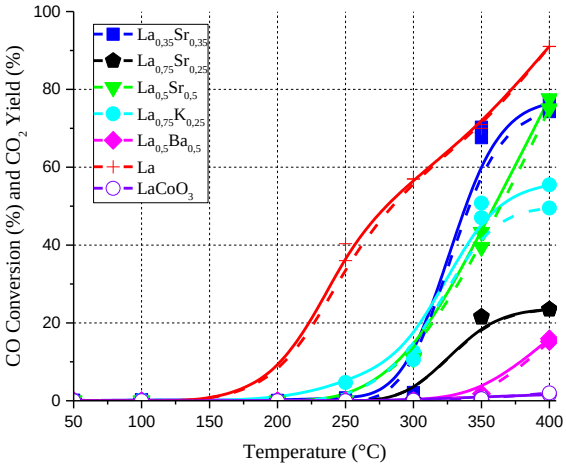

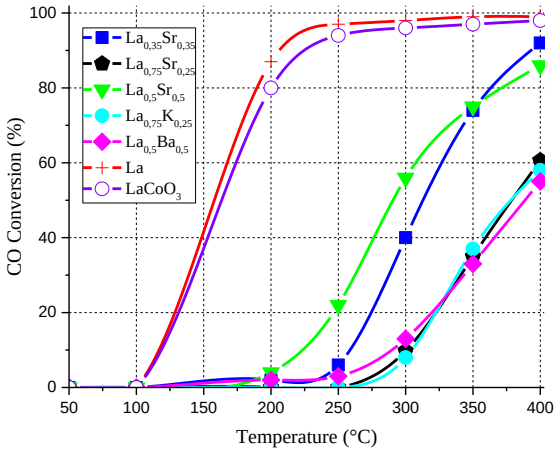

Figure A.1: conversions as a function of temperature: (upper) CO conversion in $CO+O_2$ reaction, (intermediate) CO and (lower) NO conversions in CO+NO. N_2 and CO_2 yields in

dashed lines.

+ $LaCo_{0.5}Cu_{0.5}O_3$; ▼$La_{0.5}Sr_{0.5}Co_{0.5}Cu_{0.5}O_3$; ■ $La_{0.35}Sr_{0.35}Co_{0.5}Cu_{0.5}O_3$; ♦ $La_{0.5}Ba_{0.5}Co_{0.5}Cu_{0.5}O_3$;

• $La_{0.75}K_{0.25}Co_{0.5}Cu_{0.5}O_3$; ⬟ $La_{0.75}Sr_{0.25}Co_{0.5}Cu_{0.5}O_3$; ○ $LaCoO_3$.

At the highest temperature, the best activity, approaching complete CO and NO conversion is achieved by the undoped, 50% Sr-doped and understoichiometric samples. The worst results are achieved by $La_{0.75}Sr_{0.25}Co_{0.5}Cu_{0.5}O_3$ and $La_{0.5}Ba_{0.5}Co_{0.5}Cu_{0.5}O_3$; they activate at even higher temperature, and at the maximum temperature (400 °C) conversion remains very low, around 20% both for CO and NO.

The comparison among the reactivity results clearly indicates that the most promising dopant is Sr. The light off temperature on Sr-doped samples, (except for $La_{0.75}Sr_{0.25}Co_{0.5}Cu_{0.5}O_3$) for both CO oxidation and CO assisted NO reduction slightly increases but at 350-400 °C the same activity of $LaCo_{0.5}Cu_{0.5}O_3$ is observed and 50% La is avoided. Interesting improvements are obtained also with the understoichiometric Sr-doped copper cobaltate. It is important to observe that the comparison between the NO conversion and the amount of N_2 revealed sustains the selectivity toward reduction (in fact NO_2 was never observed).

A.4 $CuO/La_{0.5}Sr_{0.5}CoO_3$

A.4.1 Reactivity in $CO + O_2$

Figure A.2 compares the CO conversion as a function of temperature achieved for $La_{0.5}Sr_{0.5}CoO_3$ and for the nanocomposites. The activity at temperatures higher than 250 °C is very similar with almost complete conversion (>90%). At 200 °C, in contrast, the effect of copper deposition is well evident and the catalysts with 15 and 20% reach 100% conversion; the nanocomposites with 10% of copper

shows slightly lower conversion whereas the performance of the sample with 30% are significantly worst. The support is almost inactive until at least 300 °C.

A.4.2 Reactivity in CO + NO

The catalytic tests with CO+NO mixtures were performed using stoichiometric amounts of CO and NO, each at 4% dilution; the results are compared in figure 6A.2. The supporting $La_{0.5}Sr_{0.5}CoO_3$ shows very low activity even at 400 °C. The catalytic performance is greatly enhanced by copper oxide deposition and increases with copper amount until 20%. A common light-off temperature > 200 °C is observed as well as conversions around 80-90% at 400 °C.

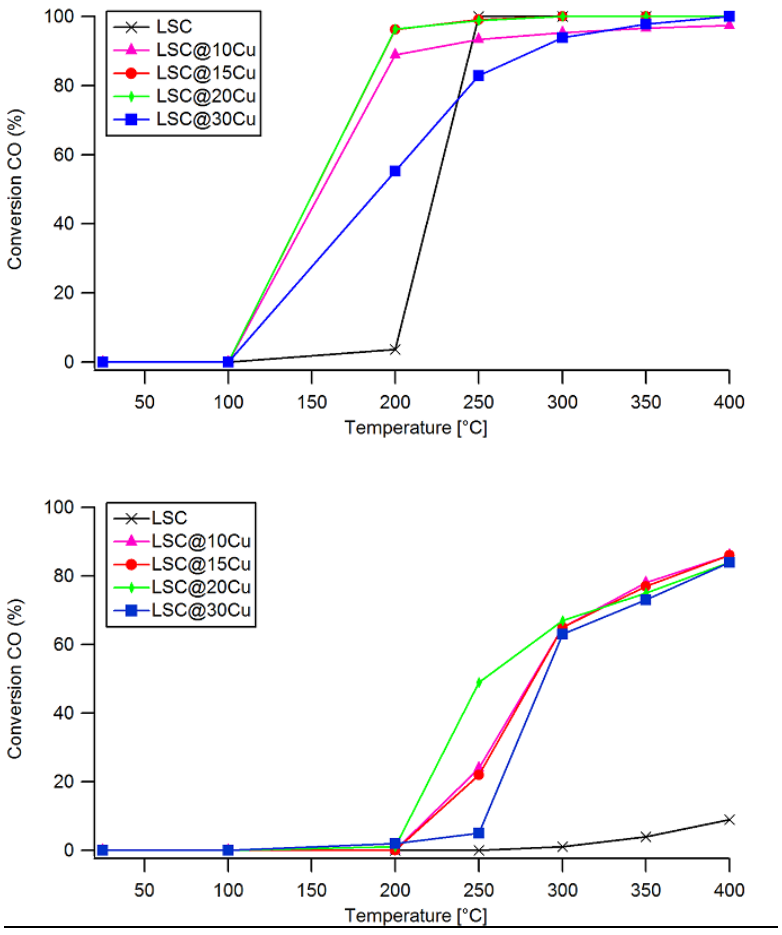

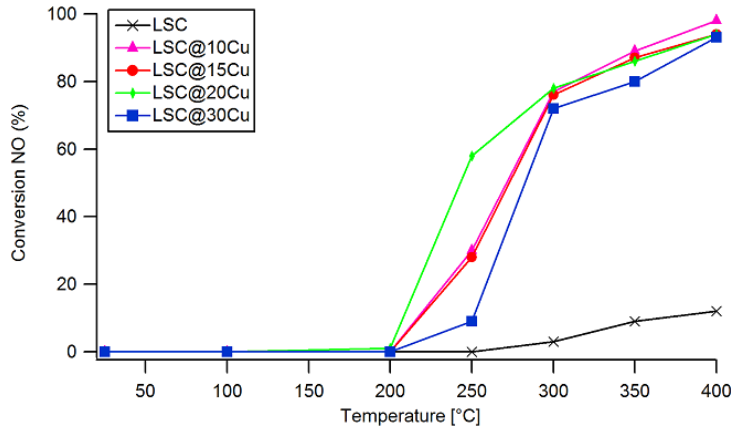

Figure A.2: CO and NO conversion as a function of temperature obtained for $La_{0.5}Sr_{0.5}CoO_3$ and Cu@ $La_{0.5}Sr_{0.5}CoO_3$ catalysts in the CO oxidation (upper graph) and in the CO assisted NO reduction.

These considerations suggest that an optimized composition is needed in order to obtain the maximum catalytic activity. A synergic effect of copper and perovskite surface may be strictly involved in the reactivity, so an excessive coverage of the support appears not so effective.

A.5 Reactivity with the complex mixture

The complex mixture more realistically samples the activity of materials, at conditions approaching the real automotive exhaust. In addition to a larger number of species, including a relevant amount of steam, we compared the catalysts behavior at both stoichiometric amount of O_2, based on the combustible reagents, as well as in lack of O_2 (fuel rich conditions). In the figures A.3 and A.4 we compare the different activity of materials in the removal of each single species, at both stoichiometric and rich conditions. Note that a different experimental setup and operation mode compared to the simpler mixtures above allowed to collect data at a higher frequency, over a larger temperature range (up to 600 °C), better spotting the onset of activity. Also, a preconditioning of the

catalyst in air at 600 °C distinguishes these tests from the ones using model reactions.

Figure A.3a shows the activity of all catalysts in CO oxidation. The first surprising result is that doping with Sr results in an improved activity in CO oxidation, outperforming $LaCo_{0.5}Cu_{0.5}O_3$. K-doping is the less effective. Results with nominal stoichiometric O_2 can be compared with those reported in figure A.1; we observe an unexpected switch between $LaCo_{0.5}Cu_{0.5}O_3$ and $La_{0.5}Sr_{0.5}Co_{0.5}Cu_{0.5}O_3$ as the most active one. This different behaviour suggests to consider the higher oxygen mobility provided by Sr-doping and the difference in reaction conditions. The other materials, except for K-doped, becomes active within the same temperature range, 200-300 °C. It is interesting to observe that the CO conversion is higher for the Ba-doped catalysts than for the K-doped one. The surface segregation of cobalt oxide revealed by XPS in $La_{0.5}Ba_{0.5}Co_{0.5}Cu_{0.5}O_3$ could contribute, being cobalt oxide very active in CO oxidation.

With understoichiometric O_2, figure A.3b, the activity shifts to higher temperature; differences among catalysts reduce, preserving the same ranking. The lower catalytic activity observed in understoichimetric conditions is consistent with the Mars-van Krevelen mechanism, usually accepted for CO oxidation. CO molecularly adsorbs on Lewis surface acidic sites and reacts with oxygen species near neighbors of the Lewis acidic sites originating CO_2 that desorbs. The result is a partially reduced site (oxygen vacancy) that may be re-oxidized by gas phase oxygen or deactivate by interacting with CO.

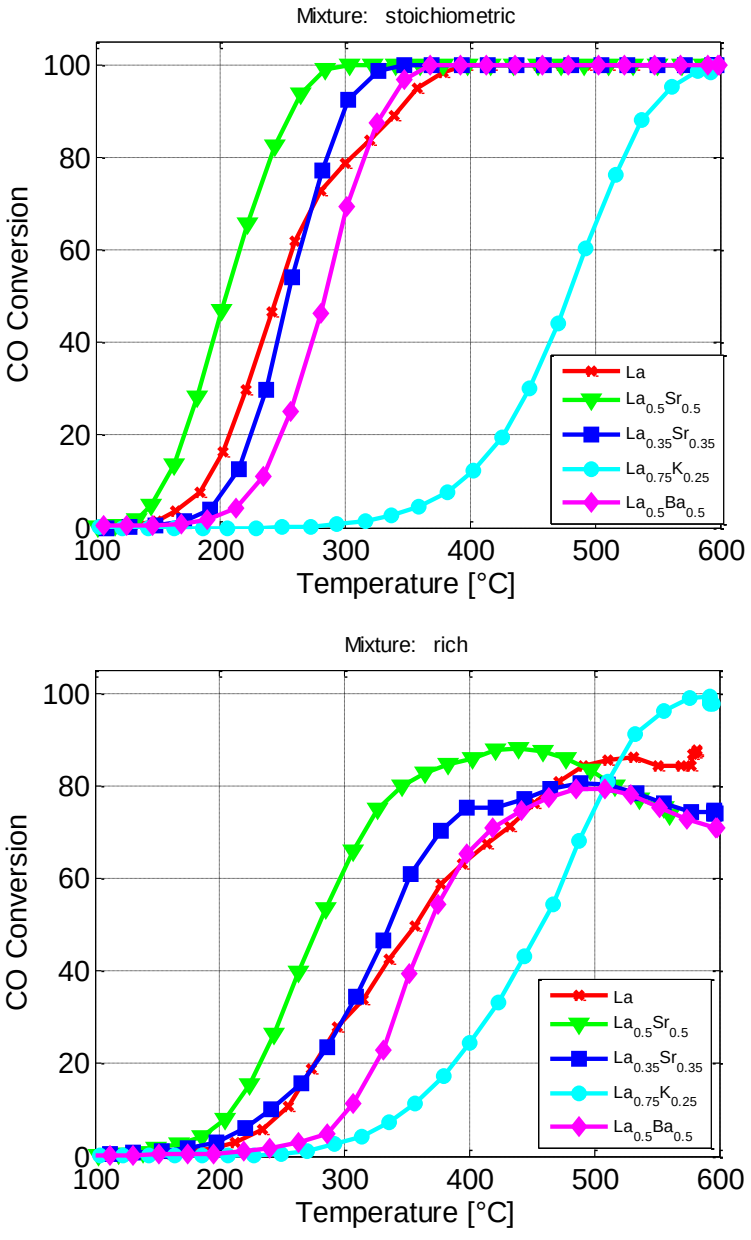

Figure A.3: CO conversion as a function of temperature with the complex TWC mixture. Stoichiometric (a) and understoichiometric O_2, i.e. fuel rich, (b).

× $LaCo_{0.5}Cu_{0.5}O_3$; ▼ $La_{0.5}Sr_{0.5}Co_{0.5}Cu_{0.5}O_3$; ■ $La_{0.35}Sr_{0.35}Co_{0.5}Cu_{0.5}O_3$;
♦ $La_{0.5}Ba_{0.5}Co_{0.5}Cu_{0.5}O_3$; • $La_{0.75}K_{0.25}Co_{0.5}Cu_{0.5}O_3$

Oxygen deficiency can decrease the oxygen availability un-favouring oxidation. Moreover the presence of reducible cations on the perovskite surface is helpful for CO_2 desorption and the presence of an efficient redox couple can be decreased by the fuel rich conditions. Note that all the catalysts, except K-doped one, reach a

maximum of CO conversion at fuel rich conditions; at higher temperature there is a drop of conversion.

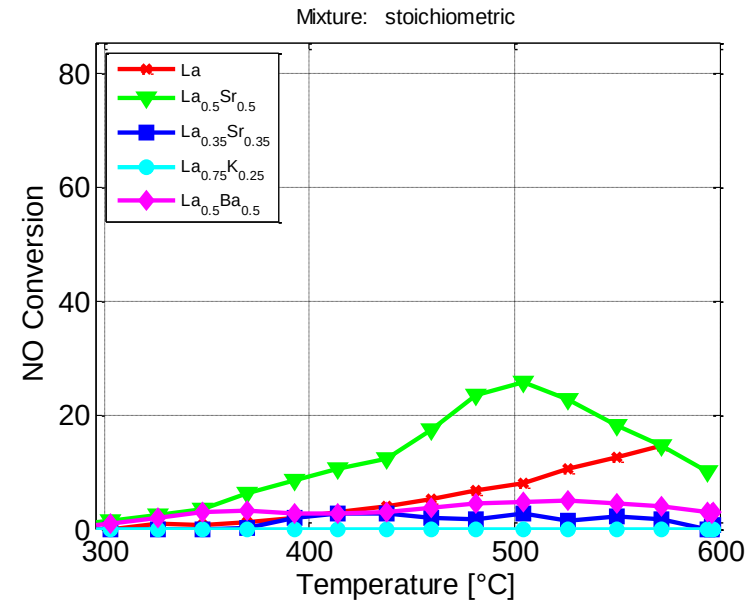

a)

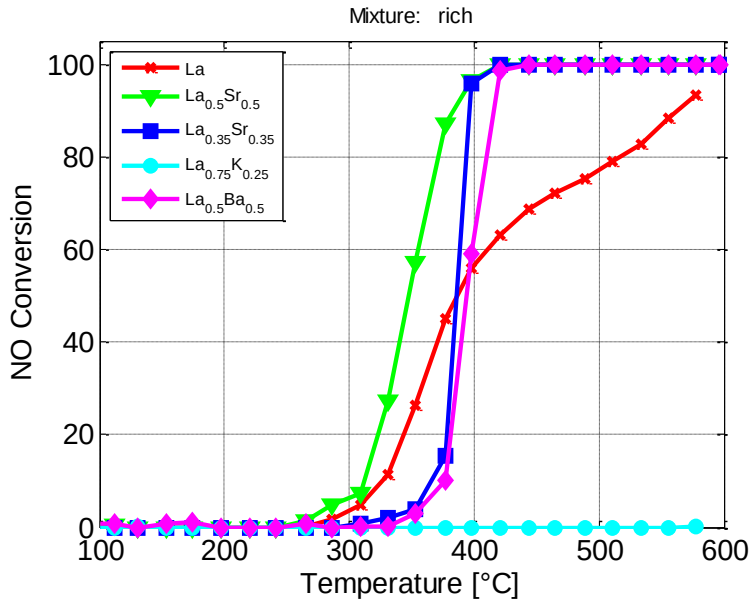

b)

Figure A.4: NO conversion as a function of temperature with the complex TWC mixture. Stoichiometric (a) and understoichiometric O_2, i.e. fuel rich, (b).

× $LaCo_{0.5}Cu_{0.5}O_3$; ▼ $La_{0.5}Sr_{0.5}Co_{0.5}Cu_{0.5}O_3$; ■ $La_{0.35}Sr_{0.35}Co_{0.5}Cu_{0.5}O_3$; ♦ $La_{0.5}Ba_{0.5}Co_{0.5}Cu_{0.5}O_3$; • $La_{0.75}K_{0.25}Co_{0.5}Cu_{0.5}O_3$

The NO removal is inefficient in the presence of stoichiometric O_2, as shown by figure A.4a. The best result is a modest 20% conversion by Sr-doped catalyst, at high temperature (500 °C). Total NO removal can be obtained in O_2 poor mixture, as shown in figure 6.3b, even if O_2 amount is not much smaller than the stoichiometric (just 60% of that). This is consistent with the mechanism proposed for perovskites that considers the interaction between NO and the oxygen vacancies present on the perovskite surface, as the rate determining step for NO reduction. Moreover, it has to be considered that, under O_2-understoichiometric conditions, lower oxidation states are possible for the surface cations and their presence can affect the interaction of NO with the surface active sites and thus the reactivity, as also suggested by the increment in NO reduction activity observed in the model reaction after H_2 treatment. Catalysts lead to total NO removal below 400°C. $LaCo_{0.5}Cu_{0.5}O_3$ behaves somehow differently, gradually improving NO conversion with temperature, as already observed in the simplified mixture (figure A.1b). The presence of small amounts of highly distributed CuO on the perovskite surface may play a role but further studies are in course to evaluate the reaction mechanisms under model and real conditions.

References

[1] U.S. Energy Information Administration, “International Energy Outlook 2017 Overview,” 2017.

[2] BP, “BP Statistical Review of World Energy 2017,” 2017.

[3] E. Union, E. Council, and E. C. Foundation, “Roadmap 2050,” 2009.

[4] J. P. Hansen, P. A. Narbel, and D. L. Aksnes, “Limits to growth in the renewable energy sector,” *Renew. Sustain. Energy Rev.*, vol. 70, no. November, pp. 769–774, 2017.

[5] REN 21, “Renewables 2017: global status report,” 2017.

[6] T. K. Mandal and D. H. Gregory, “Hydrogen: A future energy vector for sustainable development,” *Proc. Inst. Mech. Eng. Part C J. Mech. Eng. Sci.*, vol. 224, no. 3, pp. 539–558, 2010.

[7] T. F. Edgar *et al.*, *Process Control*. 2008.

[8] Omar Z. and M. F. Orhan, “An overview of fuel cell technology: Fundamentals and applications,” *Renew. Sustain. Energy Rev.*, vol. 32, pp. 810–853, 2014.

[9] L. Carrette, K. A. Friedrich, and U. Stimming, “Fuel Cells: Principles, Types, Fuels, and Applications,” *ChemPhysChem*, vol. 1, no. 4, pp. 162–193, 2000.

[10] J. Larminie and A. Dicks, *Fuel Cell Systems Explained*, vol. 93. 2001.

[11] U. Bossel, “Universal SOFC Module for Rapid Start-Ups,” vol. 35, no. 1, pp. 179–186, 2011.

[12] I. EG&G Services Parsons and Science, *Fuel Cell Handbook*, no. October. 2000.

[13] M. Lo Faro, V. Antonucci, P. L. Antonucci, and a. S. Aricó, “Fuel flexibility: A key challenge for SOFC technology,” *Fuel*, vol. 102, pp. 554–559, 2012.

[14] a. Lee, “Analysis of Solid State, Solid Oxide Electrolyte Based Direct Carbon Fuel Cells,” no. March, 2010.

[15] D. Neagu and J. T. S. Irvine, “Structure and properties of $La_{0.4}Sr_{0.4}TiO_3$ Ceramics for use as anode materials in solid oxide fuel cells,” *Chem. Mater.*, vol. 22, no. 17, pp. 5042–5053, 2010.

[16] S. P. S. Badwal, S. Giddey, C. Munnings, and a. Kulkarni, “Review of progress in high temperature solid oxide fuel cells,” *J. Aust. Ceram. Soc.*, vol. 50, pp. 23–37, 2014.

[17] S. Srinivasan, *Fuel cells From Fundamentals to Applicaions*. 2006.

[18] P. Oxide and O. Fuel, *Perovskite oxide for fuel cells*. 2009.

[19] X. Zhou, N. Yan, K. T. Chuang, and J. Luo, “Progress in La-doped $SrTiO_3$ (LST)-based anode materials for solid oxide fuel cells,” *RSC Adv.*, vol. 4, p. 118, 2014.

[20] C. D. Savaniu and J. T. S. Irvine, “La-doped $SrTiO_3$ as anode material for IT-SOFC,” *Solid State Ionics*, vol. 192, pp. 491–493, 2011.

[21] A. Garbujo *et al.*, “On A-doping strategy for tuning the TWC catalytic performance of perovskite based catalysts,” *Appl. Catal. A Gen.*, vol. 544, no. June, pp. 94–107, 2017.

[22] M. M. Natile, G. Eger, P. Batocchi, F. Mauvy, and A. Glisenti, “Strontium and copper doped $LaCoO_3$: New cathode materials for solid oxide fuel cells?,” *Int. J. Hydrogen Energy*, vol. 42, no. 3, pp. 1724–1735, 2016.

[23] A. Kulkarni *et al.*, “Mixed ionic electronic conducting perovskite anode for direct carbon fuel cells,” *Int. J. Hydrogen Energy*, vol. 37, no. 24, pp. 19092–19102, 2012.

[24] Y. Hu *et al.*, “Popper-type layered cobaltites as cathode materials for IT-SOFC application,” vol. 8, pp. 0–8, 2012.

[25] W. F. Libby, “Promising catalyst for Auto Exhaust,” *Science (80)*, vol. 171, no. 3970, pp. 500–501, 1971.

[26] NASA, “https://www.nasaspaceflight.com,” 1960.

[27] S. M. Haile, “Fuel cell materials and components,” vol. 51, pp. 5981–6000, 2003.

[28] G. Merle, M. Wessling, and K. Nijmeijer, “Anion exchange membranes for alkaline fuel cells: A review,” *J. Memb. Sci.*, vol. 377, no. 1–2, pp. 1–35, 2011.

[29] W. R. W. Daud, R. E. Rosli, E. H. Majlan, S. A. A. Hamid, R. Mohamed, and T. Husaini, “PEM fuel cell system control: A review,” *Renew. Energy*, vol. 113, pp. 620–638, 2017.

[30] V. S. Bagotsky and A.N., *Fuel cells Problems and Solutions*. 2012.

[31] B. C. Ong, S. K. Kamarudin, and S. Basri, “Direct liquid fuel cells: A review,” *Int. J. Hydrogen Energy*, vol. 42, no. 15, pp. 10142–10157, 2017.

[32] R. J. Gorte, H. Kim, and J. M. Vohs, “Novel SOFC Anodes for the Direct Electrochemical Oxidation of Hydrocarbons,” *J. Power Sources*, vol. 106, p. 10/15, 2002.

[33] A. Orera and P. R. Slater, “New chemical systems for solid oxide fuel cells,” *Chem. Mater.*, vol. 22, no. 3, pp. 675–690, 2010.

[34] L. Fan, C. Wang, M. Chen, and B. Zhu, “Recent development of ceria-based (nano)composite materials for low temperature ceramic fuel cells and electrolyte-free fuel cells,” *J. Power Sources*, vol. 234, pp. 154–174, 2013.

[35] S. Tao and J. T. S. Irvine, “Discovery and characterization of novel oxide anodes for solid oxide fuel cells,” *Chem. Rec.*, vol. 4, no. 2, pp. 83–95, 2004.

[36] J. C. Ruiz-Morales *et al.*, “Is YSZ stable in the presence of Cu?,” *J. Mater. Chem.*, vol. 18, no. 42, pp. 5072–5077, 2008.

[37] S. Sengodan *et al.*, “Layered oxygen-deficient double perovskite as an efficient and stable anode for direct hydrocarbon solid oxide fuel cells.,” *Nat. Mater.*, vol. 14, no. 2, pp. 205–9, 2015.

[38] F. M. T. Xia, A. Brüll, A. Grimaud, S. Fourcade and J. M. B. H. Zhao, J.C. Grenier a, “Optimization of the electrochemical performance of a Ni/$Ce_{0.9}Gd_{0.1}O_2$ impregnated $La_{0.57}Sr_{0.15}TiO_3$ anode in hydrogen,” vol. 35, pp. 1–9, 2014.

[39] D. Marrero-López, J. Peña-Martínez, J. C. Ruiz-Morales, M. C. Martín-Sedeño, and P. Núñez, “High temperature phase transition in SOFC anodes

based on $Sr_2MgMoO_{6-\delta}$," *Journal of Solid State Chemistry*, vol. 182. pp. 1027–1034, 2009.

[40] P. Zhang, Y. H. Huang, J. G. Cheng, Z. Q. Mao, and J. B. Goodenough, "Sr_2CoMoO_6 anode for solid oxide fuel cell running on H_2 and CH_4 fuels," *J. Power Sources*, vol. 196, no. 4, pp. 1738–1743, 2011.

[41] B. He, Z. Wang, L. Zhao, X. Pan, X. Wu, and C. Xia, "Ti-doped molybdenum-based perovskites as anodes for solid oxide fuel cells," *J. Power Sources*, vol. 241, pp. 627–633, 2013.

[42] D. J. L. Brett, A. Atkinson, N. P. Brandon, and S. J. Skinner, "Intermediate temperature solid oxide fuel cells," *Chem. Soc. Rev.*, vol. 37, no. 8, p. 1568, 2008.

[43] N. Mahato, A. Banerjee, A. Gupta, S. Omar, and K. Balani, "Progress in Material Selection for Solid Oxide Fuel Cell Technology: A Review," *Prog. Mater. Sci.*, vol. 72, pp. 141–337, 2015.

[44] A. Weber and E. Ivers-Tiffée, "Materials and concepts for solid oxide fuel cells (SOFCs) in stationary and mobile applications," *J. Power Sources*, vol. 127, no. 1–2, pp. 273–283, 2004.

[45] J. T. S. Irvine and P. Connor, "Solid oxide fuels cells: Facts and figures: Past, present and future perspectives for SOFC Technologies," *Green Energy Technol.*, vol. 55, 2013.

[46] S. B. Adler, "Factors governing oxygen reduction in solid oxide fuel cell cathodes," *Chem. Rev.*, vol. 104, no. 10, pp. 4791–4843, 2004.

[47] Æ. P. Holtappels, Æ. T. Graule, T. Nakamura, and Æ. L. J. Gauckler, "Materials design for perovskite SOFC cathodes," pp. 985–999, 2009.

[48] S. J. Mcphail, L. Leto, and C. Boigues-muñoz, "DOSSIER THE YELLOW PAGES OF SOFC TECHNOLOGY International Status of SOFC deployment," 2013.

[49] P. Von Dollen and S. Barnett, "A study of screen printed yttria-stabilized zirconia layers for solid oxide fuel cells," *J. Am. Ceram. Soc.*, vol. 88, no. 12, pp. 3361–3368, 2005.

[50] J. Will, A. Mitterdorfer, C. Kleinlogel, D. Perednis, and L. J. Gauckler, "Fabrication of thin electrolytes for second-generation solid oxide fuel cells," *Solid State Ionics*, vol. 131, no. 1, pp. 79–96, 2000.

[51] D. Ding, X. Li, S. Y. Lai, K. Gerdes, and M. Liu, “Enhancing SOFC cathode performance by surface modification through infiltration,” *Energy Environ. Sci.*, vol. 7, no. 2, p. 552, 2014.

[52] J. T. S. Irvine, D. Neagu, M. C. Verbraeken, C. Chatzichristodoulou, C. Graves, and M. B. Mogensen, “Evolution of the electrochemical interface in high-temperature fuel cells and electrolysers,” *Nat. Energy*, vol. 1, no. 1, p. 15014, 2016.

[53] Y. Lin, Z. Zhan, J. Liu, and S. A. Barnett, “Direct operation of solid oxide fuel cells with methane fuel,” vol. 176, pp. 1827–1835, 2005.

[54] Y. Shiratori, T. Ijichi, T. Oshima, and K. Sasaki, “Internal reforming SOFC running on biogas,” *Int. J. Hydrogen Energy*, vol. 35, no. 15, pp. 7905–7912, 2010.

[55] I. EG&G Technical Services, “Fuel Cell Handbook,” *Fuel Cell*, vol. 7 Edition, no. November, pp. 1–352, 2004.

[56] J. W. Fergus, “Oxide anode materials for solid oxide fuel cells,” *Solid State Ionics*, vol. 177, no. 17–18, pp. 1529–1541, 2006.

[57] J. Staniforth and K. Kendall, “Biogas powering a small tubular solid oxide fuel cell,” vol. 71, pp. 275–277, 1998.

[58] J. B. Hansen, “Fuel processing for fuel cells and power to fuels as seen from an industrial perspective,” *J. Catal.*, vol. 328, pp. 280–296, 2015.

[59] M. Persson, O. Jonsson, and A. Wellinger, “Biogas Upgrading To Vehicle Fuel Standards and Grid,” 2007.

[60] H. Tanaka and M. Misono, “Advances in designing perovskite catalysts,” *Curr. Opin. Solid State Mater. Sci.*, vol. 5, pp. 381–387, 2001.

[61] S. Royer, D. Duprez, and S. Kaliaguine, “Oxygen mobility in $LaCoO_3$ perovskites,” *Catal. Today*, vol. 112, pp. 99–102, 2006.

[62] X. Li, Q. Hu, Y. Yang, Y. Wang, and F. He, “Studies on stability and coking resistance of $Ni/BaTiO_3$-Al_2O_3 catalysts for lower temperature dry reforming of methane (LTDRM),” *Appl. Catal. A Gen.*, vol. 413–414, pp. 163–169, 2012.

[63] A. E. Bocquet *et al.*, “Electronic structure of $SrFe^{4+}O_3$ and related Fe perovskite oxides,” *Phys. Rev. B*, vol. 45, no. 4, pp. 1561–1570, 1992.

[64] A. Maignan, C. Martin, N. Nguyen, and B. Raveau, “Magnetoresistance in the ferromagnetic metallic perovskite $SrFe_{1-x}Co_xO_3$,” *Solid State Sci.*, vol. 3, no. 1–2, pp. 57–63, 2001.

[65] C. Michel, J. Provost, and B. Raveau, “A series of oxygen-defect perovskites containing CuII and CuIII: The oxides $La_{3-x}Ln_xBa_3$ [$CuII_{5-2y}$ $CuIII_{1+2y}$] O14+y,” *J. Solid State Chem.*, pp. 151–156, 1981.

[66] S. Tao and J. T. S. Irvine, “Structural and electrochemical properties of the perovskite oxide $Pr_{0.7}Sr_{0.3}Cr_{0.9}Ni_{0.1}O_3$,” *Solid State Ionics*, vol. 179, no. 19–20, pp. 725–731, 2008.

[67] A. L. Sauvet and J. T. S. Irvine, “Catalytic activity for steam methane reforming and physical characterisation of $La_{1-x}Sr_xCr_{1-y}Ni_yO_3$,” *Solid State Ionics*, vol. 167, no. 1–2, pp. 1–8, 2004.

[68] Y.-H. Huang, G. Liang, M. Croft, M. Lehtimäki, M. Karppinen, and J. B. Goodenough, “Double-Perovskite Anode Materials Sr_2MMoO_6 (M = Co, Ni) for Solid Oxide Fuel Cells,” *Chem. Mater.*, vol. 21, no. 11, pp. 2319–2326, 2009.

[69] S. Tao, J. T. S. Irvine, and J. A. Kilner, “An efficient solid oxide fuel cell based upon single-phase perovskites,” *Adv. Mater.*, vol. 17, no. 14, pp. 1734–1737, 2005.

[70] Z. Cheng, S. Zha, L. Aguilar, D. Wang, J. Winnick, and M. Liu, “A Solid Oxide Fuel Cell Running on H2SCH4 Fuel Mixtures,” *Electrochem. Solid-State Lett.*, vol. 9, no. 1, p. A31, 2006.

[71] R. Martínez-Coronado, J. a. Alonso, and M. T. Fernández-Díaz, “$SrMo_{0.9}Co_{0.1}O3_{-\delta:}$ A potential anode for intermediate-temperature solid-oxide fuel cells (IT-SOFC),” *Journal of Power Sources*, vol. 258. pp. 76–82, 2014.

[72] European Commission, “Report on critical raw materials for the EU, Report of the Ad hoc Working Group on defining critical raw materials,” no. May, p. 41, 2014.

[73] F. Yi, H. Li, H. Chen, R. Zhao, and X. Jiang, “Preparation and characterization of la and Cr co-doped $SrTiO_3$ materials for SOFC anode,” *Ceram. Int.*, vol. 39, no. 1, pp. 347–352, 2013.

[74] A. Vincent, J. L. Luo, K. T. Chuang, and A. R. Sanger, “Effect of Ba doping on performance of LST as anode in solid oxide fuel cells,” *J. Power Sources*, vol. 195, pp. 769–774, 2010.

[75] X. Hou, O. Marin-Flores, B. W. Kwon, J. Kim, M. G. Norton, and S. Ha, "Gasoline-fueled solid oxide fuel cell with high power density," *J. Power Sources*, vol. 268, no. December, pp. 546–549, 2014.

[76] B. W. Kwon *et al.*, "High-Performance Molybdenum Dioxide-Based Anode for Dodecane-Fueled Solid-Oxide Fuel Cells (SOFCs)," *Energy Technol.*, vol. 2, no. 5, pp. 425–430, 2014.

[77] S. J. Litzelman, A. Rothschild, and H. L. Tuller, "The electrical properties and stability of $SrTi_{0.65}Fe_{0.35}O_{3-\delta}$ thin films for automotive oxygen sensor applications," vol. 108, pp. 231–237, 2005.

[78] A. Rothschild, S. J. Litzelman, H. L. Tuller, W. Menesklou, T. Schneider, and E. Ivers-tiff, "Temperature-independent resistive oxygen sensors based on $SrTi_{1-x}Fe_xO_{3-\delta}$ solid solutions," vol. 108, pp. 223–230, 2005.

[79] D. P. Fagg, V. V Kharton, J. R. Frade, and a a L. Ferreira, "Stability and mixed ionic – electronic conductivity of (Sr,La)(Ti ,Fe)O_3 À d perovskites," *Solid State Ionics*, vol. 156. pp. 45–57, 2003.

[80] a. a. Murashkina, E. Y. Pikalova, and a. K. Demin, "Promising membrane materials based on strontium titanate," *Russ. J. Electrochem.*, vol. 45, no. 5, pp. 542–547, 2009.

[81] A. Rothschild, W. Menesklou, H. L. Tuller, and E. Ivers-tiffe, "Electronic Structure , Defect Chemistry , and Transport Properties of $SrTi_{1-x}Fe_xO_{3-y}$ Solid Solutions," no. 1, pp. 3651–3659, 2006.

[82] "Fe-substituted $SrTiO_{3-\delta}$–$Ce_{0.9}Gd_{0.1}O_2$ composite anodes for solid oxide fuel cells.pdf." .

[83] G. Valderrama, a. Kiennemann, and M. R. Goldwasser, "Dry reforming of CH4 over solid solutions of $LaNi_{1-x}Co_xO_3$," *Catalysis Today*, vol. 133–135. pp. 142–148, 2008.

[84] N. G. A. S. Conversion, S. Science, and E. S. B. V All, "Dry reforming of methane. Interest of La-Ni-Fe solid solutions compared to $LaNiO_3$ and $LaFeO_3$," vol. 119, pp. 741–746, 1998.

[85] M. Assaf, "Ni – Fe catalysts based on perovskite-type oxides for dry reforming of methane to syngas," vol. 108, no. April, pp. 63–70, 2006.

[86] and D. H. A. Button, D. D., "Development of $La_{1-x}Sr_xCoO_3$ air electrodes for solid electrolyte fuel cells," in *Amer Ceram Soc Washington*.

[87] H.-H. Mobius, “On the history of solid electrolyte fuel cells,” *J. Solid State Electrochem.*, vol. 1, no. 1, pp. 2–16, 1997.

[88] V. V Kharton, A. P. Viskup, E. N. Naumovich, and F. M. B. Marques, “Oxygen ion transport in La2NiO4 -based ceramics,” *J. Mater. Chem.*, vol. 9, pp. 2623–2629, 1999.

[89] V. V. Kharton, A. P. Viskup, A. V. Kovalevsky, E. N. Naumovich, and F. M. B. Marques, “Ionic transport in oxygen-hyperstoichiometric phases with K_2NiF_4-type structure,” *Solid State Ionics*, vol. 143, no. 3–4, pp. 337–353, 2001.

[90] E. Environ, A. Chroneos, B. Yildiz, A. Taranc, and J. A. Kilner, “Environmental Science Oxygen diffusion in solid oxide fuel cell cathode and electrolyte materials : mechanistic insights from atomistic simulations,” pp. 2774–2789, 2011.

[91] C. Tealdi *et al.*, “High-temperature neutron diffraction study of $La_{2-x}Sr_xCoO_4$: Correlation between structure and transport properties,” pp. 1–8, 2010.

[92] T. Matswra, J. Tabuchi, and K. Fueki, “Electrical properties of $La_{2-x}Sr_xCoO_4$—II: Models and analysis of the relationship between cobalt 3d electron state and structural, electrical and magnetic properties,” vol. 49, pp. 1409–1418, 1988.

[93] X. Yang, L. Luo, and H. Zhong, “Structure of $La_{2-x}Sr_xCoO_{4\pm\lambda}$(x=0.0–1.0) and their catalytic properties in the oxidation of CO and C_3H_8,” vol. 272, pp. 299–303, 2004.

[94] M. Al Daroukh, V. V. Vashook, H. Ullmann, F. Tietz, and I. Arual Raj, “Oxides of the AMO_3 and A_2MO_4-type: structural stability, electrical conductivity and thermal expansion,” *Solid State Ionics*, vol. 158, no. 1–2, pp. 141–150, 2003.

[95] X. Yang, “Preparation of $LaSrCoO_4$ mixed oxides and their catalytic properties in the oxidation of CO and C_3H_8,” vol. 6, pp. 13–17, 2005.

[96] E. V Tsipis and V. V Kharton, “Electrode materials and reaction mechanisms in solid oxide fuel cells : a brief review,” pp. 1367–1391, 2008.

[97] N. Kinadjan, R. Sayers, H. El Shinawi, C. Greaves, and S. J. Skinner, “Performance of $La_{2-x}Sr_xCo_{0.5}Ni_{0.5}O_4$±d as an Oxygen Electrode for Solid Oxide Reversible Cells,” no. 1, pp. 102–107, 2011.

[98] T. Nakamura, K. Yashiro, K. Sato, and J. Mizusaki, “Oxygen nonstoichiometry and defect equilibrium in $La_{2-x}Sr_xNiO_4+\delta$,” *Solid State Ionics*, vol. 180, no. 4–5, pp. 368–376, 2009.

[99] S. J. Skinner and J. A. Kilner, “Oxygen diffusion and surface exchange in $La_{2-x}Sr_xNiO_{4+\delta}$Oxygen diffusion and surface exchange in $La_{2-x}Sr_xNiO_{4+\delta}$,” *Solid State Ionics*, vol. 135, no. 1–4, pp. 709–712, 2000.

[100] M. Rieu, R. Sayers, M. A. Laguna-bercero, S. J. Skinner, P. Lenormand, and F. Ansart, “Investigation of graded $La_2NiO_{4+\delta}$ cathodes to improve SOFC electrochemical performance,” pp. 477–480, 2010.

[101] A. B. Yunnanica, “Electrical characterization of Co-doped $La_2CuO_{4+\delta}$ at elevated temperature,” vol. 34, no. 2, pp. 8–10, 2008.

[102] D. M. Bochkov, V. V Kharton, A. V Kovalevsky, A. P. Viskup, and E. N. Naumovich, “Oxygen permeability of $La_2Cu(Co)O$ù solid solutions,” vol. 120, no. January, pp. 281–288, 1999.

[103] A. Galenda, M. M. Natile, V. Krishnan, H. Bertagnolli, and A. Glisenti, “LaSrCoFeO and Fe_2O_3/LaSrCoFeO powders: synthesis and characterization,” *Chem. Mater.*, vol. 19, no. 11. pp. 2796–2808, 2007.

[104] L. C. Yang, Q. S. Gao, Y. Tang, Y. P. Wu, and R. Holze, “MoO_2 synthesized by reduction of MoO_3 with ethanol vapor as an anode material with good rate capability for the lithium ion battery,” *J. Power Sources*, vol. 179, no. 1, pp. 357–360, 2008.

[105] S. Vasala, H. Yamauchi, and M. Karppinen, “Role of $SrMoO_4$ in Sr_2MgMoO_6 synthesis,” *J. Solid State Chem.*, vol. 184, no. 5, pp. 1312–1317, 2011.

[106] L. Dos Santos-Gómez, L. León-Reina, J. M. Porras-Vázquez, E. R. Losilla, and D. Marrero-López, “Chemical stability and compatibility of double perovskite anode materials for SOFCs,” *Solid State Ionics*, vol. 239, pp. 1–7, 2013.

[107] D. Marrero-López *et al.*, “Redox behaviour, chemical compatibility and electrochemical performance of $Sr_2MgMoO_{6-\delta}$ as SOFC anode,” *Solid State Ionics*, vol. 180. pp. 1672–1682, 2010.

[108] K. Takehira, T. Shishido, and M. Kondo, “Partial Oxidation of CH_4 over Ni / $SrTiO_3$ Catalysts Prepared by a Solid-Phase Crystallization Method,” vol. 316, pp. 307–316, 2002.

[109] W. K. Jozwiak, E. Kaczmarek, T. P. Maniecki, W. Ignaczak, and W. Maniukiewicz, “Reduction behavior of iron oxides in hydrogen and carbon monoxide atmospheres,” *Appl. Catal. A Gen.*, vol. 326, no. 1, pp. 17–27, 2007.

[110] P. Ciambelli *et al.*, “La, Ca and Fe oxide perovskites: Preparation, characterization and catalytic properties for methane combustion,” *Appl. Catal. B Environ.*, vol. 33, no. 3, pp. 193–203, 2001.

[111] J. Kubo and W. Ueda, “Catalytic behavior of $AMoO_x$ (A = Ba, Sr) in oxidation of 2-propanol,” *Mater. Res. Bull.*, vol. 44, no. 4, pp. 906–912, 2009.

[112] “Optimized energy conversion efficiency in solid-oxide fuel cells implementing $SrMo_{1-x}Fe_xO_{3-\delta}$ perovskites as anodes.” .

[113] R. Martínez-Coronado, J. a. Alonso, a. Aguadero, and M. T. Fernández-Díaz, “New $SrMo_{1-x}Cr_xO_{3-\delta}$ perovskites as anodes in solid-oxide fuel cells,” *International Journal of Hydrogen Energy*, vol. 39. pp. 4067–4073, 2014.

[114] B. Ura *et al.*, “Effect of potassium addition on catalytic activity of $SrTiO_3$ catalyst for diesel soot combustion,” *Appl. Catal. B Environ.*, vol. 101, no. 3–4, pp. 169–175, 2011.

[115] W. Yang, “X-ray photoelectron spectroscopy and electrical properties studies of La_2O_3-doped strontium titanate ceramics prepared by sol-precipitation method,” vol. 4, pp. 3533–3544, 1999.

[116] P. V Nagarkar, P. C. Searson, F. D. G. Iii, P. V Nagarkar, P. C. Searson, and F. D. Gealy, “Effect of surface treatment spectroscopic study on $SrTiO_3$: An x-ray photoelectron,” vol. 459, no. 1991, 2013.

[117] S. Tsunekawa, S. Ito, T. Mori, K. Ishikawa, Z. Li, and Y. Kawazoe, “Critical size and anomalous lattice expansion in nanocrystalline $BaTiO_3$ particles,” vol. 62, no. 5, 2000.

[118] M. Wegmann, “XPS Analysis of Submicrometer Barium Titanate Powder,” vol. 77, pp. 371–377, 2004.

[119] S. Kumar, V. S. Raju, and T. R. N. Kutty, “Investigations on the chemical states of sintered barium titanate by X-ray photoelectron spectroscopy,” vol. 206, pp. 250–261, 2003.

[120] C. a. Ellefson, O. Marin-Flores, S. Ha, and M. G. Norton, “Synthesis and applications of molybdenum (IV) oxide,” *J. Mater. Sci.*, vol. 47, no. 5, pp.

2057–2071, 2012.

[121] J. Li *et al.*, “Molybdenum substitution at the B-site of lanthanum strontium titanate anodes for solid oxide fuel cells,” *Int. J. Hydrogen Energy*, pp. 1–8, 2017.

[122] J. Choi and L. T. Thompson, “XPS study of as-prepared and reduced molybdenum oxides,” vol. 93, pp. 143–149, 1996.

[123] P. Company and T. Netherlunds, “An XPS investigation of the interaction of CH_4, C_2H_2, C_2H_4 and C_2H_6 with a barium surface,” vol. 123, pp. 369–383, 1982.

[124] T. Hanawa, “Calcium phosphate naturally formed on titanium in electrolyte solution,” vol. 12, 1991.

[125] J. Zou and G. L. Schrader, “Multicomponent Thin Film Molybdate Catalysts for the Selective Oxidation of 1 , 3-Butadiene,” vol. 686, no. 229, pp. 667–686, 1996.

[126] R. D. Shannon, “Revised effective ionic radii and systematic studies of interatomic distances in halides and chalcogenides,” *Acta Crystallogr. Sect. A*, vol. 32, pp. 751–767, 1976.

[127] M. a Pena and J. L. G. Fierro, “Chemical structures and performances of perovskite oxides,” *Chem. Rev.*, vol. 101, pp. 1981–2017, 2001.

[128] P. Mars and D. W. van Krevelen, “Oxidations carried out by means of vanadium oxide catalysts,” *Chem. Eng. Sci.*, vol. 3, pp. 41–59, 1954.

[129] J.-H. Li, X.-Z. Fu, J.-L. Luo, K. T. Chuang, and A. R. Sanger, “Application of $BaTiO_3$ as anode materials for H2S-containing CH_4 fueled solid oxide fuel cells,” *J. Power Sources*, vol. 213, pp. 69–77, 2012.

[130] D. Pakhare and J. Spivey, “A review of dry (CO_2) reforming of methane over noble metal catalysts,” *Chem. Soc. Rev.*, vol. 43, p. , 2014.

[131] U. Olsbye, T. Wurzel, and L. Mleczko, “Kinetic and Reaction Engineering Studies of Dry Reforming of Methane over a Ni / La / Al_2O_3 Catalyst,” vol. 5885, no. 97, pp. 5180–5188, 1997.

[132] M. Usman, W. M. a. Wan Daud, and H. F. Abbas, “Dry reforming of methane: Influence of process parameters—A review,” *Renew. Sustain. Energy Rev.*, vol. 45, pp. 710–744, 2015.

[133] M.-S. Fan, A. Z. Abdullah, and S. Bhatia, “Catalytic Technology for Carbon Dioxide Reforming of Methane to Synthesis Gas,” *ChemCatChem*, vol. 1, no. 2, pp. 192–208, 2009.

[134] CNRS, “Institut de Chimie de la Matière Condensée de Bordeaux CNRS.”

[135] M. N. Pérez-Camacho, J. Abu-Dahrieh, A. Goguet, K. Sun, and D. Rooney, “Self-cleaning perovskite type catalysts for the dry reforming of methane,” *Chinese J. Catal.*, vol. 35, no. 8, pp. 1337–1346, 2014.

[136] S. A. X-ray and P. Oxidation, “Hydrogen and Synthesis Gas by Steam- and CO * Reforming,” vol. 47, 2002.

[137] W. Wang, C. Su, Y. Wu, R. Ran, and Z. Shao, “Progress in Solid Oxide Fuel Cells with Nickel-Based Anodes Operating on Methane and Related Fuels,” 2012.

[138] H. Hayashi, “Thermal expansion of Gd-doped ceria and reduced ceria,” *Solid State Ionics*, vol. 132, no. 3–4, pp. 227–233, 2000.

[139] A. L. Soldati, L. C. Baqué, H. E. Troiani, and A. C. Serquis, “World â€™ s largest Science , Technology & Medicine Open Access book publisher Electrode / Electrolyte Interphase Characterization in Solid Oxide Fuel Cells.”

[140] S. Zha, W. Rauch, and M. Liu, “Ni-$Ce_{0.9}Gd_{0.1}O_{1.95}$ anode for GDC electrolyte-based low-temperature SOFCs,” *Solid State Ionics*, vol. 166, no. 3–4, pp. 241–250, 2004.

[141] J. Dailly, S. Fourcade, A. Largeteau, F. Mauvy, J. C. Grenier, and M. Marrony, “Perovskite and A_2MO_4-type oxides as new cathode materials for protonic solid oxide fuel cells,” *Electrochim. Acta*, vol. 55, no. 20, pp. 5847–5853, 2010.

[142] Z. Du, H. Zhao, C. Yang, Y. Shen, and C. Yan, “Optimization of strontium molybdate based composite anode for solid oxide fuel cells,” *J. Power Sources*, vol. 274, pp. 568–574, 2015.

[143] S. P. S. B. Jiang, S.P., “An electrode kinetics study of H2 oxidation on Ni/Y_2O_3 –ZrO_2 cermet electrode of the solid oxide fuel cell,” vol. 123, pp. 209–224, 1999.

[144] H. I. M. Mogensen, T. Lindegaard, in: S.C. Singhal, “Proceedings of the 3rd International Symposium on Solid Oxide Fuel Cells, The Electrochemical Society Proceedings Series, The Electrochemical Society, Pennington,”

1993.

[145] E. C. S. Transactions and T. E. Society, “Comparative Study of Metal Impregnated Lanthanum Doped Strontium Titanate Anodes and Conventional Nickel Oxide Anode for Solid Oxide Fuel Cell Application,” vol. 78, no. 1, pp. 1375–1383, 2017.

[146] K. Bin Yoo and G. M. Choi, “Performance of La-doped strontium titanate (LST) anode on LaGaO3-based SOFC,” *Solid State Ionics*, vol. 180, no. 11–13, pp. 867–871, 2009.

[147] Q. Li, X. Zeng, L. Sun, H. Zhao, L. Huo, and J. Grenier, “Electrochemical performance of La $_2$ Cu $_{1-x}$ Co $_x$ O 4 cathode materials for intermediate-temperature SOFCs,” *Int. J. Hydrogen Energy*, vol. 37, no. 3, pp. 2552–2558, 2011.

[148] H. Zhong and R. Zeng, “Structure of $LaSrMO_4$ (M = Mn, Fe, Co, Ni, Cu) and their catalytic properties in the total oxidation of hexane,” *J. Serbian Chem. Soc.*, vol. 71, no. 10, pp. 1049–1059, 2006.

[149] X. Du, G. Zou, and X. Wang, “Low-Temperature Synthesis of Ruddlesden-Popper Type Layered Perovskite $La_xCa_{3-x}Mn_2O_7$ for Methane Combustion,” *Catal. Surv. from Asia*, vol. 19, no. 1, pp. 17–24, 2015.

[150] K. Sutthiumporn, T. Maneerung, Y. Kathiraser, and S. Kawi, “CO2 dry-reforming of methane over $La_{0.8}Sr_{0.2}Ni_{0.8}M_{0.2}O_3$ perovskite (M = Bi, Co, Cr, Cu, Fe): Roles of lattice oxygen on C-H activation and carbon suppression,” *Int. J. Hydrogen Energy*, vol. 37, no. 15, pp. 11195–11207, 2012.

[151] G. Valderrama, A. Kiennemann, and M. R. Goldwasser, “La-Sr-Ni-Co-O based perovskite-type solid solutions as catalyst precursors in the CO_2 reforming of methane,” *J. Power Sources*, vol. 195, no. 7, pp. 1765–1771, 2010.

[152] P. La and D. Pechini, “Popper phase prepared by a modified Pechini method Reducibilidad y comportamiento catalítico de la por el método de Pechini modificado Redutibilidade e comportamento catalítico da fase Ruddlesden-,” vol. 30, no. 1, pp. 33–43, 2016.

[153] P. Sr, X. C. Λ. With, and K. N. Structure, “Preparation and catalytic oxidaion performance of $Pr_{2-x}Sr_xCoO_4$ with K_2NiF_4 structure,” vol. 87, no. 1, pp. 139–148, 2006.

[154] S. La, C. H. Co, B. S. Liu, and C. T. Au, “Sol–gel-generated La $_2$ NiO $_4$ for CH 4 /CO 2 reforming,” vol. 85, no. 3, pp. 165–170, 2003.

[155] L. Hui, C. Ping, G. Yuping, and L. Yueqing, “Preparation , Crystal Structure , and Reducibility of K_2NiF_4 Type Oxides,” vol. 104, no. 141, pp. 99–104, 1998.

[156] H. Zhong and R. Zeng, “Structure of $LaSrMO_4$ (M = Mn , Fe , Co , Ni , Cu) and their catalytic properties in the total oxidation of hexane,” vol. 71, no. 10, pp. 1049–1059, 2006.

[157] P. C. A. Glisenti, M. Pacella, M. Guiotto, M.M. Natile, “Largely Cu-doped $LaCo_{1-x}Cu_xO_3$ perovskites for TWC Toward new PGM-free catalysts,” *Appl Catal B-Environ*, vol. 180, pp. 94–105, 2016.

[158] R. Zhang, A. Villanueva, H. Alamdari, and S. Kaliaguine, “Catalytic reduction of NO by propene over $LaCo_{1-x}Cu_xO_3$ perovskites synthesized by reactive grinding,” *Appl. Catal. B Environ.*, vol. 64, pp. 220–233, 2006.

[159] A. Glisenti, A. Galenda, and M. M. Natile, “Steam reforming and oxidative steam reforming of methanol and ethanol: The behaviour of $LaCo_{0.7}Cu_{0.3}O_3$,” *Appl. Catal. A Gen.*, vol. 453, pp. 102–112, 2013.

[160] A. Galenda, M. M. Natile, L. Nodari, and A. Glisenti, “$La_{0.8}Sr_{0.2}Ga_{0.8}Fe_{0.2}O_{3-\delta}$: Influence of the preparation procedure on reactivity toward methanol and ethanol,” *Applied Catalysis B: Environmental*, vol. 97, no. 3–4. pp. 307–322, 2010.

[161] T. Saitoh, “Strontium-doped Lanthanum Cobalt Oxides Studied by XPS,” *Surf. Sci. Spectra*, vol. 6, no. 4, p. 302, 1999.

[162] D. Mullica, H. Perkins, C. Lok, and V. Young, “The X-ray photoemission spectra of La(OH)3,” *… Electron Spectrosc. …*, vol. 61, pp. 337–355, 1993.

[163] L. G. Tejuca and J. Fierro, “XPS and TPD probe techniques for the study of LaNiO3 perovskite oxide,” *Thermochim. Acta*, vol. 147, no. 2, pp. 361–375, 1989.

[164] M. F. Sunding, K. Hadidi, S. Diplas, O. M. L iik, T. E. Norby, and A. E. Gunn??s, “XPS characterisation of in situ treated lanthanum oxide and hydroxide using tailored charge referencing and peak fitting procedures,” *J. Electron Spectros. Relat. Phenomena*, vol. 184, no. 7, pp. 399–400, 2011.

[165] P. Ivanova, A. W. Naumkin, and L. A. Vasilyev, “An XPS study of compositional changes induced by argon ion bombardment of the LaPO , surface,” vol. 47, no. l, pp. 67–71, 1995.

[166] "NIST XPS Database 20, Version 3.4 (Web Version)." .

[167] A. Galenda, M. M. Natile, and A. Glisenti, "$La_{0.6}Sr_{0.4}Co_{0.8}Fe_{0.2}O_{3-\delta}$ and $Fe_2O_3/La_{0.6}Sr_{0.4}Co_{0.8}Fe_{0.2}O_{3-\delta}$ Powders: XPS Characterization," *Surf. Sci. Spectra*, vol. 13, no. 1, pp. 31–47, 2006.

[168] T. A. A. Kobeleva S.P., Lapshina I.E., Orlov A.F., Titov A.A., "Kobeleva S.P., Lapshina I.E., Orlov A.F., Titov A.A., Titov A.A.," *Poverkhnost*, vol. 111, 1994.

[169] À. Sr, C. Ni, H. El Shinawi, and C. Greaves, "Synthesis and characterization of $La1_{.5+x}Sr0_{.5-x}Co_{0.5}Ni_{0.5}O_{4\pm\delta}$ (x = 0, 0.2)," pp. 504–511, 2010.

[170] N. R. Raoj and M. W. Roberts, "Nature of the Oxygen Species at Ni(110) and Ni(100) Surfaces Revealed by Exposure to Oxygen and Oxygen-Ammonia Mixtures: Evidence for the Surface Reactivity of O- Type Species," no. 100, pp. 3310–3316, 1995.

[171] G. Ertl, R. Hierl, H. Knozinger, N. Thiele, and H. P. Urbach, "XPS Study of copper aluminate catalysts," vol. 5, pp. 49–64, 1980.

[172] M. Polak, "Structural, Chemical, and Electronic State on $La_{0.7}Sr_{0.3}MnO_3$ Dense Thin-Film Surfaces at High Temperature: Surface Segregation," *J. Phys. Condens. Matter*, vol. 28, no. 6, pp. 235–240, 2016.

[173] W. Lee, J. W. Han, Y. Chen, Z. Cai, and B. Yildiz, "Cation Size Mismatch and Charge Interactions Drive Dopant Segregation at the Surfaces of Manganite Perovskites," p. 2139, 2011.

[174] L. Zhu, G. Lu, Y. Wang, Y. Guo, and Y. Guo, "Effects of Preparation Methods on the Catalytic Performance of $LaMn_{0.8}Mg_{0.2}O_3$ Perovskite for Methane Combustion," *Chinese J. Catal.*, vol. 31, no. 8, pp. 1006–1012, 2010.

[175] G. Saracco, "Methane combustion on Mg-doped $LaCrO_3$ perovskite catalysts," *Appl. Catal. B Environ.*, vol. 8, no. September 1998, pp. 229–244, 1996.

[176] T. S. H. Arai, T. Yamada, K. Eguchi, "Catalytic combustion of methane over various perovskite-type oxides," vol. 26, pp. 265–276, 1986.

[177] B. Christian Enger, R. Lødeng, and A. Holmen, "A review of catalytic partial oxidation of methane to synthesis gas with emphasis on reaction mechanisms over transition metal catalysts," *Appl. Catal. A Gen.*, vol. 346, pp. 1–27, 2008.

[178] Y. Liu, J. Chen, F. Liang, J. Pu, B. Chi, and L. Jian, “Thermochemical compatibility and polarization behaviors of fuel cell,” *Int. J. Hydrogen Energy*, vol. 38, no. 16, pp. 6802–6808, 2013.

[179] V. V Kharton, “Ceria-based materials for solid oxide fuel cells,” vol. 6, pp. 1105–1117, 2001.

[180] A. L. Soldati, L. C. Baqué, H. E. Troiani, and A. C. Serquis, “Electrode/Electrolyte Interphase Characterization in Solid Oxide Fuel Cells.”

[181] J. Zhou, G. Chen, K. Wu, and Y. Cheng, “$La_{0.8}Sr_{1.2}CoO\grave{u}$–CGO composite as cathode on $La_{0.9}Sr_{0.1}Ga_{0.8}Mg_{0.2}O3-\delta$ electrolyte for intermediate temperature solid oxide fuel cells,” *J. Power Sources*, vol. 232, pp. 332–337, 2013.

[182] F. Zhao, X. Wang, Z. Wang, R. Peng, and C. Xia, “K_2NiF_4 type $La_{2-x}Sr_xCo_{0.8}Ni_{0.2}O_{4+\delta}$ as the cathodes for solid oxide fuel cells,” vol. 179, pp. 1450–1453, 2008.

[183] A. Ovalle, J. C. Ruiz-Morales, J. Canales-Vázquez, D. Marrero-López, and J. T. S. Irvine, “Mn-substituted titanates as efficient anodes for direct methane SOFCs,” *Solid State Ionics*, vol. 177, no. 19–25 SPEC. ISS., pp. 1997–2003, 2006.

[184] “Electrochemical oxidation of sour natural gas over $La_{0.4}Ce_{0.6}O_{1.8}$–$La_{0.4}Sr_{0.6}TiO_{3\pm\delta}$ anode in SOFC A mechanism study of H_2S effects.” .

[185] A. Sin *et al.*, “Stabilisation of composite LSFCO – CGO based anodes for methane oxidation in solid oxide fuel cells,” vol. 145, pp. 68–73, 2005.

[186] ESRF, “http://www.esrf.eu.” .

[187] C. H. Wendel, P. Kazempoor, and R. J. Braun, “Novel electrical energy storage system based on reversible solid oxide cells: System design and operating conditions,” *J. Power Sources*, vol. 276, pp. 133–144, 2015.

Abstract

Title: "Perovskite materials as electrodes for solid oxide fuel cells active toward sustainable reactions"

Traditional solid oxide fuel cell (SOFC) work between 800 °C and 1000 °C but this induces great materials deterioration and a high device cost. The development of new electrodes for SOFC application, characterized by high activity at intermediate temperatures (600-800 °C), is extremely important for the commercial diffusion and the future of this technology. In this research advanced perovskite materials were studied as electrodes for Solid Oxide fuel cell application. Particular attention was paid to their activity toward sustainable reaction (methane oxidation and dry reforming) and the design of material avoiding platinum group elements and minimizing rare earth elements. The methane was chosen due to its role as bio-fuel in the carbon footprint decrease (bio gas, CH_4 and CO_2). Two different perovskite-based materials have been studied for SOFC application, titanates and cobaltites. All samples were prepared by means citric method and deeply characterized by XRD, XPS, TPR, TPO, BET, SEM and EIS. The catalytic activities toward methane (reforming and oxidation) were detected by GC. Among titanates ($SrTiO_3$ doped with Mo or Fe) only $SrTi_{0.9}Mo_{0.1}O_3$ infiltrated with 15%wt shown a good activity toward dry reforming (58% of CH_4 conversion at 800 °C) with an interesting polarisation resistance observed, 1.57 Ω cm² at 800°C under 5% of H_2/Ar. $(LaSr)Co_{0.5}M_{0.5}O_4$ (M = Cu, Ni) Ruddlesden Popper type cobaltites were investigated as electrodes for symmetric solid oxide fuel cell. The best catalytic activity was observed on $(LaSr)_2Co_{0.5}Ni_{0.5}O_4$ achieving 80% of CH_4 conversion at 800 °C in methane oxidation. The electrochemical behaviour of $(LaSr)_2Co_{0.5}Ni_{0.5}O_4$ was tested under air (cathode) and under 5% CH_4/Ar (anode) conditions showing a polarization resistance of 0.56 Ω cm² and 0.94 Ω m² at 800 °C respectively. In order to go deeper inside the performance of these materials, both in term of MIEC and of catalytic activity, in situ time resolved high energy X-ray diffraction analysis was carried out to deeply investigate the structural changes of Co-based perovskite under pulsing conditions. The experiments were executed at European synchrotron radiation facility (ESRF) in Grenoble. The high reversibility observed on Co-based perovskites have revealed the potential of these materials encouraging further studies on more complex systems for symmetric and

reversible SOFC application. The data collected give useful information on structural change involved into catalytic activity.

Titolo:" Materiali perovskitici come elettrodi per celle a combustibile ad ossido solido attive in reazioni sostenibili"

La tradizionale cella a combustibile ad ossido solido (SOFC) lavora tra gli 800 °C e i 1000 °C, tuttavia questa condizione induce un notevole deterioramento ed un conseguente aumento dei costi dei materiali. Lo sviluppo di nuovi materiali elettrodici per applicazioni SOFC, caratterizzati da un'alta attività a temperature intermedie (600-800 °C), è estremamente importante per la commercializzazione e il futuro di questa tecnologia. In questa ricerca, materiali perovskitici avanzati sono stati studiali come elettrodi per celle a combustibili ad ossido solido. Particolare attenzione è stata posta alla loro attività verso reazioni sostenibili (l'ossidazione e il reforming del metano) e alla formulazione di materiali privi di elementi del gruppo del platino e minimizzando la quantità di terre rare. Il metano è stato scelto grazie il suo ruolo come bio-combustibile nella diminuzione dell'impronta del carbonio (bio-gas, CH_4 e CO_2). Due tipi differenti di materiali perovskitici sono stati studiati per applicazioni SOFC, i titanati e i cobaltiti. Tutti i materiali sono stati preparati tramite il metodo dei citrati e caratterizzati con XRD, XPS, TPR, TPO, BET, SEM e EIS. Le attività catalitiche verso il metano (reforming e ossidazione) sono state misurate attraverso il GC. Tra i titanati studiati ($SrTiO_3$ sostituito con Mo o Fe) solo $SrTi_{0.9}Mo_{0.1}O_3$ infiltrato con il 15% wt ha mostrato una buona attività verso il reforming del metano (58% della conversione di CH_4 a 800 °C) con un interessante resistenza di polarizzazione pari a 1.57 Ω cm² a 800°C sotto flusso di 5% H_2/Ar. I cobaltiti con struttura tipo Ruddlesden Popper, $(LaSr)Co_{0.5}M_{0.5}O_4$ (M = Cu, Ni), sono stati invece studiati come elettrodi per SOFC simmetriche. La migliore attività catalitica è stata osservata su $(LaSr)Co_{0.5}Ni_{0.5}O_4$ raggiungendo una conversione del 80% di CH_4 a 800 °C nell'ossidazione del metano. Il comportamento elettrochimico di $(LaSr)Co_{0.5}M_{0.5}O_4$ è stato testato in aria (catodo) e sotto flusso di 5% di metano (anodo) mostrando una resistenza di polarizzazione di 0.56 Ω cm² e 0.94 Ω m² a 800 °C rispettivamente. Al fine di andare a fondo sulle performance di questi materiali, sia in termini di MIEC che di attività catalitica, analisi di raggi X ad alta energia in situ e risolte nel tempo sono state condotte per analizzare i cambiamenti strutturali delle perovskiti a base di cobalto sotto condizioni impulsate. Gli esperimento sono stati condotti al European synchrotron radiation facility (ESRF) a Grenoble. L'alta reversibilità osservata nei cobaltiti ha rivelato il potenziale di questi materiali incoraggiando ulteriori studi su sistemi più complessi per celle SOFC simmetriche e reversibili. I dati raccolti hanno prodotto informazioni preziose sui cambi strutturali che avvengono durante l'attività catalitica.

Ringraziamenti

Con questa tesi finisce un capitolo importante della mia vita, durante il quale mi sono divertito, sono cresciuto, ho creato nuove relazioni, ho imparato, ma ho anche faticato, alternando momenti alti e bassi soprattutto negli ultimi mesi. Per fortuna non mi sono mai sentito solo, non posso quindi esimermi dal non ringraziare le persone che sono state vicine e che mi hanno supportato, dandomi la forza per arrivare fino alla fine.

Il ringraziamento più grande va alla prof.ssa Antonella Glisenti, per avermi dato l'opportunità di fare il dottorato e permesso di sviluppare in modo autonomo le mie idee, dandomi anche la possibilità di trascorrere dei periodi di ricerca all'estero e di partecipare a numerose conferenze. Senza il suo supporto e guida tutto questo lavoro non sarebbe stato possibile.

Alla dott.ssa Marta Maria Natile per il suo supporto, i suoi numerosi consigli e il tempo che mi ha dedicato.

Al dott.Davide Ferri, per le svariate collaborazioni e per avermi permesso di effettuare delle ricerche presso il sincrotrone di Grenoble.

Al prof. Fabrice Mauvy, per avermi accolto presso il "Institut de Chimie de la Matière Condensée de Bordeaux" e avermi permesso di sviluppare parte della mia ricerca all'estero.

All'ormai dott. Andrea Bedon, per il continuo confronto scientifico durante questi tre anni e per essere stato sempre presente nel momento del bisogno.

A Giovanni Carollo per il suo prezioso aiuto nello sviluppo di questa ricerca e per le varie avventure che abbiamo affrontato assieme.

A tutti gli altri componenti, passati e presenti, del gruppo di ricerca "Impact" per i momenti trascorsi assieme, sia di confronto, sia di svago ma anche dell'aiuto ricevuto soprattutto in quest'ultimo periodo.

Ai miei genitori, per avermi sempre permesso di seguire i miei sogni e per avermi sostenuto qualsiasi fossero le mie scelte.

A Deborah, per aver creduto in me e avermi sopportato soprattutto in questi ultimi mesi.

Agli amici, per la pazienza che hanno avuto ogni volta che rimandavo un impegno per la ricerca.